

SYNTHESIS AND REACTIONS OF STERICALLY ENCUMBERED INORGANIC AND
ORGANOMETALLIC COMPLEXES

By

Nicholas Charles Boyde

Dissertation

Submitted to the Faculty of the
Graduate School of Vanderbilt University
in partial fulfillment of the requirements
for the degree of

DOCTOR OF PHILOSOPHY

in

Chemistry

June 30th, 2017

Nashville, Tennessee

Approved:

Timothy P. Hanusa, Ph. D.

Charles M. Lukehart, Ph. D.

David W. Wright, Ph. D.

James E. Wittig, Ph. D.

This work is dedicated to all of the educators who made my journey exciting and enlightening.

Thank you.

ACKNOWLEDGEMENTS

There are many individuals that guided me along my scientific career and I would like to briefly acknowledge them. Stephen “Wito” Witowich was instrumental in my education as he inspired my love of chemistry, challenged me to do my best, and was a friend. Although Wito is no longer alive, I constantly remember his teaching style and the energy with which he taught. I hope to inspire the next generation of chemists the way that he inspired me. Scott Mason guided me through my undergraduate career by providing me the foundations of inorganic chemistry, allowing me to design my senior research project, and offering continued guidance in my pursuit of a career in higher education.

The success of my graduate career was all thanks to the guidance and tutelage of Timothy Hanusa. My time in Tim’s lab was invaluable as the skills and experience that I gained will remain with me throughout the rest of my life. Tim’s wealth of knowledge was greatly appreciated as I learned a great deal every day and I cannot fully express my gratitude for everything that you have done.

I would like to extend a special thanks to Grant Steelman for all of the work that he has contributed to my research. It was a pleasure to work with you throughout your time in lab. Your willingness to work on a variety of projects and learn a variety of techniques made mentoring rewarding. I wish you the best in your future endeavors.

A special thanks is also owed to Nathan Schley for assisting with many crystal structures. Without the assistance of Nathan I would not have discovered a key compound for my system

and therefore might have missed a crucial discovery. His willingness to check crystals that were less than ideal was greatly appreciated.

This work was financially supported through the National Science Foundation (CHE-1112181), The American Chemical Society–Petroleum Research Fund (56027-ND3), a Discovery Grant of Vanderbilt University, and the Mitchum E. Warren, Jr. Graduate Research Fellowship.

TABLE OF CONTENTS

	Page
DEDICATION	ii
ACKNOWLEDGEMENTS	iii
LIST OF TABLES	vii
LIST OF FIGURES	viii
COMMON ABBREVIATIONS AND SYMBOLS	x
 Chapter	
1. Formation of sterically encumbered molecules to study steric and electronic effects	1
1.1 Introduction	1
1.2 Reaction conditions toward product formation	2
1.3 Bulky ligands.....	4
1.3.1 Amides.....	5
1.3.2 Allyls	5
1.4 Steric and electronic effects	6
1.5 Methods Employed.....	7
1.6 Conclusion.....	8
 2. Structural Distortions in $M[E(SiMe_3)_2]_3$ Complexes (M = Group 15, f element, E = N, CH)	9
2.1 Introduction	9
2.2 Results and Discussion.....	11
2.3 Conclusion.....	35
2.4 Experimental	36
 3. Preparation of substituted $P[N(SiMe_3)_2]_3$ complexes and nanoparticle applications	42
3.1 Introduction	42
3.2 Results and Discussion.....	44
3.2.1 Nanoparticle formation.....	44

3.2.2 Derivatives of P[N(SiMe ₃) ₂] ₃	47
3.3 Conclusion.....	50
3.4 Future Directions	51
3.5 Experimental	52
4. Reaction environment and ligand liability in group 4 Cp ₂ MX ₂ (X, Y = Cl, OtBu).....	56
4.1 Introduction	56
4.2 Results and Discussion.....	57
4.3 Conclusion.....	67
4.3 Experimental	68
5. Multicomponent mechanochemical synthesis of cyclopentadienyl titanium alkoxy halides	74
5.1 Introduction	74
5.2 Results and Discussion.....	76
5.3 Conclusion.....	91
5.4 Experimental	91
6. Symmetric assembly of a sterically encumbered allyl complex: mechanochemical and solution synthesis of the tris(allyl)beryllate, K[BeA'](A' = 1,3-(SiMe ₃) ₂ C ₃ H ₃).....	96
6.1 Introduction	96
6.2 Results and Discussion.....	98
6.3 Conclusion.....	108
6.4 Experimental	109
Appendix	
A1. Crystallographic and spectral data of Group 15 M[N(SiMe ₃) ₂] ₃	113
A2. Nanoparticle formation from P[N(SiMe ₃) ₂] ₃ and NMR spectra of attempted derivatives ...	122
A3. Crystallographic and fractional coordinates of mixed ligand group 4 species.....	128
A4. Crystallographic data of K[Be(1,3-(SiMe ₃) ₂ C ₃ H ₃) ₃].....	147
REFERENCES	148

LIST OF TABLES

Table 1 Selected bond distances, angles, and G_{solid} values in representative $M[N(\text{SiMe}_3)_2]_3$ complexes..	17
Table 2 Selected bond distances, angles, and G_{solid} values in representative $M[\text{CH}(\text{SiMe}_3)_2]_3$ complexes..	23
Table 3 Selected Experimental and UFF Optimized Bond Distances and Angles for $\text{Pu}[N(\text{SiMe}_3)_2]_3$, $\text{Ce}[\text{CH}(\text{SiMe}_3)_2]_3$, and $\text{Sb}[N(\text{SiMe}_3)_2]_3$	27
Table 4. Selected experimental and DFT optimized bond distances and angles for $E[N(\text{SiMe}_3)_2]_3$ ($E = \text{P-Bi}$)..	30
Table 5 Percent Mulliken contribution of various atomic orbitals	32
Table 6. Nanoparticle size distribution from noble metal sources.....	45
Table 7. Ratio of major peaks in ^{31}P NMR for the reaction $3K[N(\text{SiMe}_3)_2]_3 + \text{OPCl}_3$	49
Table 8. Summary of Cp_2MX_2 and $M'[\text{OtBu}]$ reactions.....	59
Table 9. Calculated and crystallographic bond distance and angles of select titanium species	91
Table 10. Summary of $K[A']$ and BeCl_2 reactions	99
Table 11 ^1H NMR shifts (ppm) and bond distances in $M[M'A'_3]$ complexes.....	101
Table 12. Crystal Data and Summary of $P[N(\text{SiMe}_3)_2]_3$	114
Table 13 Fractional Coordinates of $P[N(\text{SiMe}_3)_2]_3$	115
Table 14 Crystal Data and Summary of $\text{Sb}[N(\text{SiMe}_3)_2]_3$	119
Table 15 Fractional coordinates of $\text{Sb}[N(\text{SiMe}_3)_2]_3$	120
Table 16. Crystal Data and Summary of $\text{Cp}_3\text{Ti}(\text{OtBu})$	128
Table 17. Crystal Data and Summary of $\text{Cp}_2\text{Zr}(\text{OtBu})_2$	129
Table 18. Crystal Data and Summary of $\text{Cp}_2\text{HfCl}(\text{OtBu})$	130
Table 19. Crystal Data and Summary of $\text{Cp}_2\text{Hf}(\text{OtBu})_2$	131
Table 20. Fractional coordinates $\text{Cp}_3\text{Ti}(\text{OtBu})$	132
Table 21. Fractional coordinates $\text{Cp}_2\text{Zr}(\text{OtBu})_2$	134
Table 22. Fractional Coordinates $\text{Cp}_2\text{HfCl}(\text{OtBu})$	135
Table 23. Fractional Coordinates $\text{Cp}_2\text{Hf}(\text{OtBu})_2$	136
Table 24. Crystal Data and Summary of $\text{Cp}_2\text{TiCl}(\text{OMe})$	137
Table 25. Crystal Data and Summary of $\text{Cp}_2\text{TiCl}(\text{OiPr})$	138
Table 26. Crystal Data and Summary of $\text{Cp}_2\text{TiCl}(\text{OtBu})$	139
Table 27. Crystal Data and Summary of $\text{Cp}_2\text{TiBr}(\text{OtBu})$	140
Table 28. Crystal Data and Summary of $\text{CpTiBr}_2(\text{OtBu})$	141
Table 29. Fractional Coordinates $\text{Cp}_2\text{TiCl}(\text{OtBu})$	142
Table 30. Fractional Coordinates $\text{Cp}_2\text{TiBr}(\text{OtBu})$	143
Table 31. Fractional Coordinates $\text{CpTiBr}_2(\text{OtBu})$	146
Table 32. Fractional Coordinates $\text{Cp}_2\text{TiCl}(\text{OiPr})$	148
Table 33. Crystal Data and Summary for $K[\text{Be}(1,3-(\text{SiMe}_3)_2\text{C}_3\text{H}_3)_3]$	149

LIST OF FIGURES

Figure 1. Distinction between attractive agostic ($M \cdots H-C$) and $M \cdots Si-C$ interactions.	10
Figure 2. Thermal ellipsoid plot of non-hydrogen atoms of $P[N(SiMe_3)_2]_3$	13
Figure 3. Thermal Ellipsoid Plot of $As[N(SiMe_3)_2]_3$	14
Figure 4. Thermal Ellipsoid Plot of $Sb[N(SiMe_3)_2]_3$	15
Figure 5. Solid-G visualization of $P[N(SiMe_3)_2]_3$ and $Tb[N(SiMe_3)_2]_3$	19
Figure 6. Relationship between various bond distances and intramolecular contacts in $M[N(SiMe_3)_2]_3$ complexes.....	22
Figure 7. Relationship between (N,CH)-M-(N,CH) angles and closest intramolecular $M \cdots C(H_3)$ contacts in $M[N(SiMe_3)_2]_3$	25
Figure 8. Depiction of the LUMO of $Sb[N(SiMe_3)_2]_3$ (a) and $Lu[N(SiMe_3)_2]_3$ (b).....	34
Figure 9. AIM representations for $Lu[N(SiMe_3)_2]_3$ and $Sb[N(SiMe_3)_2]_3$	35
Figure 10. Gold nanoparticles formed from $HAuCl_4$	45
Figure 11. Platinum particles formed from $PtCl_2$	46
Figure 12. Silver particles formed from $AgOtf$	47
Figure 13. Thermal ellipsoid of $Cp_3Ti(OtBu)$	63
Figure 14. Thermal ellipsoid plot of $Cp_2Zr(OtBu)_2$	64
Figure 15. Thermal ellipsoid plot of $Cp_2HfCl(OtBu)$	65
Figure 16. Energy interrelationships between various $Cp_{2-x}Ti(OtBu)_{2+x}$ molecules.	66
Figure 17. Combinatorial possibilities of mixed group 4 $Cp_xMX_y(OR)_{4-(x+y)}$ complexes.....	75
Figure 18. Thermal ellipsoid plot of $Cp_2TiCl(OMe)$	79
Figure 19. Thermal ellipsoid plot of $Cp_2TiCl(OiPr)$	80
Figure 20. Thermal ellipsoid plot of $Cp_2TiCl(OtBu)$	82
Figure 21. Thermal ellipsoid of $Cp_2TiBr(OtBu)$	83
Figure 22. Thermal ellipsoid plot of $CpTiBr_2(OtBu)$	84
Figure 23. Molecular orbitals of $Cp_2TiCl(OtBu)$	89
Figure 24. Molecular orbitals of $CpTiBr_2(OtBu)$	90
Figure 25. Limiting bonding arrangements for $Cp_2TiCl(OtBu)$	91
Figure 26. Thermal ellipsoid plot of $KBeA'_3$	102
Figure 27. Geometry optimized structures of the $[BeA'_3]^-$ anions.....	104
Figure 28. Geometry optimized structures of the $K[BeA'_3]$ complex.....	105
Figure 29. Visualization of the extent of coordination sphere coverage ($G_{complex}$) of $BeA'_2 \cdot Et_2O$, BeA'_2 , and $KBeA'_3$	107
Figure 30. 1H NMR of $P[N(SiMe_3)_2]_3$	113
Figure 31. ^{31}P NMR of $P[N(SiMe_3)_2]_3$	113
Figure 32. EDS Mapping $HAuCl_4$ Grind.....	122
Figure 33. EDS Mapping $HAuCl_4:PN'$ THF Reaction	122
Figure 34. EDS Mapping $HAuCl_4:PN'$ Grind Reaction.....	123
Figure 35. ^{31}P NMR (proton decoupled) 3:1 $KN':SPCl_3$	124
Figure 36. ^{31}P NMR (proton decoupled) 2:1 $KN':SPCl_3$	124
Figure 37. ^{31}P NMR (proton decoupled) 1:1 $KN':SPCl_3$	125
Figure 38. ^{31}P NMR (proton decoupled) 3:1 $KN':OPCl_3$	125
Figure 39. ^{31}P NMR (proton decoupled) 3:1 $KN':OPCl_3$ (reaction 2).....	126

Figure 40. ^{31}P NMR (proton decoupled) 2:1 $\text{KN}':\text{OPCl}_3$	127
Figure 41. ^{31}P NMR (proton decoupled) 1:1 $\text{KN}':\text{OPCl}_3$	128

COMMON ABBREVIATIONS AND SYMBOLS

$\xrightarrow{\infty}$ Mechanochemical processing (grinding or milling)

A' [1,3-(SiMe₃)₂C₃H₃]⁻

KA' K[1,3-(SiMe₃)₂C₃H₃]

HA' 1,3-(SiMe₃)₂C₃H₄

A'₂ 1,3,4,6-tetrakis(trimethylsilyl)-1,5-hexadiene ([1,3-(SiMe₃)₂C₃H₃]₂)

N' [N(SiMe₃)₂]⁻

Ae alkaline-earth metal

Cp cyclopentadienyl (C₅H₅)⁻

Cp* pentamethylcyclopentadienyl (C₅Me₅)⁻

THF tetrahydrofuran

Et₂O diethyl ether

tol toluene

NMR Nuclear Magnetic Resonance

CHAPTER 1

Introduction to the use of sterically encumbered molecules to study steric and electronic effects in metal complexes

1.1 Introduction

A longstanding focus of synthetic inorganic and organometallic chemistry has been on the production and improvement of catalytically active species, and on advances in advanced materials development, with both efforts being undergirded by fundamental mechanistic studies of reactions. The interconnectedness of these goals has been evident in the recent push toward the use of relatively inexpensive, earth-abundant, non-toxic metals, coupled with attempts to move toward sustainable (green) techniques in synthesis and manufacture. This advance is reflected in many areas of the chemical enterprise, not least in the appearance of research journals dedicated to sustainable chemistry, such as *Green Chemistry* (RSC, founded 1999),¹ *ChemSusChem* (Wiley, founded 2008),² and *ACS Sustainable Chemistry & Engineering* (ACS, founded 2013).³ Sustainable synthesis techniques and efforts to modify product formation are recurring and major themes throughout the following chapters.

The three projects that will be discussed throughout the following chapters are: 1) the synthesis, characterization, and applications of group 15 MN'_3 ($N' = [N(\text{SiMe}_3)_2]$) complexes; 2) group 4 mixed ligand species of the form $\text{Cp}_x\text{MX}_y(\text{OR})_{4-(x+y)}$; and 3) the mechanochemical preparation of $\text{KB}[A']_3$ ($A' = [1,3-(\text{SiMe}_3)_2\text{C}_3\text{H}_3]$). These projects incorporate the study of: product formation as a function of reaction conditions, the use of bulky ligands in main-group chemistry, and discussions of steric and electronic effects in the resulting complexes.

1.2 The influence of reaction conditions on product formation

It goes almost without saying that synthetic inorganic and organometallic chemistry can be conducted under a variety of conditions. Factors that are often considered in the optimization of these reactions include: the choice of solvent (or whether solvent use should be avoided entirely), reaction time and temperature, and how rigorously the reaction must be protected from air and moisture. As regards the latter point, many inorganic and organometallic complexes are sensitive to oxygen and/or water, properties that in some cases can be modified through ligand choice (e.g. $\text{Ni}(\text{C}_3\text{H}_5)_2$ is highly pyrophoric⁴ but $\text{Ni}(1,3\text{-TMS-C}_3\text{H}_3)_2$ displays moderate air stability).⁵ The overall sustainability and environmental impact of synthetic routes is another factor that is increasingly being considered in the optimization process.

Organic solvents are employed in a vast number of synthetic reactions, and for a variety of undeniably good reasons: among these are promoting reagent interactions, dissipating heat in exothermic reactions, and allowing for kinetic control during product formation. Although many inorganic reactions use such solvents, there are consequences of solvent properties on the outcomes of reactions that are still poorly understood. The solvent effects in salt metathesis reactions (e.g., $\text{RM} + \text{M}'\text{X} \rightleftharpoons \text{RM}' + \text{MX}$; M = typically group 1 or 2 metal) are examined in this dissertation; this reaction type was the primary focus in the three aforementioned projects.

Traditionally conducted salt metathesis reactions suffer from a variety of problems, some of which are noted here. To begin with, solution-based reactions usually require the use of reagents with similar solubility, which can limit the range of suitable starting materials. Coordinating solvents (typically ethers such as THF or diethyl ether) may bind strongly to a metal, which may influence the overall reactivity of a final metal-ligand complex. In particular,

tightly bound ethers can prove difficult (or impossible) to remove without the decomposition of the complex. This phenomenon has been observed with various metal allyl complexes (e.g., with Mg,⁶ Be,⁷ Al,⁸ etc.). One method that has been implemented for the removal of ethereal solvents is a ‘toluene reflux’ method which has varying degrees of success.⁹⁻¹⁰ The use of nonpolar solvents for metathesis reactions is less common, but can provide an alternative route, given materials with appropriate solubility.¹¹

Metathesis reactions can generate products that do not reflect the ratio of starting materials, in which case require alternative conditions to obtain the desired product(s). As will be described later in this dissertation, the formation of metal alkoxides,¹² amides,¹³ and allyls¹⁴ can be complicated by non-stoichiometric metathesis reactions. The common method to form metal alkoxides without the use of metathesis is to treat the metal salt with the appropriate alcohol (in the presence of a base when necessary; i.e., $\text{MX}_n + n\text{HOR} \rightarrow \text{M}(\text{OR})_n + \text{HX}$). Salt metathesis of zirconium alkoxides has reportedly led to inseparable mixtures of products; thus alcoholysis was used to promote cleaner reactions.¹² Similarly the undesired tris(amido) complex $\text{M}(\text{N}(\text{SiMe}_3)_2)_3$ was prepared through metathesis, but the desired bis(amido) $\text{M}(\text{N}(\text{SiMe}_3)_2)_2$ was produced through transmetallation.¹⁵ Formations of tris(allyl) $\text{M}(\text{A}')_3$ complexes has also been reported, but there are few examples of allyl transfer reagents to circumvent the undesirable product formation.¹⁴

To address the need for alternative reaction conditions that would to avoid complications from unwanted solvation, incompatible solubilities, and non-stoichiometric reactions, attention has been given to solvent-free mechanochemical reactions. Mechanochemistry was demonstrated as early as the 4th century BCE through the grinding of cinnabar (HgS) in a copper vessel with small amounts of vinegar to produce elemental mercury and copper sulfide (eq 1).



This technique was expanded by the American chemist M. Carey Lee in the late 19th century through his investigation of metal salts that behave differently depending on whether they are subject to grinding and pressure, or simply heated. He found, for example, that silver salts such as AgCl undergo reduction upon grinding and under pressure, but only melt upon heating. This was instrumental in establishing the uniqueness of mechanochemistry as a distinct process, which until his work had been thought to be simply an extension of traditional heating methods.

Mechanochemistry utilizes solvent-free or reduced solvent reactions and can promote faster reaction times than traditional solution reactions. These benefits have been recognized by several research groups and have led to the growth of mechanochemistry in synthetic organic, inorganic, and organometallic systems. Mechanochemistry has been investigated as a possible solution to the non-stoichiometric issues related to salt metathesis reactions, and this will be discussed in later chapters.

1.3 Bulky ligands and stability

Incorporation of sterically encumbered ligands in metal complexes to promote stability has been a longstanding practice in synthetic chemistry. An example of steric bulk providing enhanced stability to a compound is found in the synthesis of free, persistent carbenes. Carbenes were long thought to be unisolatable, but the use of adamantyl substituents stabilized an N-heterocyclic carbene.¹⁶ Sterically bulk groups have also been used to promote low coordination number complexes for alkaline earth and lanthanide compounds. The formation of bulky homoleptic compounds will be discussed with reference to bis(trimethyl)silyl amides and the

bulky allyl 1,3-TMS-C₃H₃ (A'). Heteroleptic compounds involving cyclopentadienyl, halides, and alkoxides will be discussed in full detail in Chapters 4 and 5.

1.3.1 Amido Complexes of the Group 15 Elements

The bis(trimethyl)silylamido ligand (-N(SiMe₃)₂, N') binds to a wide range of metals, and the corresponding amides have been studied for applications in metal organic chemical vapor deposition (MOCVD) and atomic layer deposition (ALD).¹⁷⁻¹⁸ The promotion of low coordination numbers is another property which has been studied for this ligand. Typical coordination numbers (CN) for lanthanides are 8 or 9 for monodentate ligands, and up to 12 for chelating ligands,¹⁹ but lanthanide amides containing the bis(trimethyl)silylamido ligand can occur in the form of 3-coordinate pyramidal M(N[SiMe₃]₂)₃ complexes. The amide ligand also forms low coordination number complexes with the alkaline earths, with typical CN of 4-12,²⁰ but the amides form BeN'₂ (CN = 2) or [MN'₃]⁻/M₂N'₄ complexes (M = Mg–Ba; CN = 3).²¹⁻²²

The wide range of applications, support of low coordination numbers, and ability to form uniform binding configurations with a range of metal radii was the primary motivation for investigations with this ligand. As will be discussed in Chapters 2 and 3, the group 15 MN'₃ complexes were prepared, some for the first time. Preliminary applications studies of PN'₃ were attempted that demonstrated its ability to function as a reducing and capping agent in the formation of noble metal nanoparticles.

1.3.2 Allyl complexes

The parent allyl anion ([C₃H₅]⁻) is the smallest delocalized π-ligand, but it can also bind to metals in a σ-bonding mode (i.e., M–CH₂C(H)=CH₂). Numerous examples of metal allyl complexes have been reported, but homoleptic transition metal species (i.e., those in which allyls

are the only type of ligand) often possess poor thermal stability and are only persistent at low temperatures. The addition of trimethylsilyl groups to the parent allyl to form the bis-substituted allyl ([1,3-TMS-C₃H₃]⁻) provides sufficient bulk to shield the metal centers of complexes at room temperature, and in some cases, they also confer modest air stability on the compounds.

The formation of electron-deficient complexes that have thermal stability and potential catalytic activity is one major benefit of using a bulky allyl ligand. Although these are thermally stable at room temperature and above, their air- and moisture- stability is very low, with a majority of these complexes quickly decomposing upon exposure to traces of oxygen. Attempts to prepare an unsolvated bis(allyl) beryllium complex resulted in the isolation of an unexpected tris(allyl)beryllate, which will be discussed in further detail in Chapter 6.

1.4 Steric and electronic effects in metal complexes

The two major controllers of chemical reactions are often described under the general rubric of “steric” and “electronic” effects. In the context of inorganic reactions, steric effects reflect the consequences of interligand repulsions, and the necessity to reduce such interactions in order to achieve minimum energy structures. Electronic effects encompass everything from the oxidation states of metals to metal-ligand bond strengths. Depending on how broadly one defines the term, “electronic effects” could also be said to incorporate steric effects as well, as the latter arise from non-bonded electron repulsions between ligands. It should not be surprising, therefore, that the differentiation of these effects can often be difficult, if not impossible, and many systems are stated to display a “subtle mix of steric and electronic effects.”²³ Nevertheless, there are practical benefits to distinguishing these two influences on structure and reactivity, and studying specific complexes whose behavior can be understood as being dominated by one or the

other of these effects can provide useful insights into metal-ligand bonding interactions. Preparation of such complexes with various metal and ligand combinations was studied in the course of work on this dissertation.

Group 15 metal amides, $M[N(\text{SiMe}_3)_2]_3$, have been prepared and display close intramolecular contacts and distorted bond angles typically associated with agostic bonding interactions. This bonding motif for the group 15 compounds mimics those of lanthanide and actinide compounds, but computational investigations demonstrated that the structural similarities are largely the result of interligand steric congestion, and do not stem from any peculiar electronic parallels between the p-block and f-block elements. These results are a caveat not to be hasty in ascribing electronic origins to structural distortions that might ultimately be the result of crowding from bulky ligands.

An example of a heavily directed electronic effect can be seen in the group 4 mixed ligand species $\text{Cp}_x\text{TiX}_y(\text{OtBu})'_{4-(x+y)}$ ($X = \text{Cl}, \text{Br}$). The shortness of the Ti–O bonds and the near linearity of the Ti–O–C angles was initially believed by some to result from steric congestion, but this was shown not to be case through further investigation. Computational investigations were used to support the existence of π -bonding character in the Ti–O bonds, a result of appropriate orbital overlap. An in-depth analysis of this interaction will be found in Chapter 5.

1.5 Methods Employed in this Dissertation

Traditional air-sensitive handling techniques were employed for the syntheses outlined in later chapters. Unless specially mentioned, all reactions were run with rigorous exclusion of air and moisture. Solution-based reactions were conducted either entirely within an inert atmosphere

glove box or on a vacuum line with Schlenk techniques. Mechanochemical reactions involved sealing the reaction under nitrogen with an air-tight seal to prevent contamination.

There exists a wide range of options for implementing the grinding associated with mechanochemical reactions; these include mortar and pestles, use of vortex mixing apparatus, tube dispersers, mixer mills, and planetary ball mills. Detailed explanations about these methods have been discussed in various reviews.²⁴⁻²⁵ Reactions in this document were performed primarily on a Retsch Planetary Ball Mill (PM 100). Typical reactions were conducted for 15 minutes at a frequency of 600 revolutions per minute (RPM). Such short reaction times highlight a major advantage of mechanochemical methods of activation over commonly used solution-based approaches to synthesis.

1.6 Conclusions

In this chapter, the broad topics of bulky ligands, steric and electronic effects, and reaction conditions were briefly discussed. The junction of these general areas provides a unifying theme for the dissertation work, even though a range of ligands with metals from widely different parts of the period table were studied. Subsequent chapters will describe the synthesis of novel complexes, an examination of their structures with X-ray crystallography and computational methods, and some of their potential applications.

CHAPTER 2

Structural Distortions in $M[E(SiMe_3)_2]_3$ Complexes

(M = Group 15, f-Element; E = N, CH)

2.1 Introduction

The bis(trimethylsilyl)amido ligand, $-N(SiMe_3)_2$ (N'), is widely used in metal amide chemistry, owing to the solubility it confers on associated complexes, its substantial steric bulk, and its facile characterization with NMR spectroscopy (1H , ^{13}C , ^{29}Si).²⁶ It is also compatible with metals from across the periodic table, from Groups 1–16 (including the lanthanides and actinides). Its versatility has led to its incorporation into a variety of precursors for metal-organic chemical vapor deposition (MOCVD) and atomic layer deposition (ALD), and its alkali metal salts are extensively used in synthetic chemistry.¹⁷⁻¹⁸

Homoleptic bis(trimethylsilyl)amido group 15 complexes were of interest owing to their uses (or in some cases, potential uses) in materials chemistry. $Bi[N']_3$ is a long-known compound, and has been used to prepare amorphous BiO_x and the ferroelectric perovskite $SrBi_2Ta_2O_9$.²⁷ Its crystal structure²⁷ and some unusual associated reactions²⁸ have been described. $Sb[N']_3$ has been employed in the generation of colloidal $InSb$ nanocrystals,²⁹ in the preparation of phase-change memory materials,³⁰⁻³³ and as a precursor to antimony selenates for thermal pyrolysis studies,³⁴ although its solid state structure has not been reported. The arsenic complex $As[N']_3$ is unknown, but several related heteroleptic compounds have been prepared, including $HAs[N(SiMe_3)_2]_2$,³⁵ $ClAs[N(SiMe_3)_2]_2$,³⁶ $Cl_2AsN(SiMe_3)_2$,³⁷ $L_2AsN(SiMe_3)_2$ ($L = Cr(CO)_5$, $Fe(CO)_4$),³⁸ and $Cp^*AsCl[N(SiMe_3)_2]_2$.³⁹ The tertiary aminophosphine analogue $P[N']_3$ is also unknown, but the related hydrogen-bridged dimer $\{HP[N']_2\}_2$ has been

crystallographically characterized,³⁵ as have many L_nPN' derivatives, such as Cl_2PN' ,⁴⁰ $(Me_3SiN)_2PN(SiMe_3)_2$,⁴¹ and $\{P[N(SiMe_3)_2]_2\}_4$.⁴²

The preparation of $P[N']_3$ and $As[N']_3$, their single crystal X-ray structures, along with that of $Sb[N(SiMe_3)_2]_3$, and a comparison of the geometry of the four Group 15 $M[N']_3$ complexes are reported here. During the course of the investigation, it became apparent that many of their geometric features (e.g., distortions in $M-N-Si$ bond angles, close $M\cdots C$ and $M\cdots Si$ contacts) are paralleled in pyramidal f-element $M[N']_3$ (and related $M[CH(SiMe_3)_2]_3$) complexes. Although at one time both agostic $M\cdots(\gamma-H-C)$ and $M\cdots(\beta-Si-C)$ interactions (Figure 1) were considered as likely contributors to the f-element structures, continued investigations have demonstrated that $M\cdots(\gamma-H-C)$ interactions do not contribute to their distinctive geometric features.⁴³⁻⁴⁶

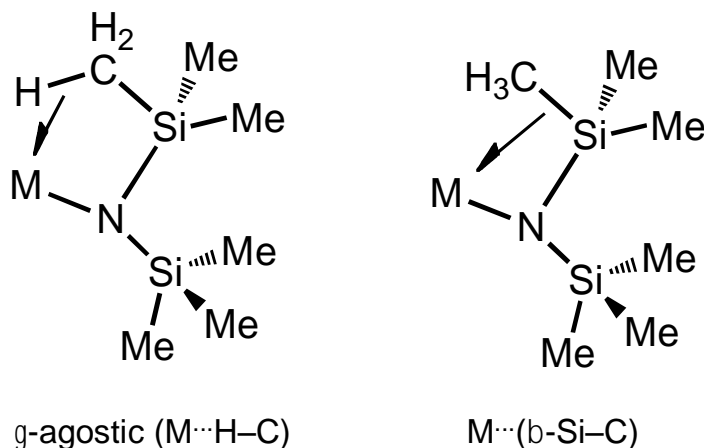


Figure 1. Distinction between attractive agostic ($M\cdots H-C$) and $M\cdots Si-C$ interactions; only the latter is thought to be operative in $M[(N,CH)(SiMe_3)_2]_3$ complexes.

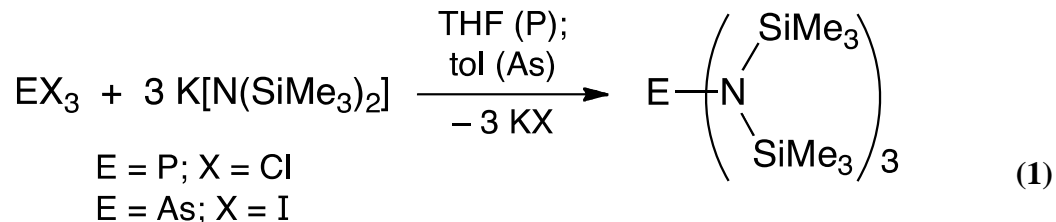
Complicating this picture is the role of steric effects in agostic and related 3-center-2-electron intramolecular interactions.⁴⁷⁻⁴⁸ For example, in metal complexes containing bulky

ligands, a C–H bond may be near a metal because such a location minimizes steric interactions with other ligands; when so positioned, it may engage in an electronic interaction with the metal center.⁴⁹⁻⁵⁰ It is conversely possible for steric interactions to place a C–H bond close to a metal center, and yet there be no agostic interaction, owing to unfavorable orbital energetics (e.g., as with the titanium amide $\text{Ti}_2\text{Cl}_6[\text{N}(t\text{-Bu})_2]_2$).⁵¹ Although interligand steric stress has been recognized as an influence on the geometries of f-element $\text{M}[\text{N}']_3$ and $\text{M}[\text{CH}(\text{SiMe}_3)_2]_3$ complexes, it is generally regarded as playing a secondary role to the $\text{M}\cdots\text{Si}-\text{C}$ interactions.

A basic requirement for a metal center to engage in a delocalized 3-center-2-electron interaction is that it be electron-deficient; this accounts for the large number of such complexes among the early transition metals and f-elements. In particular, the existence of energetically accessible d orbitals are thought to be critical to the establishment of $\text{M}\cdots\text{Si}-\text{C}$ interactions.⁴⁴ The latter would not normally be expected in the electronically saturated ML_3 complexes of the Group 15 elements. Consequently, it was thought that the $\text{M}[\text{N}']_3$ complexes described here might serve as a type of experimental “control” in separating the effects of steric crowding (and dispersion forces) from other electronic interactions on the geometries of $\text{M}[(\text{N},\text{CH})(\text{SiMe}_3)_2]_3$ complexes.

2.2 Results and Discussion

(a) Synthesis. Tris(bistrimethylsilylamido) phosphorus, $\text{P}[\text{N}(\text{SiMe}_3)_2]_3$ (**1**), and –arsenic, $\text{As}[\text{N}(\text{SiMe}_3)_2]_3$ (**2**), were synthesized in high yield from salt elimination reactions involving phosphorus trichloride and arsenic triiodide, respectively, and three equivalents of potassium hexamethyldisilazide in THF or toluene (eq 1):



The yellow solids are soluble in polar and nonpolar organic solvents, and show no signs of decomposition after 6 weeks in an inert atmosphere at room temperature. The sterically crowded **1** can tolerate limited (ca. 2 hours) exposure to air before decomposition is noted.

(b) Crystallographic Results. P[N(SiMe₃)₂]₃ (1**).** Crystals of P[N']₃ were isolated from hexane solution as nearly colorless blocks. It crystallizes in the triclinic space group $P\bar{1}$, and is monomeric with three bis(trimethylsilyl)amide ligands arranged around the phosphorus (Figure 2a). Two crystallographically independent molecules are found in the unit cell, as was found for the bismuth analogue;²⁷ the phosphorus atom is disordered over two sites (in one molecule, in an 80/20 split; in the second, a 77/23 split). The apparent separation between P and P' is 1.358(3) Å (1.363(2) Å in the second molecule). Owing to the similarity of the two molecules, only the one containing P1 will be discussed here and listed in the tables.

The average P1–N bond length of 1.748(3) Å (1.766(5) Å for P1'–N) is somewhat shorter than that reported for the related compound {HP[N']₂}₂ (1.815(14) Å),³⁵ although the latter contains a four-coordinate P center, and might be expected to be slightly lengthened. The P–N bond in the three-coordinate Cl₂PN(SiMe₃)₂ (1.6468(8) Å),⁴⁰ is even shorter than in **1**, but this has been attributed to hyperconjugative interaction of the lone pair of the amino nitrogen atom with the antibonding σ*(P–Cl) bond orbital, leading to partial PN double bond character. A more representative comparison might be with {P[μ-N(SiMe₃)]PN(SiMe₃)₂}₂, in which the terminal

three-coordinate PN bond is 1.712 Å in length.⁵² The sum of the angles at phosphorus (318.3° at P; 315.8° at P') reflects the pyramidalization of the molecule. The inclination of the Si–N–Si' planes to the N₃ plane ranges from 49.6° to 66.5° (average 55.5°); the twist helps to minimize steric interactions.

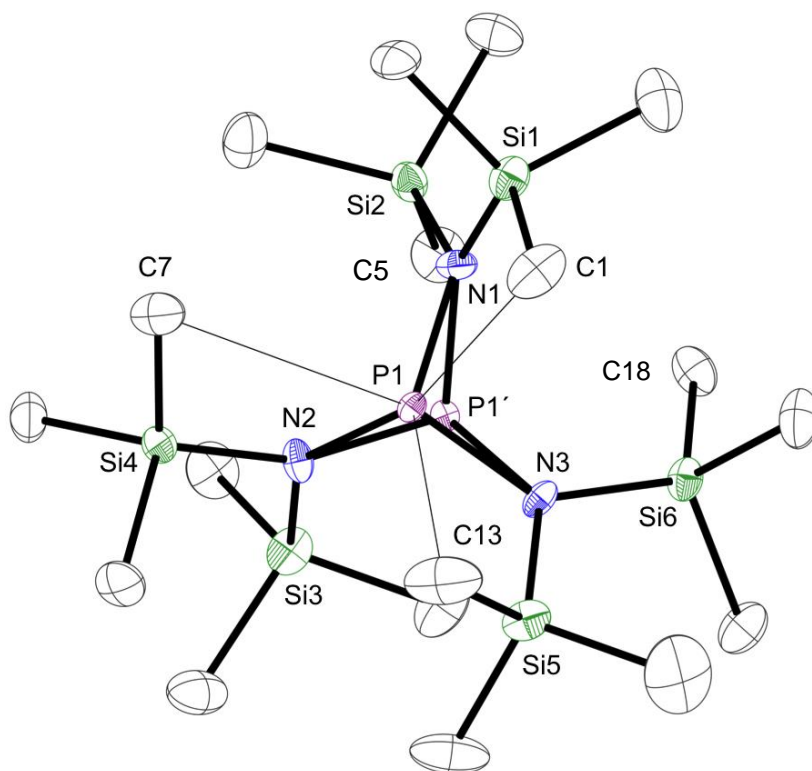


Figure 2. Thermal ellipsoid plot of non-hydrogen atoms of P[N(SiMe)₂]₃

Thermal ellipsoids are shown at the 50% level. Of the minor conformations, only the M' atoms are shown. Thin lines are drawn from M to the closest carbon contacts (see text). Selected bond distances (Å) and angles (deg): P1–N1, 1.7427(17); P1–N2, 1.7616(18); P1–N3, 1.7384(17); P1'–N1, 1.807(3); P1'–N2, 1.696(3); P1'–N3, 1.796(3); N1–P1–N2, 106.61(9); N1–P1–N3, 105.08(9); N2–P1–N3, 108.61(9); N1–P1'–N2, 106.63(15); N1–P1'–N3, 100.15(14); N2–P1'–N3, 108.96(15).

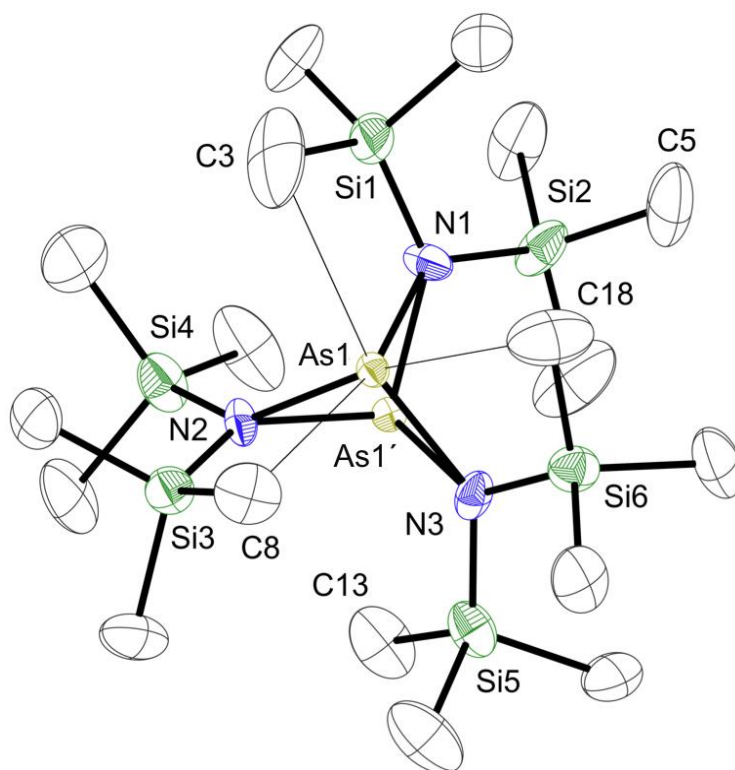


Figure 3. Thermal Ellipsoid Plot of $\text{As}[\text{N}(\text{SiMe}_3)_2]_3$

Thermal ellipsoids are shown at the 50% level. Of the minor conformations, only the M' atoms are shown. Thin lines are drawn from M to the closest carbon contacts (see text). Selected bond distances (\AA) and angles (deg): As1-N1 , 1.879(2); As1-N2 , 1.896(2); As1-N3 , 1.956(3); As1'-N1 , 1.917(2); As1'-N2 , 1.927(3); As1'-N3 , 1.903(3); N1-As1-N2 , 105.33(12); N1-As1-N3 , 103.71(11); N2-As1-N3 , 102.92(12); N1-As1'-N2 , 102.70(11); N1-As1'-N3 , 104.36(12); N2-As1'-N3 , 103.78(11). Crystals were obtained by Steven Chemly.

$\text{As}[\text{N}(\text{SiMe}_3)_2]_3$ (**2**). Crystals of $\text{As}[\text{N}']_3$ were isolated from hexane solution as nearly colorless blocks. It crystallizes in the monoclinic space group $P2_1/c$, and like **1** is monomeric with three bis(trimethylsilyl)amide ligands arranged around the arsenic (Figure 3). As is found for the other Group 15 analogues,²⁷ the arsenic atom is disordered over two sites (in the case of **2**, in a 55/45 split); the apparent separation between As and As' is 1.5980(7) \AA .

The average As–N bond length of 1.910(3) \AA (1.916(2) \AA for $\text{As}'\text{-N}$) is somewhat longer than that reported for the related compounds $\text{HAs}[\text{N}']_2$ (1.878(4) \AA),³⁵ $\text{Cp}^*\text{AsCl}[\text{N}']_2$ (1.874(2) \AA),³⁹ and $\text{Cl}_2\text{As}[\text{N}']$ (1.802(3) \AA).³⁷ This could be partly artifactual, stemming from the disorder

at the As center, but in fact the distance is close to that expected from the sum of the covalent radii (1.90 Å).⁵³ The particularly short As–N bond observed in Cl₂As[N'] has been ascribed to hyperconjugation involving the chlorine atoms, an effect obviously not possible in **2**. The sum of the angles at arsenic (312.0° at As; 310.8° at As') indicates the substantial pyramidalization present. The Si–N–Si' planes are inclined at an average angle of 48.1° from the N₃ plane, evidently to minimize steric interactions.

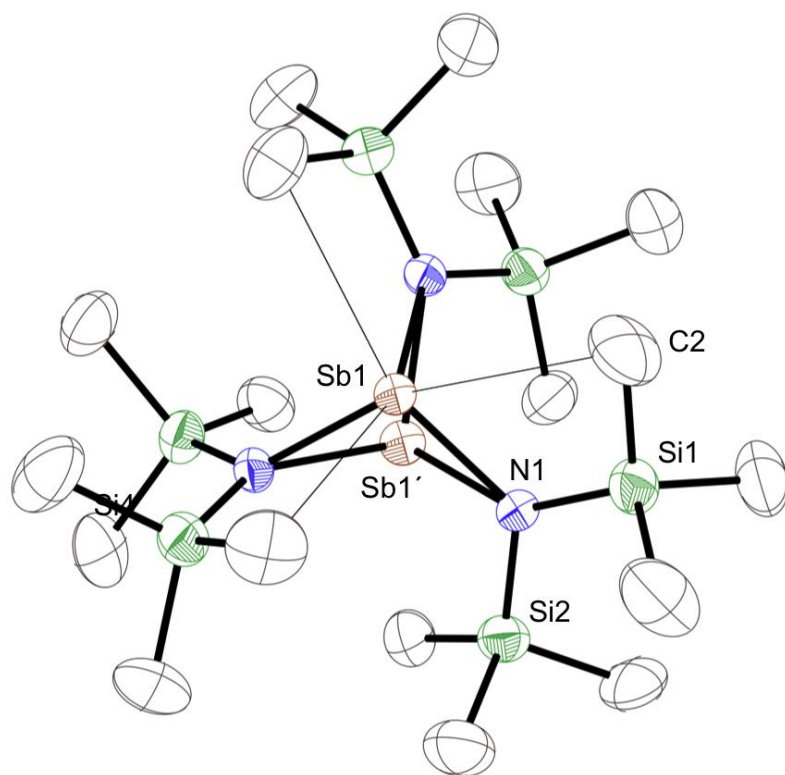


Figure 4. Thermal Ellipsoid Plot of Sb[N(SiMe₃)₂]₃

Thermal ellipsoids are shown at the 50% level. Of the minor conformations, only the M' atoms are shown. Thin lines are drawn from M to the closest carbon contacts (see text). Selected bond distances (Å) and angles (deg): Sb1–N1, 2.100(5); N1–Sb1–N1', 103.42(19); Si1–N1–Si2, 118.0(2); Sb1–N1–Si1, 108.8(2).

Sb[N(SiMe₃)₂]₃ (3**).** Compound **3** was found cocrystallized with HN' (see Experimental) and is isostructural with **1** and **2**; **3** crystallizes in the trigonal space group $P\bar{3}$, however. It has crystallographically imposed threefold symmetry, but like the other M[N']₃ complexes,²⁷ is

disordered over two sites (Figure 4). The minor contributor could not be as satisfactorily modeled as in the other cases; nevertheless, the major structural features are well defined.⁵⁴

The Sb–N bond length of 2.100(5) Å matches that expected from the sum of the covalent radii (2.10 Å),⁵³ and is also identical to that found in the cyclodiphosphazane [(PN-*t*-Bu)₂(N-*t*-Bu)₂]SbN(SiMe₃)₂.⁵⁵ Sb–N distances in several (trimethylsilyl)amido-substituted diazastiboles (2.049(3) and 2.040(3) Å) are only slightly shorter.⁵⁶ The sum of the angles at antimony in **3** (310.3°) indicates the considerable pyramidalization in the complex. It should be noted that the angle is substantially wider than in the tris(amino)stibine Sb[N(H)(C₆H₂(*t*-Bu)₃)]₃,⁵⁷ whose N–Sb–N' bond angles, which sum to 287.9°, are distorted because of the bulk of the C₆H₂(*t*-Bu)₃ groups. The heteroleptic complex (C₆F₅)₂NSb(NEt₂)₂ has an intramolecular Sb···F interaction that contributes to distortions in the N–Sb–N angles, but they also sum to a value (290.5°) that is considerably less than in **3**.⁵⁸

(c) Comparison among Group 15 M[N(SiMe₃)₂]₃ Derivatives. The ability of the –N(SiMe₃)₂ ligand to support isostructural complexes across a broad range of metal sizes is well established (e.g., in the dinuclear series {M[N(SiMe₃)₂]₂}₂ for M = Mg–Ba²²). The homoleptic Group 15 derivatives are an additional example of this ability. The complexes **1–4** are all monomeric pyramidal complexes, and the average M–N bond distances are within 0.03 Å of the sum of the appropriate covalent radii.⁵³ To a first approximation, the L–M–L' angles in sets of Group 15 ML₃ compounds are expected to become progressively closer to 90° with the heavier complexes, owing to the greater amount of *np* character in the M–L bonding. Superimposed on this is a trend originating from lessened steric repulsion between the ligands; i.e., angles typically decrease in the order P > As > Sb > Bi, reflecting the longer M–L bonds and consequently reduced interligand interaction in the heavier compounds. Thus, as hydrogen exerts little steric

demand, the Group 15 hydrides display only small H–M–H variation (93.6° (PH_3)⁵⁹ — 90.5° (BiH_3)⁶⁰), but a larger range is observed in the triphenyls (MPh_3), whose average C–M–C angles decrease from 102.8° (P)⁶¹ to 93.9° (Bi).⁶² It is notable that the average N–M–N' angles in **1–4** are both comparatively large ($>100^\circ$) and exhibit relatively little variation with the change in the central atom (106.8° (P)– 103.7° (Bi)).

The wide N–M–N values in the complexes would appear to be at least partially dictated by steric interactions between the ligands. That these molecules (and their f-element counterparts) are unquestionably crowded species can be visualized through the calculation of their G_{complex} values; this is a measure of the total steric shielding of the metal center by the coordinated ligands.⁶³ G_{complex} values are listed in Table 1 and depicted in Figure 5 for the two complexes in this study with the shortest (M = P) and longest (M = Tb) M–N bonds; that the values range from 92% to 85% indicates the high percentage of the coordination sphere occupied by the (trimethylsilyl)amido ligands. More specifically, it can be noted that there are multiple interligand Me...Me' contacts less than 4.0 \AA (the sum of the van der Waals radii⁶⁴) in the complexes; the closest Me...Me' contact in **2** is at 3.56 \AA , in **3** at 3.69 \AA , and in **4** at 3.82 \AA . Those in **1** are especially close, as short as 3.36 \AA (C5–C18).

Table 1 Selected bond distances (Å) and angles (deg) and G_{solid} values (%) in representative $M[N(\text{SiMe}_3)_2]_3$ complexes.^a In molecules with less than C_3 symmetry, average values are cited. M–N–Si, N–Si–C, and M–N–Si–C angles are those nearer the apex of the MN_3 pyramid.

Compound	M–N	N–M–N	M···C	M···Si	M–N–Si	N–Si–C	M–N–Si–C	G_{solid}	Ref.
Y[N(SiMe ₃) ₂] ₃	2.224	114.6	2.98	3.18	107.1	108.1	3.1	86.1	65
Lu[N(SiMe ₃) ₂] ₃	2.191	111.6	2.89	3.13	104.9	107.2	2.8	86.0	66
Ce[N(SiMe ₃) ₂] ₃	2.319	118.2	3.11	3.32	110.4	107.4	7.0	83.6	67
Nd[N(SiMe ₃) ₂] ₃	2.290	117.8	3.10	3.29	110.1	108.0	5.8	84.2	68
	2.243	120.0	3.30	3.40	117.7	106.1	10.0	84.4	69
Sm[N(SiMe ₃) ₂] ₃	2.284	115.5	3.00	3.24	107.6	107.6	3.9	83.5	44
	2.294	115.1	2.99	3.23	106.8	108.2	3.3	83.4	70
Tb[N(SiMe ₃) ₂] ₃	2.333	113.0	2.92	3.18	106.1	107.3	2.0	85.3	71
Dy[N(SiMe ₃) ₂] ₃	2.212	114.6	2.97	3.18	107.4	107.8	2.5	84.9	72
Er[N(SiMe ₃) ₂] ₃	2.211	113.4	2.94	3.15	106.1	108.8	0.6	84.9	72
Yb[N(SiMe ₃) ₂] ₃	2.183	114.5	2.98	3.16	107.4	108.2	2.6	85.6	73
U[N(SiMe ₃) ₂] ₃	2.320	116.2	3.04	3.29	108.2	107.7	5.6	81.6	74
Pu[N(SiMe ₃) ₂] ₃	2.315	114.0	2.97	3.23	105.9	108.3	3.0	82.7	75
P[N(SiMe ₃) ₂] ₃	1.748	106.8	3.14	2.83	106.7	114.2	25.4	92.2	this work
As[N(SiMe ₃) ₂] ₃	1.910	104.0	2.95	2.88	103.3	113.7	3.1	89.0	this work
Sb[N(SiMe ₃) ₂] ₃	2.100	103.4	3.19	3.15	108.8	112.6	9.9	81.6	this work
Bi[N(SiMe ₃) ₂] ₃	2.218	103.7	3.14	3.19	106.6	113.0	4.4	79.1	work ²⁷

^aOnly the M–N and N–M–N values have been reported for M = Sc and Eu complexes;⁷⁶ they have been omitted from this compilation.

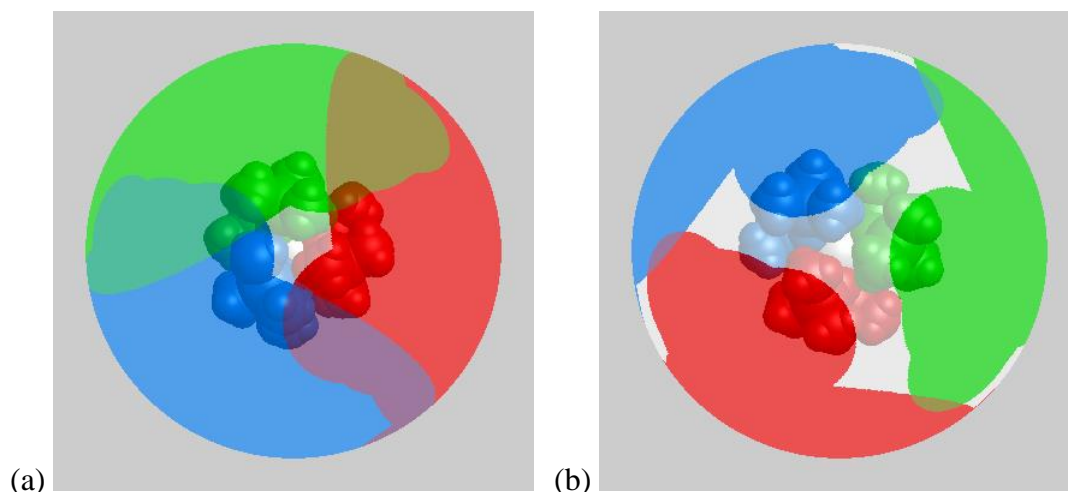


Figure 5. Solid-G visualization of $P[N(SiMe_3)_2]_3$ and $Tb[N(SiMe_3)_2]_3$.

(a) Visualization of the extent of coordination sphere coverage of $P[N']_3$, using crystallographic coordinates and the program Solid-G.⁶³ The view is from the bottom of the MN_3 pyramid. (b) The same for the complex $Tb[N']_3$. The G_{complex} value takes into account the net coverage; regions of the coordination sphere where the projections of the ligands overlap are counted only once.

There are consistently observed distortions in the $-N(SiMe_3)_2$ ligands in the Group 15 compounds that are not present in less sterically congested species. For example, in **2**, the As and C3, C8, and C18 atoms are at distances of 2.93, 2.99, and 2.92 Å, respectively; all other carbons are over 3.9 Å from the arsenic (in the related $HAs[N']_2$,³⁵ the closest $As\cdots C$ contact is at 3.39 Å). In addition, the As–N–Si angles involving these carbons are 102.8(1)°, 104.8(1)°, 102.3(1)°, respectively, consistent with the orientation of the carbon atoms toward the arsenic (none of the comparable angles in $HAs[N']_2$ is less than 117°). The As–N–Si–C torsion angles involving the close carbons in **2** are 3.9° or less. The evidence for similar orientations in **3** and **4** is almost as strong; the closest $Sb\cdots C$ and $Bi\cdots C$ contacts are at 3.19 Å and 3.13 Å, respectively, for example, and the corresponding M–N–Si angles are 108.8(2)°, and 106.1°, respectively. Reflecting the even larger amount of steric crowding in **1**, the pattern of ligand distortions is modestly different from the three heavier complexes. For example, although there is a close

P...C contact at 3.08 Å, the P–N–Si–C torsion angle involving that carbon is 13.6°, nearly 10° more than in **2** (3.9°). In general, however, the pattern of ligand distortions is similar in all four compounds, and is comparable to that observed in the complexes of the f-elements (see below).

(d) Bonding and structure in M[(N,CH)(SiMe₃)₂]₃ complexes. Despite the differences in the regions of the periodic table from which the pyramidal M[N']₃ and related M[CH(SiMe₃)₂]₃ complexes originate, they share certain structural features that can be use useful in discussing their bonding.

i. Absence of M...H–C agostic bonding. There are characteristic values for M...H distances (1.8–2.3 Å) and M...H–C angles (90–140°) that can be expected for agostic interactions,⁷⁷ but in the available crystal structures of M[N']₃ and M[CH(SiMe₃)₂]₃ complexes, hydrogen atoms have been inserted in calculated positions and refined using a riding model. Owing to such constraints on the geometry of C–H bond, the significance that can be placed on the final M...H distances and M...H–C angles is limited. Nevertheless, in a study of the structure and bonding in Sm[N']₃,⁴⁴ a detailed analysis of the metal-ligand geometry led the authors to determine that, despite the existence of short Sm...H contacts, “attractive interactions with the γ-C–H bonds are not present. These interactions are in fact *repulsive*” [italics added]. A similar conclusion was reached for La[CH(SiMe₃)₂]₃⁴³ and the titanium amide Ti₂Cl₆[N(*t*-Bu)₂]₂,⁵¹ and for the complexes (C₅Me₅)La[CH(SiMe₃)₂]₂⁷⁸⁻⁸¹ and (C₅Me₅)Y(OC₆H₃(*t*-Bu)₂)[CH(SiMe₃)₂],⁸¹ in which neutron diffraction experiments enabled the accurate location and refinement of hydrogen atom positions.

Tellingly, the same arrangements of the central element and ligand hydrogens are present in the Group 15 complexes; e.g., the hydrogen atoms bound to the γ -carbons of the $[\text{N}(\text{SiMe}_3)_2]^-$ ligands are oriented so as to *maximize* their distances to the metal center. The dihedral $\text{As}\cdots\text{Si}-\text{C}-\text{H}$ angles in **2**, for example, are in the range from $54\text{--}66^\circ$, and not near zero, which would be expected if there were attractive $\text{As}\cdots\text{H}$ interactions; comparable values are found in the other complexes.

ii. Evidence for $\text{M}\cdots\text{Si}-\text{C}$ interactions. There are several structural criteria that have been cited as evidence for $\text{M}\cdots(\beta\text{-Si}-\text{C})$ interactions in $\text{M}[\text{N}']_3$ and $\text{M}[\text{CH}(\text{SiMe}_3)_2]_3$ complexes, including distorted $\text{M}-(\text{N},\text{CH})-\text{Si}$ and $(\text{N},\text{CH})-\text{Si}-\text{Me}$ angles, small $\text{M}-(\text{N},\text{CH})-\text{Si}-\text{Me}$ torsion angles (this is less notable with the nonplanar $-\text{CH}(\text{SiMe}_3)_2$ ligands), elongated $\text{Si}-\text{Me}$ bonds for the carbon interacting with the metal, relatively short $\text{M}\cdots\text{Si}$ contacts, and the placement of one or more of the carbon atoms close ($\sim 3 \text{ \AA}$) to the metal atom. The existence of these structural features are more reliably established than are the location of hydrogen atoms in X-ray crystal structures, and most are included in the tabulation in Tables 1 (for $\text{M}[\text{N}']_3$ complexes) and 2 (for $\text{M}[\text{CH}(\text{SiMe}_3)_2]_3$ complexes).⁸²⁻⁸³ The discussion below will focus primarily on the amido complexes, although similar comments can be made for the alkyl species.

These distortions and contacts are not completely independent. For example, compared to complexes with longer $\text{M}-\text{N}$ bonds (Figure 6a), those with shorter $\text{M}-\text{N}$ bonds would be expected to have closer contacts between the basal TMS groups, which would have the effect of tilting the ligands toward the more open apex side of the MN_3 pyramid (Figure 6b). The “upper” $\text{M}-\text{N}-\text{Si}$ angle would thereby be compressed, and the silicon atom (and an attached methyl group) would be pushed closer to the metal.

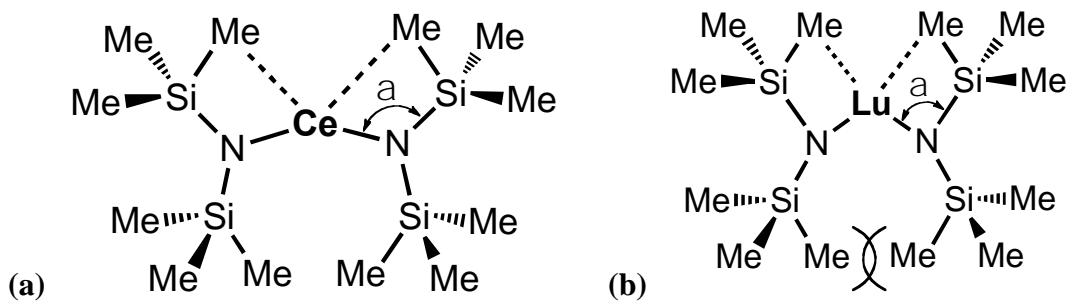


Figure 6. Relationship between various bond distances and intramolecular contacts in $M[N(SiMe_3)_2]_3$ complexes, using Ce and Lu complexes as examples

(a) In $Ce[N']_3$, the M–N distance is 2.319 Å, the N–Ce–N is 118.2°, and the angle α is 110.4°; the corresponding $Ce \cdots C(H_3)$ contact is at 3.11 Å. (b) In $Lu[N']_3$, the Lu–N distance is shortened to 2.191 Å, the N–Lu–N angle has narrowed to 111.6°, as has the angle α to 104.9°; the accompanying $Lu \cdots C(H_3)$ contact is now at 2.98 Å.

Table 2 Selected bond distances (Å) and angles (deg) and G_{solid} values (%) in representative $M[\text{CH}(\text{SiMe}_3)_2]_3$ complexes. In molecules with less than C_3 symmetry, average values are cited. M–C–Si, N–Si–C(H₃), and M–C–Si–C(H₃) angles are those nearer the apex of the MC_3 pyramid.

Compound	M–C	C–M–C	M···C(H ₃)	M···Si	M–C–Si	C–Si–C(H ₃)	M–C–Si–C(H ₃)	G_{solid}	Ref.
Y[CH(SiMe ₃) ₂] ₃	2.353	108.6	2.96	3.28	102.1	106.6	12.4	85.0	84
	2.357	108.1	2.95	3.28	101.7	106.3	13.1	84.6	85
La[CH(SiMe ₃) ₂] ₃	2.516	109.3	3.12	3.41	101.9	109.7	13.9	79.8	86
Ce[CH(SiMe ₃) ₂] ₃	2.475	110.1	3.07	3.39	102.8	108.2	11.8	82.0	84
Sm[CH(SiMe ₃) ₂] ₃	2.332	110.2	3.04	3.33	106.6	105.2	14.4	84.9	86
U[CH(SiMe ₃) ₂] ₃	2.486	107.6	3.10	3.37	101.7	109.5	16.2	82.9	87
Bi[CH(SiMe ₃) ₂] ₃	2.328	102.9	3.48	3.40	106.6	113.0	29.0	78.7	88

For the f-element $M[N']_3$ complexes, there is in fact a strongly linear relationship between the N–M–N angle and the closest $M\cdots C(H_3)$ distance (Figure 7). Interestingly, the comparable angle/distance relationship for the heaviest Group 15 complexes falls on a nearly vertical line, owing to the much smaller spread in the N–M–N angles; the highly congested compound **1** falls somewhat off the line of the heavier compounds. Also notable is the lack of strong C(H)–M–C(H) and M–C distance correlation in the f-element $M[CH(SiMe_3)_2]_3$ complexes, perhaps a consequence of the longer M–C vs. M–N bond lengths, and an ability of the nonplanar $[CH(SiMe_3)_2]^-$ anion to pack around the metal centers in a way that does not occur for the planar $[N(SiMe_3)_2]^-$ ligand. Perhaps coincidentally, the value for $Bi[CH(SiMe_3)_2]_3$ is on the line observed with the Group 15 $M[N']_3$ complexes.

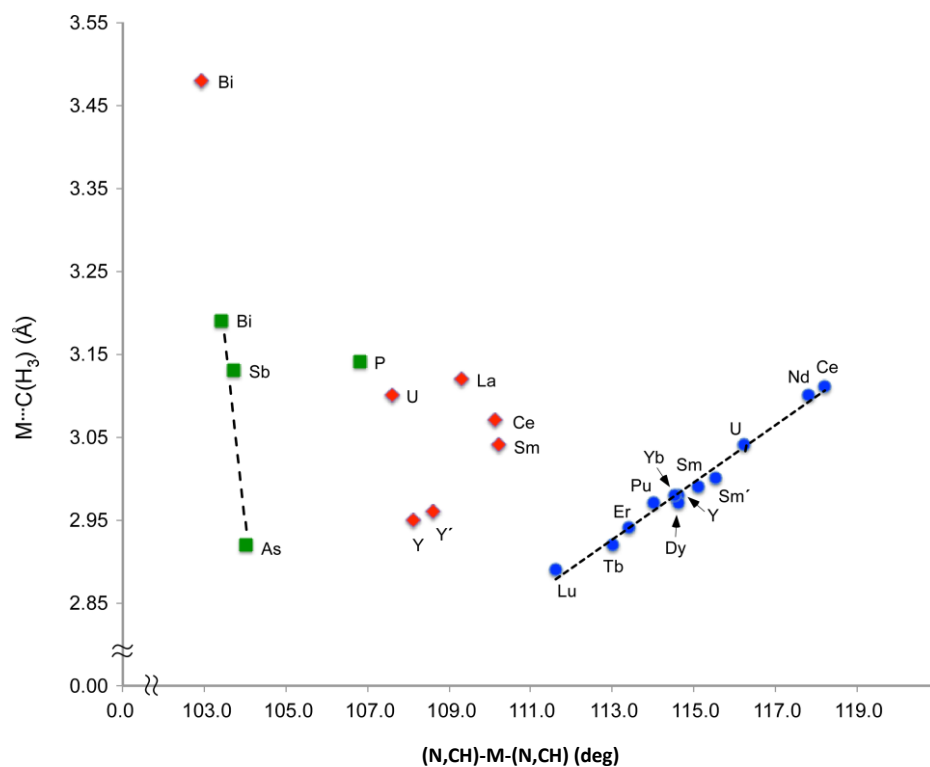


Figure 7. Relationship between (N,CH)–M–(N,CH) angles and closest intramolecular M···C(H₃) contacts in M[N(SiMe₃)₂]₃

Relationship between (N,CH)–M–(N,CH) angles and closest intramolecular M···C(H₃) contacts in M[N(SiMe₃)₂]₃ (M = f-element (blue); Group 15 (green)) and M[CH(SiMe₃)₂]₃ (red) complexes. The red symbols for Y and Y' are from ref. ⁸⁵ and ⁸⁴, respectively; those for the blue Sm and Sm' are from ref. ⁷⁰ and ⁴⁴, respectively. The least squares line drawn for the f-element M[N(SiMe₃)₂]₃ complexes has $r^2 = 0.98$; the line for (As–Bi)[N(SiMe₃)₂]₃ has $r^2 = 0.91$.

In general, the main-group complexes are more strongly pyramidal than the f-element compounds (average N–M–N of 104.5° and 114.9°, respectively), and the N–Si–C angles average to 113.4° for the Group 15 compounds, but to a smaller 107.5° for the f-element counterparts. Given the considerably different M–N bonding in the complexes (largely covalent in the Group 15 complexes; much more polar, even if not completely electrostatic, in the f-element counterparts), however, there is a substantial degree of structural similarity between the complexes.

iii. Computational investigations and steric effects. The difference in the electronic nature of the central elements in the $M[N']_3$ complexes, especially considering the expected lack of energetically relevant acceptor orbitals in **1–4**, suggests that intramolecular crowding is a likely source of some of the structural similarities. This is not a completely new proposal; for example, the inequality in the $M-(N,CH)-Si$ angles in the f-element complexes has previously been suggested to be partially the result of steric effects, independent of explicit orbital interactions.⁴⁴

As a starting point in a computational examination of this issue, we used the molecular mechanics force field UFF⁸⁹ as a tool to estimate the extent to which the structural features of the $M[(N,CH)(SiMe_3)_2]_3$ complexes might be generated from steric (and dispersion) interactions. $Pu[N']_3$, $Ce[CH(SiMe_3)_2]_3$, and $Sb[N']_3$ (**3**) were selected as representative examples for actinide, lanthanide, and Group 15 metal centers; Table 3 lists the results.

Table 3 Selected Experimental and UFF Optimized Bond Distances (Å) and Angles (deg) for Pu[N(SiMe₃)₂]₃, Ce[CH(SiMe₃)₂]₃, and Sb[N(SiMe₃)₂]₃.

		Pu[N(SiMe ₃) ₂] ₃	Ce[CH(SiMe ₃) ₂] ₃	Sb[N(SiMe ₃) ₂] ₃
M–(N,CH)	(exp.)	2.315(10)	2.475(7)	2.100(5)
	(calc.)	2.287	2.512	2.107
M···Si	(exp.)	3.23	3.38	3.15
	(calc.)	3.25	3.39	3.19
M···C	(exp.)	2.968(9)	3.068(7)	3.19
	(calc.)	3.04	2.98	3.25
(N,CH)–M–(N,CH)	(exp.)	113.97(5)	110.08(16)	103.42(19)
	(calc.)	101.1	104.6	100.8
M–(N,CH)–Si	(exp.)	105.9(2)	102.8(3)	108.8(2)
	(calc.)	108.4	100.5	109.4
(N,CH)–Si–C	(exp.)	108.3(4)	108.2(4)	112.6(3)
	(calc.)	107.9	105.6	113.4
M–(N,CH)–Si–C	(exp.)	3.0	11.8	9.9
	(calc.)	10.0	19.8	9.6

In general, the distances between directly bonded atoms are more reliably modeled with MM methods than are the corresponding angles, and the M–(N,CH) bond lengths are calculated to be within 0.04 Å of their respective experimental values. The relatively limited parameterization of the heavy metal centers, their low coordination numbers, and in the case of the amido complexes, the failure of the UFF method to capture M–N π interactions that may be present⁹⁰ is perhaps responsible for the overpyramidalization of the (N,CH)–M–(N,CH) angles; the error, not surprisingly, is least with the Sb complex (2.6°). Nevertheless, although possibly benefitting from some error cancellation,⁹¹ the long-range contacts are reasonably well represented; the M···Si and M···C distances are overestimated, but by a maximum of 0.04 Å for M···Si (in **3**) and a maximum of 0.09 Å for M···C (in the Ce complex). Considering the approximate nature of the modeling, the structures are represented surprisingly well, especially that of **3**, where the shorter Sb–N bonds and consequently tighter

intramolecular packing limits the conformational flexibility of the ligands (note that the M–N–Si–C torsion angle is reproduced to within 0.3° of the experimental value in **3**, whereas in Ce[CH(SiMe₃)₂]₃, with the longest metal-ligand bonds of the three compounds, the comparable M–(CH)–Si–C angle deviates by 8.0°).

Although any molecular mechanics representation has substantial limitations, the fact that simply holding three –(N,CH)(SiMe₃)₂ groups together around a central metal within the influence of an orbital-free force field can reproduce several of the major features of the complexes suggests that the MM approach is capturing a critical contributor to their structures; i.e., steric congestion and van der Waals (dispersion) interactions.⁹² This is not meant to imply that attractive M···Si–C interactions do not exist in f-element M[N']₃ and M[CH(SiMe₃)₂]₃ complexes. Compelling arguments have been made for their presence in these compounds, both from high-level computational results and from reactivity considerations (e.g., decomposition of Lu[N']₃ under ALD conditions, even with H₂O as a reagent, always leads to Lu silicate films, a fact that has been attributed to the existence of Lu···Si interactions that help remove Si and Lu together from the compound during decomposition⁶⁶).

A detailed DFT examination of the role of valence d orbitals in the geometry of the f-element Sm[N(SiR₂Me)(SiR₃)]₃ (R = Me, H) complexes has been previously reported, with particular attention given to the effect on the Sm–N distance, N–Sm–N angle, and the planarity of the [N(SiMe₃)₂][–] ligand (the latter by removing the d functions from the basis set for the silicon atoms).⁴⁴ We undertook a similar study with the M[N']₃ (M = P–Bi) complexes, with a focus on the accessibility of d acceptor orbitals on the Group 15 centers that could conceivably support M···Si–C interactions. Table 4 lists a selection of bond lengths, angles

and intramolecular contacts for the four main-group amido complexes, calculated both with and without valence d orbitals on the central atom (using the LANL08(d)⁹³⁻⁹⁴ and LANL08⁹⁵ ECP basis sets on the central atoms, respectively, and the M06-L functional⁹⁶). By way of generalization, it can be said that the inclusion of d polarization functions improves the reproduction of the M–N distances slightly; the effect is largest for P (0.04 Å shortening) but is essentially negligible for Sb and Bi (< 0.01 Å change). The N–M–N angles display less alteration on the addition of d functions: that for P widens by 0.2°, but there is no effect in the Bi derivative. Non-bonded distances are consistently overestimated, by up to 0.2 Å in the case of the As···Si and As···C contacts; the addition of d functions does not change the As···C distance, and shortens the As···Si by only 0.01 Å. For P, the addition of a d function shortens the P···Si contact by 0.03 Å, but still leaves it 0.09 Å longer than the experimental value. In summary, at this level of theory the inclusion of d functions has small to negligible effects on the geometries of the M[N']₃ complexes. This is in contrast to their large influence on the calculated structure of Sm[N(SiH₂Me)(SiH₃)]₃, for example, in which the removal of the d function on the metal causes the Sm–N bond length to increase by 0.074 Å, and the N–Sm–N angle to increase by 5.3°, leading to a nearly planar molecule (N–Sm–N = 119.4°).⁴⁴

Table 4. Selected experimental and DFT optimized bond distances (Å) and angles (deg) for E[N(SiMe₃)₂]₃ (E = P–Bi). Basis set for “calc. w/o *d*” is LANL08 (E); def2SVP (C,H,N,Si); for “calc. w/*d*” is LANL08(d) (E); def2SVP (C,H,N,Si).

		P[N(SiMe ₃) ₂] ₃	As[N(SiMe ₃) ₂] ₃	Sb[N(SiMe ₃) ₂] ₃	Bi[N(SiMe ₃) ₂] ₃
M–N	(exp.)	1.748(3)	1.910(3)	2.100(5)	2.218(13)
	(calc. w/o <i>d</i>)	1.821	1.926	2.099	2.183
	(calc. w/ <i>d</i>)	1.781	1.913	2.101	2.186
M···Si	(exp.)	2.83	2.88	3.15	3.19
	(calc. w/o <i>d</i>)	2.95	3.08	3.23	3.29
	(calc. w/ <i>d</i>)	2.92	3.07	3.23	3.29
M···C	(exp.)	3.14	2.95	3.19	3.14
	(calc. w/o <i>d</i>)	3.18	3.15	3.25	3.24
	(calc. w/ <i>d</i>)	3.20	3.15	3.25	3.24
N–M–N	(exp.)	106.8(2)	104.0(2)	103.42(19)	103.7(5)
	(calc. w/o <i>d</i>)	105.9	103.6	102.2	103.1
	(calc. w/ <i>d</i>)	106.1	103.5	102.1	103.1
M–N–Si	(exp.)	106.7(2)	103.3(2)	108.8(2)	106.6(7)
	(calc. w/o <i>d</i>)	109.4	112.1	112.9	112.3
	(calc. w/ <i>d</i>)	109.3	112.1	112.8	112.2
N–Si–C	(exp.)	114.2(2)	113.7(3)	112.6(3)	113.0(1.1)
	(calc. w/o <i>d</i>)	111.1	109.8	110.3	109.8
	(calc. w/ <i>d</i>)	111.8	109.9	110.2	109.6
M–N–Si–C	(exp.)	25.4	3.1	9.9	4.4
	(calc. w/o <i>d</i>)	26.1	5.9	5.6	2.3
	(calc. w/ <i>d</i>)	27.6	6.2	5.5	2.1

An analysis of the molecular orbitals in the Group 15 and f-element $M[N']_3$ complexes illustrates the difference in the involvement of d orbitals in their bonding. To a first approximation, all the compounds can be regarded as possessing C_3 symmetry (this approximation is poorest for **1**, as the 17° variation in the inclination of the Si–N–Si' planes to the N_3 plane attests). All four main group complexes, and for comparison, the f-element complex $Lu[N(SiMe_3)_2]_3$, were optimized at the BP86-D3(BJ)/TZV2P level, and the percent character of various frontier orbitals, determined with a standard Mulliken analysis, is listed in Table 5. For **1–4**, the HOMO contains significant p orbital character, reflecting the conventional lone pair on the central Group 15 centers. On descending the column, the energy gap between the N 2p orbitals and the valence np orbitals increases, and the ordering of the energy levels and the extent of mixing changes. For the complexes **2–4**, the energy gap is such that both the HOMO and next two frontier orbitals form a set (a + e symmetry) that contain significant N lone pair character as well, and which could potentially be involved in π -type bonding with the metal d orbitals. There is, however, almost negligible overlap with the metals' d orbitals in the main-group complexes (a maximum of 1.2% in **2**). In contrast, somewhat more d orbital involvement is apparent in the frontier orbitals in $Lu[N(SiMe_3)_2]_3$, which, however, largely represent the N lone pairs. The HOMO a-type orbital displays only a small amount of d orbital character (1.7% from the $5d_{z^2}$ orbital), but the e-type orbitals have 5.8% 5d orbital involvement.

Table 5 Percent Mulliken contribution of various atomic orbitals in the relevant MOs of compounds 1-4 and Lu[N(SiMe₃)₂]₃

AO	P[N(SiMe ₃) ₂] ₃				As[N(SiMe ₃) ₂] ₃			
	HOMO	HOMO-1	HOMO-2	HOMO-3	a (LP)	e (LP)	a (σ)	e (σ)
-E (au)	0.155	0.212	0.217	0.222	0.172	0.211	0.234	0.250
M(s)	18.3	1.1	0.0	4.5	10.9	0.0	7.59	0.0
M(p)	28.0	3.7	0.0	10.9	12.6	0.0	19.04	0.68
M(d)	0.0	1.5	1.3	0.0	1.2	0.74	0.0	0.0
N(tot) ^a	38.9	51.3	51.4	37.2	52.9	54.5	25.8	3.6
Si(p) ^b	0.0	0.0	0.0	1.0	0.0	0.0	2.31	12.7
Si(d) ^b	0.0	0.0	1.2	2.8	0.0	1.2	0.0	0.54

AO	Sb[N(SiMe ₃) ₂] ₃				Bi[N(SiMe ₃) ₂] ₃			
	a (LP)	e (LP)	a (σ)	e (σ)	a (LP)	e (LP)	a (σ)	e (σ)
-E (au)	0.178	0.209	0.228	0.250	0.182	0.209	0.226	0.250
M(s)	14.9	0.0	9.6	0.0	15.8	0.0	9.2	0.0
M(p)	12.3	0.0	20.0	1.8	11.3	0.0	20.3	2.4
M(d)	0.0	0.7	0.0	0.0	0.0	0.6	0.0	0.0
N(tot) ^a	49.0	54.2	26.5	6.3	47.8	54.9	33.1	9.9
Si(p) ^b	0.0	0.0	0.0	11.9	0.0	0.0	0.0	12.1
Si(d) ^b	0.0	0.0	0.0	1.1	0.0	1.8	0.0	0.0

AO	Lu[N(SiMe ₃) ₂] ₃			
	a (LP)	e (LP)	e (σ)	a (σ)
-E (au)	0.194	0.203	0.228	0.229
Lu(s)	0.0	0.0	0.0	3.3
Lu(p)	0.0	0.0	0.0	0.0
Lu(d)	1.7	5.8	5.7	1.2
N(tot) ^a	57.8	53.9	34.3	35.7
Si(p) ^b	0.0	0.0	3.1	2.1
Si(d) ^b	0.0	1.2	0.8	0.0

^aTotal for all three N atoms and for all N functions. ^bTotal for all six Si atoms (only p and d functions).

The second set of frontier orbitals in **2-4** and Lu[N']₃ comprise M-N σ bonding orbitals (a + e), for which there is no measurable overlap with the d orbitals of the Group 15

elements. This is consistent with the negligible change in M–N bond length in the calculated $M[N']_3$ structures in the absence of the d functions on the metal. In $Lu[N']_3$, the second e set lies slightly higher in energy than the a orbital, but together, they represent 6.9% overlap with the 5 d orbitals.

Attention should be given here to the orbitals in **1**; owing to its functionally lower symmetry than the other compounds, the four highest frontier orbitals are all singly degenerate, and listed as HOMO- x in Table 5. The ordering is somewhat different from that in the heavier Group 15 species, as the HOMO has more than twice the amount of p character (28%) as does that in the heavier analogues. The greater extent of P/N mixing also means that the N lone pairs are not as distinctly identifiable, and HOMO-(1-3) represent P–N σ bonding orbitals. As was found for the other main group complexes, however, the general comments above still apply as regards d orbital participation (i.e., negligible).

A final comment can be made about the LUMO in all the molecules. For **1-4**, there is no metal d character in the LUMOs. That for **3** is illustrated in Figure 8a; it consists only of various s and p orbitals (e.g., 40.9% 5p, 11.5% 5s, plus others). In contrast, more d orbital involvement is apparent in the LUMO of $Lu[N']_3$ (Figure 8b); the primary component (53.0%) is the $5d_{z^2}$ orbital; the second largest component (19.2%) is from the 6s orbital.

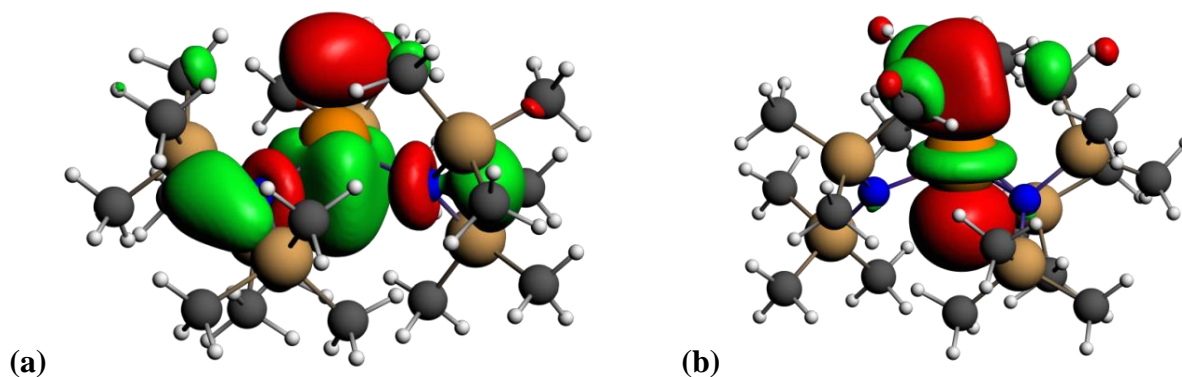


Figure 8. Depiction of the LUMO of $\text{Sb}[\text{N}(\text{SiMe}_3)_2]_3$ (a) and $\text{Lu}[\text{N}(\text{SiMe}_3)_2]_3$ (b). The Sb LUMO has 41% 5p character; the Lu is 53% 5d₂.

An alternative investigation of the possible importance of $\text{M}\cdots\text{Si}-\text{C}$ interactions in the Group 15 complexes was conducted with Bader's atoms in molecules (AIM) theory.⁹⁷ Bond critical paths and points were calculated for **1-4** and $\text{Lu}[\text{N}']_3$, using the BP86-D3(BJ)/TZV2P optimized structures. Figure 9a illustrates the fact that three bond critical paths are clearly evident between the metal and the γ -C atoms in $\text{Lu}[\text{N}']_3$. The average electron density (in au) at the critical points along the paths is 0.018, 3 times the value for the points along the paths that represent van der Waals interactions between the methyl groups (e.g., the density of those in the triangle above the Lu atom average 0.0055 au); these are values appropriate for agostic-type interactions.⁹⁸ Ring critical points, which are indicative of electron delocalization in space, are associated with the $\text{Lu}\cdots\text{C}$ bond critical paths, and are shifted toward the silicon atoms. In contrast, there are no bond critical paths or points between the Group 15 elements and the β -Si or γ -C atoms in **1-4**. The diagram for $\text{Sb}[\text{N}']_3$ is shown in Figure 9b; that for the other three complexes looks essentially the same.

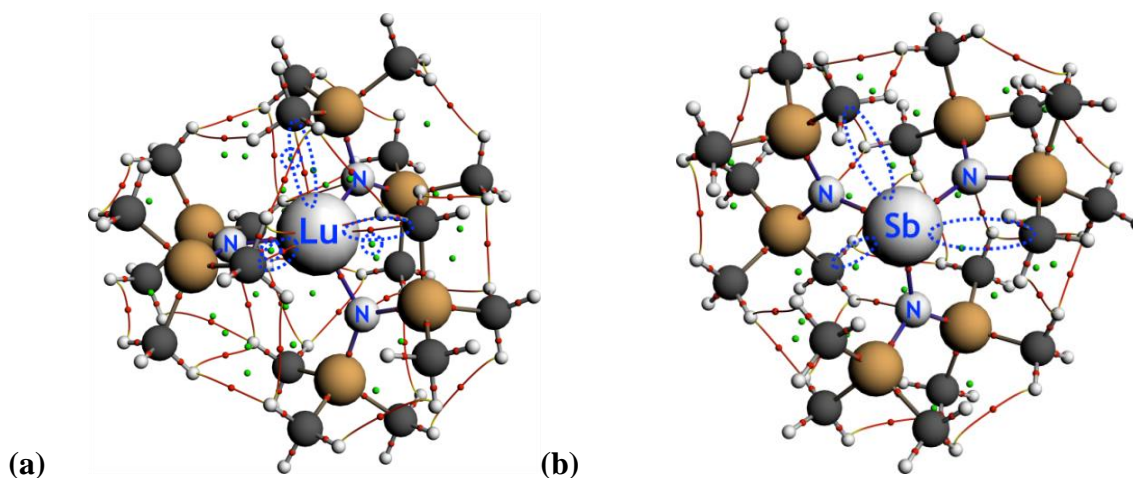


Figure 9. AIM representations for Lu[N(SiMe₃)₂]₃ and Sb[N(SiMe₃)₂]₃

AIM representations for Lu[N(SiMe₃)₂]₃ (**a**) and Sb[N(SiMe₃)₂]₃ (**b**). Bond critical points are in red, and ring critical points are in green. In (**a**), the bond critical paths from the γ -carbons to the metal are outlined with dashed ellipses; neighboring ring critical points are circled. The corresponding paths are absent in (**b**); the ellipses outline the area where they would be expected to occur, were the interactions the same as in **a**.

These results reinforce the supposition that the geometric distortions present in the Group 15 M[N']₃ complexes are not the result of M \cdots Si–C interactions or d-orbital involvement, but are the consequence of severe steric crowding. It therefore seems likely that similar geometric distortions that have sometimes been uncritically cited as diagnostic of M \cdots Si–C interactions in f-element M[(N,CH)(SiMe₃)₂]₃ complexes are also sterically induced products of the crowded metal coordination environments in the complexes, and that consequently the role of intramolecular attractions on their geometries has been given more weight than is wholly warranted.

2.3 Conclusions

The three complexes P[N']₃, As[N']₃, and Sb[N']₃ complete the series of structurally authenticated Group 15 tris(bistrimethylsilyl)amides; they are all pyramidal, monomeric

species that exhibit disorder at the metal site. Collectively they display a notable resemblance to the f-element $M[N']_3$ (and $M[CH(SiMe_3)_2]_3$) counterparts, which are also pyramidal and display a pattern of bond length changes and intramolecular contacts that have been attributed to $M\cdots Si-C$ interactions.

Nevertheless, when three $-(N,CH)(SiMe_3)_2$ ligands are arranged around a central atom in a pyramidal manner (either because of polarization/d-orbital effects (as with the f-element examples)⁹⁹ or because of near exclusive use of np orbitals in the M-L bonding (in the Group 15 cases)), the ligands will for steric reasons adopt conformations that distort the symmetrical $M-(N,CH)(SiMe_3)_2$ linkages. The consequence will be the generation of small $M-(N,CH)-Si$ and $N-Si-C$ angles, and the placement of one or more of the carbon atoms close to the central atom. Such distortions are not observed in cases of planar $M[N']_3$ complexes (e.g., the Group 13 (Al-Tl)¹⁰⁰⁻¹⁰³ or transition metal (Ti, Mn, Fe, Co)¹⁰⁴⁻¹⁰⁶ compounds), as the same amount of crowding is not present. Similar distortions are also not present in the less crowded $HAs[N(SiMe_3)_2]_2$,³⁵ even though the structure is pyramidal. In the absence of supporting spectroscopic (NMR, IR), computational, or reactivity evidence, considerable caution should be employed when relying solely on structural criteria to posit the existence of intramolecular agostic or related 3-center bonding arrangements in low-coordinate, but sterically congested metal complexes. As noted before, mere proximity is not a guaranteed marker of attractive interactions.⁵¹

2.4 Experimental Section

General Considerations. All manipulations were performed with the exclusion of air and moisture using high vacuum, Schlenk, or glovebox techniques. Proton and carbon

($^{13}\text{C}\{^1\text{H}\}$) NMR spectra were obtained on a Bruker DRX-500 or DRX-400 spectrometer at 500 or 400 (^1H) and 100.1 (^{13}C) MHz, and were referenced to the residual proton and ^{13}C resonances of C_6D_6 or THF-d_8 . Elemental analysis was performed by ALS, Tucson, AZ.

Materials. AsI_3 as purchased from Aldrich and was visibly contaminated with purple iodine crystals. It was subsequently rinsed with hexane and the remaining dark orange solid was dried under vacuum and used without further purification. $\text{K}[\text{N}']$ and PCl_3 were purchased from commercial suppliers and used as received. Toluene and hexanes were distilled under nitrogen from potassium benzophenone ketyl.¹⁰⁷ Anhydrous THF was stored over molecular sieves. C_6D_6 was vacuum distilled from Na/K (22/78) alloy and stored over type 4A molecular sieves prior to use. $\text{Sb}[\text{N}']_3$ was synthesized by halide metathesis following the literature procedure,²⁹ using $\text{K}[\text{N}']$ in place of $\text{Li}[\text{N}']$.

Synthesis of $\text{P}[\text{N}(\text{SiMe}_3)_2]_3$ (1**).** $\text{K}[\text{N}']$ (2.31 g, 11.6 mmol) was dissolved in THF (70 mL). To this, PCl_3 (0.529 g, 3.85 mmol) was added dropwise over the course of 5 min at room temperature. After 1.5 h of stirring, the yellow suspension was filtered over a medium porosity frit. All volatiles were removed from the yellow filtrate to afford **1** as a waxy yellow solid (1.43 g, 72%). Colorless X-ray quality crystals were obtained by slow evaporation of a hexane solution of **1**. Anal. Calcd (%) for $\text{C}_{18}\text{H}_{54}\text{N}_3\text{PSi}_6$: C, 42.22; H, 10.63; N, 8.20; P, 6.05. Found (average of two determinations): C, 37.21; H, 8.96; N, 7.48, P, 5.40. Although all the values are low, their molar ratios are $\text{C}_{17.8}\text{H}_{51.0}\text{N}_{3.1}\text{P}_{1.0}$, close to the expected values.¹⁰⁸⁻¹⁰⁹ ^1H NMR (400 MHz, C_6H_6 , 298 K): δ 0.42. $^{13}\text{C}\{^1\text{H}\}$ NMR (100 MHz, C_6D_6 , 298 K): δ 6.86; ^{31}P NMR (162 MHz, C_6H_6 , 298 K): δ 136.0.

Synthesis of **1** was also attempted using PI₃. K[N'] (3 equiv) was dissolved in THF. A solution, PI₃ (1 equiv) was added slowly over the course of 5 minutes. After 1.5 h of stirring, the yellow suspension was filtered over a medium porosity frit. All volatiles were removed from the yellow filtrate to afford **1** as yellow oil. This product had noticeable contamination in the ³¹P NMR which can be explained by purple crystals in the PI₃ which is likely I₂ contamination. This process was also replicated mechanochemically which also contained additional peaks in the ³¹P NMR.

Synthesis of As[N(SiMe₃)₂]₃ (2**).** AsI₃ (0.503 g, 1.10 mmol) was dissolved in toluene (70 mL). To this, a solution of K[N'] in toluene (0.661 g, 3.31 mmol) was added dropwise over the course of 5 min at room temperature. After 1.5 h of stirring, the yellow suspension was filtered over a medium porosity frit. All volatiles were removed from the yellow filtrate to afford **1** as a waxy yellow solid (0.507 g, 83%). Colorless X-ray quality crystals were obtained by slow evaporation of a hexane solution of **2**. Anal. Calcd (%) for C₁₈H₅₄AsN₃Si₆: C, 38.88; H, 9.79; As, 13.47; N, 7.56. Found: C, 38.64; H, 9.08; As, 13.4; N, 7.15. ¹H NMR (400 MHz, C₆H₆, 298 K): δ 0.36 (500 MHz, THF-d₈, 298 K): δ 0.36 (δ 0.35 at 230 K). ¹³C{¹H} NMR (100 MHz, C₆D₆, 298 K): δ 5.51.

General Procedures for X-ray Crystallography. A suitable crystal of each sample was located, attached to a glass fiber, and mounted on a Bruker diffractometer for data collection at 173(2) K or 100(2) K. Data collection and structure solutions for all molecules were conducted at the University of California, San Diego by Dr. Arnold L. Rheingold (P, As) or at the X-ray Crystallography Facility at the University of Rochester by Dr. William W. Brennessel (Sb). The intensity data were corrected for absorption and decay (SADABS). All

calculations were performed using the current SHELXTL suite of programs.¹¹⁰ Final cell constants were calculated from a set of strong reflections measured during the actual data collection. Relevant crystal and data collection parameters for each of the compounds are given in Table 6.

The space groups were determined based on systematic absences and intensity statistics. Compound **3** refined as a two-component twin, with a merohedral twin law of $[0 \ -1 \ 0 \ / \ -1 \ 0 \ 0 \ / \ 0 \ 0 \ -1]$. For all the compounds, a direct-methods solution was calculated that provided most of the non-hydrogen atoms from the E-map. Several full-matrix least squares/difference Fourier cycles were performed that located the remainder of the non-hydrogen atoms. Non-hydrogen atoms were refined with anisotropic displacement parameters. All hydrogen atoms were placed in ideal positions and refined as riding atoms with relative isotropic displacement parameters. In the case of **3**, there are two large peaks of electron density that remain in the final difference map. They are located 0.80 and 1.03 Å from atoms Si1 and Si2, respectively. They are separated by 2.97 Å, which is similar to the distance between Si1 and Si2 (3.02 Å). However, no methyl groups could be placed on these potential silicon atoms without violating the van der Waals space of neighboring symmetry equivalent methyl groups. Therefore, these peaks were left unassigned.

Note on crystal formation for 3. Compound **3** was initially isolated from hexanes solution as a yellow solid, but not in the form of crystallographically useful crystals. A sample of **3** that had been stored in a glovebox for more than a year was later found to contain crystals suitable for data collection. One-half of a molecule of HN' was found per molecule of **3** in the lattice. The HN' molecule was found to be disordered over a crystallographic $\bar{3}$ site,

and is well separated from **3** (Me...Me' contacts > 4.0 Å). Evidently during the long storage the compound was exposed to trace amounts of water that caused partial hydrolysis of the sample, which then aided crystallization. As a check on this, a mixture of freshly prepared Sb[N']₃ and HN' was allowed to slowly evaporate, and pale yellow plates formed within one week. The crystals were found to have the same unit cell as compound **3**.

Computational Details. Molecular mechanics calculations were performed with the UFF force field⁸⁹ as implemented in Gaussian 09.¹¹¹ In the case of Ce[CH(SiMe₃)₂]₃, charges were assigned to all atoms using the QEq method;¹¹² use of an alternative charge assignment method¹¹³ was required to achieve convergence with Sb[N']₃. Assigning charges did not improve the structure of Pu[N']₃ (e.g., the overpyramidalization was worse), and they were not included in the final optimization. The Solid-G program⁶³ was used to compute ligand solid angles. They are converted to percentages (G-values) that reflect the shielding by each ligand of the central metal.

Density functional calculations were performed both with the Gaussian 09W¹¹¹ and Amsterdam Density Functional (ADF)¹¹⁴ suite of programs. With Gaussian, the meta-GGA functional M06-L⁹⁶ was used; this provides an accounting for dispersion interactions. The effective core potential basis sets LANL08 were used for on all the metal centers when d functions were not desired; the corresponding LANL08(d) bases were used to incorporate additional polarization and diffuse functions.¹¹⁵ The split valence polarized basis sets def2SVP were used for all other atoms.¹¹⁶ With ADF, the functional BP86-D3(BJ) was used; it incorporates dispersion corrections according to Grimme's DFT-D3 method,¹¹⁷ and uses the Becke-Johnson damping function as well.¹¹⁸ Full geometry optimizations were carried out

with all-electron valence triple- ζ Slater-type basis sets with double-polarization functions for all atoms (TZ2P) from the ADF basis set library; ZORA scalar relativistic corrections were used for the Sb, Bi and Lu complexes. The AIM analysis and Mulliken population analysis were conducted with the functionality built into the ADF program.

(This work was adapted from Boyde, N. C., et al. *Inorg. Chem.* **2014**, 53, 9703).

CHAPTER 3

Preparation of substituted $P[N(SiMe_3)_2]_3$ complexes and nanoparticle applications

3.1 Introduction

The versatility of the $-N(SiMe_3)_2$ (N') ligand has afforded multiple opportunities for its use in metal amide complexes. Development of applications for the newly prepared group 15 tris(amido) complexes, particularly the phosphorus derivative, $P[N']_3$, was of interest, but the latter's overwhelming steric bulk provided a challenge to its use in synthesis. The phosphorus compound has a calculated cone angle of 241° , and has 92% of its coordination sphere occupied.¹¹⁹ The bulk surrounding the central phosphorus was initially thought to be severe enough to limit the reactivity of this compound. Attempts to coordinate gold in the motif of $Cl-Au-P[N(SiMe_3)_2]_3$ produced gold nanoparticles instead, which then stimulated an in-depth study of the general utility of this compound for nanoparticle formation.

A major goal within the field of nanomaterials is to generate high quality nanoparticles with uniform size and shape. This control is typically garnered through temperature control, and the selection of appropriate metal precursors and capping ligands. Although production of high quality nanoparticles is the primary goal, another stress has recently been placed on the production of nanoparticles through more environmentally conscious, "green," methods. One way to push towards green chemistry is to limit the use of harsh conditions such as high temperatures and reducing agents. Historically, it has been difficult to maintain control over the size and shape of particles without the use of such energetic conditions. Another method

to reduce the overall impact of nanoparticle production is to limit the solvent consumption. Typically syntheses require total solvent consumption on the order of liters/gram of particle produced.¹²⁰

Production of monodisperse nanoparticles typically result from the nucleation processes. The two primary nucleation mechanisms relevant to nanoparticle formation are Ostwald ripening and coalescence.¹²¹ Ostwald ripening occurs when the highly curved small particles dissolve and subsequently precipitate onto large particles. Coalescence is the combination of different size particles into one larger particle. These methods can be controlled through the use of specific temperatures, times, and quenching procedures. These processes have been widely used in the field and produce high quality nanoparticles.¹²²

An alternative method to producing nanoparticles is through the use of mechanochemistry.¹²³ Reports have shown that ball milling techniques can result in nanoparticle formation, with some control stemming from the choice of metal, stoichiometry, and milling conditions. Frišćić et al. have produced gold particles with a high degree of uniformity through use of long chain capping ligands (aliphatic amines) and high energy forces in a mixer mill.¹²⁴ This method of producing nanoparticles in the solid state is used much less frequently than solution methods, which could be the result of the high cost barrier of the required mixing apparatus.

While investigating the reactivity of $P[N']_3$, noble metal reduction and nanoparticle formation was found to be one potential application of this compound. The initial reactions did not have an additional capping agent suggesting that the $P[N']_3$ is acting both as a reductant and a capping ligand. Derivation of $P[N']_3$ to form $S=P[N']_3$ and $O=P[N']_3$ was

attempted to model the reactivity that can be obtained from traditional capping agents. This would model the difference observed between triphenylphosphate (TPP) and triphenylphosphate oxide (TPPO), trioctylphosphine (TOP) and triphenylphosphine oxide (TOPO), and related sulfur analogs. These compounds have similar uses but the derivatized compounds open the possibility of various applications for which the parent compound may not be well suited.

TOP and TOPO are both used in nanoparticle synthesis¹²⁵ as well as in various other applications. The choice of using the oxide or not is system- and target-dependent, but the availability of both compounds is an important asset for given reactions. TPP and TPPO are also commonly used reagents with various applications in both nanoparticle and conventional transition metal complex synthesis.¹²⁶⁻¹²⁹ TPP readily binds to many transition metals but is notable for its ability as a labile ligand, in the presence of palladium, to promote cross coupling reactions.¹³⁰ TPPO is also a common reagent with uses as a crystallization aid¹³¹ and coordinating ligand.¹³⁰

3.2 Results/discussion

3.2.1 Nanoparticle formation

Metal nanoparticles were produced for gold, silver, and platinum through mechanochemical and solution methods. The gold particles displayed below show a wide range of sizes produced by the different methods.

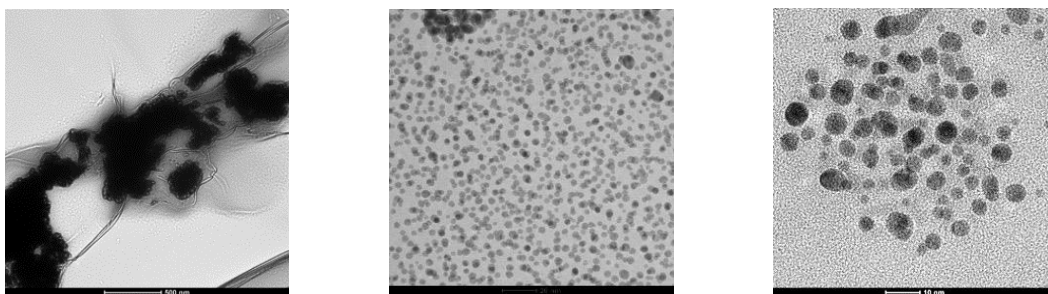


Figure 10. Gold nanoparticles formed from H₂AuCl₄

From left to right: H₂AuCl₄ ground without additional reagents, H₂AuCl₄ ground with P[N(SiMe₃)₂]₃, H₂AuCl₄ solution reaction with P[N(SiMe₃)₂]₃ from THF.

The formation of gold nanoparticles in the absence of additional reagents indicates that mechanochemical reduction is the primary driving force. Without any capping agent present, gold particles agglomerated into large groups of particles. In the presence of P[N(SiMe₃)₂]₃, the particles showed much higher uniformity. The average sizes are displayed in Table 6. The phosphorus-capped gold particles produced with milling are less uniform in size than might be desirable (23–33% variation), but the consistency and reproducibility of this method was not high.

Table 6. Nanoparticle size distribution from noble metal sources

Particle Source	Size Distribution
H ₂ AuCl ₄	Agglomerated
H ₂ AuCl ₄ + P[N(SiMe ₃) ₂] ₃ (Mill)	3.9 ± 0.9 nm
H ₂ AuCl ₄ + P[N(SiMe ₃) ₂] ₃ THF	4.5 ± 1.5 nm
PtCl ₂	1.9 ± 0.4 nm
PtCl ₂ + P[N(SiMe ₃) ₂] ₃ (Mill)	2.5 ± 0.5 nm
PtCl ₂ + P[N(SiMe ₃) ₂] ₃ THF	2.3 ± 0.4 nm
AgCF ₃ SO ₃	8 ± 5 nm
AgCF ₃ SO ₃ + P[N(SiMe ₃) ₂] ₃ (Mill)	3.8 ± 0.8 nm
AgCF ₃ SO ₃ + P[N(SiMe ₃) ₂] ₃ (tol)	9 ± 3 nm

The platinum particles were formed easily upon grinding, and did not simply agglomerate, as was observed for gold. The small average size of the platinum particles in the

absence of $P[N']_3$ could result simply from a size reduction of grinding; it should however be noted that while the majority of particles were very small, samples also contained much larger particles (30 nm). The oxidation state of particles was not checked at the time of TEM imaging but substantial chlorine was present on the EDS mapping. With the presence of $P[N']_3$ the particles were larger on average, but the method of either grinding or solvent reactions did not have a significant impact on the sizes. The images of platinum particles can be seen below Figure 11.

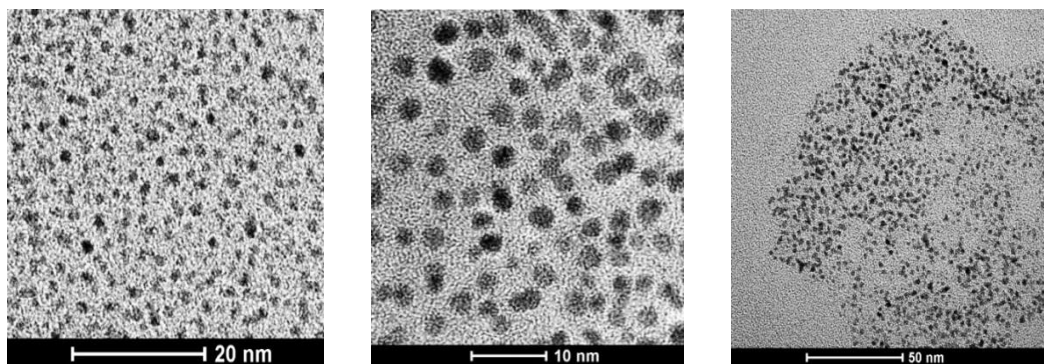


Figure 11. Platinum particles formed from $PtCl_2$

From left to right: $PtCl_2$ grind, $PtCl_2$ grind with $P[N(SiMe_3)_2]_3$, $PtCl_2$ with $P[N(SiMe_3)_2]_3$ in toluene.

The silver particles in the absence of $P[N']_3$ showed a large size distribution (>60%); the average size in the ground mixture containing $P[N']_3$ had a smaller average size and smaller deviation (ca. 20%), but the particles were still not uniform. The toluene reaction produced an average particle size similar to that of from those formed in the absence of $P[N']_3$, although the size distribution was almost twice as narrow.

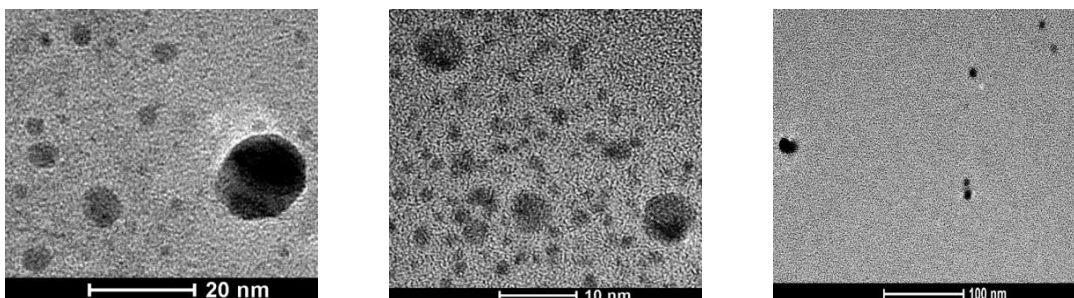


Figure 12. Silver particles formed from AgOtf

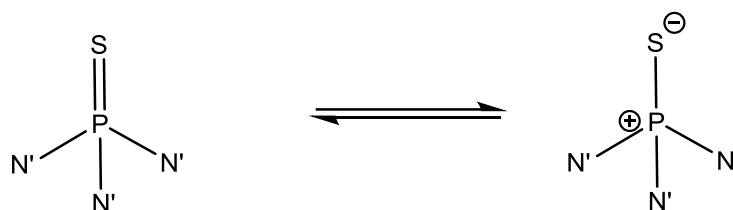
From left to right: AgOtf grind, AgOtf with $P[N(SiMe_3)_2]_3$ from grinding, AgOtf with $P[N(SiMe_3)_2]_3$ in toluene.

Due to the overall inconsistency with the shape and size of particles formed with $P[N']_3$, a replacement for it was sought. The preparation of $S=P[N']_3$ and $O=P[N']_3$ were attempted in order to produce bulky sulfur- and oxygen-donor ligands that would be more persistent capping agents.

3.2.2 Derivatives of $P[N(SiMe_3)_2]_3$

Halide metathesis of $SPCl_3$ with $K[N']$ was the reaction method of choice, which has literature precedent with less bulky amides.¹³² The results of this method are far from conclusive, as the ^{31}P NMR spectra shows a large number of peaks that have not yet been identified (see Appendix 3 for representative spectra). The 1H and ^{13}C spectra also displayed more peaks than were expected and did not clarify the situation clarity, thus the ^{31}P NMR spectra will be discussed in further detail. In an attempt to gain additional insight into the complex spectra, the reaction was performed at various temperature and ratios. The reaction was performed at room temperature, $0\text{ }^\circ\text{C}$ and $-78\text{ }^\circ\text{C}$, and in 1:1 and 2:1 ratios ($K[N']:SPCl_3$) at $-78\text{ }^\circ\text{C}$. The resulting product of these reactions was an oil that did not yield crystalline material.

There is a wide range of possible side products for this reaction, some of which will be discussed, but these are possibilities that have not been confirmed at this point. It has been reported that S-P bonds show a larger charge separation than respective O-P bonds.¹³³ This charge separation could lead to an equilibrium of S^-P^+ which could then allow for product formation involving a P-S-X bond where X could be another sulfur to form a disulfide compound. Other possibilities for the reaction include THF coordination, potassium ion interference, or the formation of bridged amido complexes.



Other possible side products involve the incomplete substitution reaction of the $SPCl_3$ and 3 $K[N']$, so as to form $S=PCl_2[N']$ or $S=PCl[N']_2$. Attempts to identify these side products were carried out by running the halide metathesis reaction in 1:1 and 2:1 ratios ($K[N']:SPCl_3$) as previously mentioned. These tests were inconclusive, as a variety of peaks were still present in the ^{31}P spectra.

The ^{31}P NMR spectra were run both in both proton coupled and decoupled modes, and which always contained a large number of peaks. Some of these peaks were different in the coupled and decoupled spectra, meaning there is evidently a side-product with a reasonable J_{PH} coupling. $^4J_{PH}$ coupling is rarely seen unless the compound adopts a W-conformation (in a phenomenon known as the ‘W effect’).¹³³ This effect is a through-space interaction that occurs when the proton is close enough to directly interact with the phosphorus. In normal $P[N']_3$, there is no change between the coupled and decoupled spectra, so the parent does not

display the $^4J_{\text{PH}}$ coupling. This implies a side-product that whose composition is not intuitively obvious.

The 3 K[N']₃:1 OPCl₃ reaction yielded a solid with two notable peaks and one smaller peak in the ³¹P NMR (Spectra shown in Appendix 3). The two primary peaks had similar intensity and an apparent “splitting” of 1119 Hz, which is a reasonable coupling constant for ³¹P NMR; however, further experiments showed that this is likely not a doublet. The reaction of K[N'] and OPCl₃ was run at a 2:1 and 1:1 ratio to determine if the peaks found in the 3:1 reaction could be easily identified as an incomplete substitution product. The shifts of the peaks and their respective integration can be seen in Table 2.

Table 7. Ratio of major peaks in ³¹P NMR for the reaction 3K[N(SiMe₃)₂]₃ + OPCl₃

Ratio	Chemical shift (ppm)		
3:1	-11.06 ppm 100.0 relative intensity	-17.97 83.04	-19.70 11.65
2:1	-11.08 0.78	-17.99 100.0	-19.70 4.078
1:1	-11.08 1.13	-17.98 100.0	-19.68 13.49

The peaks listed in Table 7 reflect the only peaks present for the 3:1 reaction, but it should be noted additional peaks are apparent in the 2:1 and 1:1 that are not listed. This test showed that the peaks at -11 ppm and -18 ppm do not comprise a doublet, as the ratio of peaks shifts drastically and they likely represent a major side-product. This side-product has not yet been identified. It should be noted that there were also differences in the proton and carbon spectra of the 3:1, 2:1, and 1:1 reactions. In addition, when the 3:1 reaction ratio is replicated under the same conditions (time, temperature, and scale), the number of peaks and their integrated intensity are not the same.

Calculations on these compounds were performed to study the bond lengths of the E=P bond, and the charges related to the E and P (E = O, S) moieties. Charges were calculated using NBO population analysis with Gaussian 09. The charges are reported below and show that, as expected, the oxygen has a greater negative charge than the sulfur. This implies a stronger O-P than S-P bond. The weaker interaction of sulfur to phosphorus shown in these calculations supports the supposition that the greater number of side-products formed by the sulfur compound may result from a weaker S-P bond.

	Charge on E	Charge on P	Average Charge N
S=P[N(SiMe ₃) ₂] ₃	-0.613	2.045	-1.69
O=P[N(SiMe ₃) ₂] ₃	-1.155	2.534	-1.68

3.3 Conclusion

Nanoparticles can be formed through mechanochemical processing of silver or noble metal salts, but the particle morphology is not well controlled. The routes do not appear at this time to produce high quality particles, and conditions would need to be greatly optimized for them to be of practical utility. In the case of the solution and mechanochemical approach to gold nanoparticles, it is clear that not all of the gold reacts, which is apparent from the yellow gold chloride-containing filtrates that are left. The synthesis of platinum particles showed the highest level of size and shape control, but this synthesis was not fully optimized. It is possible through further optimization of synthesis and work-up procedures these particles could be produced in a high enough quality for further applications.

Although halide metathesis has been used a method to produce other S=PNR₃ complexes, it would appear as though this is not a viable method to produce S=P[N']₃ and

O=P[N']₃. The preliminary results from this study show a product that contains a variety of non-reproducible side products that have not yet been identified.

A possible explanation for this involves the large amount of steric bulk in the tris(amide) compound. Previous studies on the parent P[N']₃ compound showed a calculated cone angle of 241°; a Solid-G calculation suggested that 92% of the coordination sphere was occupied, and the space-filling model indicates a buried phosphorus. Despite these bulky attributes, reactivity has been observed with the P[N']₃ parent compound.

3.4 Future directions of this project

To generate optimally sized particles, extensive screenings would be needed to test the particles under different times of reaction, different solvents (when used), and possibly varied temperatures. Typical nanoparticle and quantum dot syntheses use high temperatures to control the nucleation of particles, and thus they have a greater control over the sizes. The goal of this project was to produce particles under mild conditions, but this resulted in particles of low quality. More traditional reducing agents could be tested, and P[N']₃ could be screened as just a capping agent for various particles, rather than attempt to exploit its reducing abilities as well.

This system has proven to be complicated and the identification of the side products has not been successful. Attempts could be made to produce these products in higher yield or to develop an approachable method of separation, but at this time the project is being curtailed due to the possibility that the product mixtures will be intractable. If this project is revisited in the future, attempts could be made to identify and separate the products. Halide metathesis has been shown to not be a viable route for this method, and mechanochemical approaches

would not be feasible since OPCl_3 and SPCl_3 are liquids; in addition, the reaction is likely to be strongly exothermic, which would be difficult to manage under mechanochemical conditions. Routes to directly sulfonate or oxygenate the $\text{P}[\text{N}']_3$ would theoretically be possible, but these are not being investigated at this time.

3.5 Experimental

General Considerations:

All manipulations were performed with the exclusion of air and moisture using high vacuum, Schlenk, or glovebox techniques. Proton, carbon ($^{13}\text{C}\{^1\text{H}\}$), and phosphorus ($^{31}\text{P}\{^1\text{H}\}$) (^{31}P) NMR spectra were obtained on a Bruker DRX-500 or DRX-400 spectrometer at 500 or 400 (^1H), 100.1 (^{13}C) 169.9 (^{31}P) MHz, and were referenced to the residual proton and ^{13}C resonances of C_6D_6 or THF- d_8 . Typical grinding conditions involve loading the grinding jar with solid samples (typically 500 mg or less), 6 mm stainless steel ball bearings (50 count), and sealing under inert atmosphere. The reaction then was then ground for 15 minutes at 600 RPM using a PM100 planetary ball mill.

The general procedure for the solution based reactions was to dissolve the metal salt in THF and add a solution of $\text{P}[\text{N}(\text{SiMe}_3)_2]_3$ in THF to the metal. This reaction was filtered and the filtrate was collected; the THF was removed through vacuum filtration and any remaining solid was collected and analyzed.

Synthesis of gold nanoparticles

Solvent reaction: HAuCl_4 was dried under vacuum to remove ambient water in the system. The HAuCl_4 (1 equiv) was then dissolved in THF to produce a yellow solution. To

this solution, a separate solution of P[N']₃ (1 equiv) in THF was added. The solution rapidly turned from yellow to brown/black. The reaction was allowed to stir for 2 h, then the solution was filtered to afford a yellow filtrate and a brown precipitate, which dried to a purple solid. The volume of the yellow filtrate was reduced, and the precipitate was collected and subsequently analyzed. The precipitate was analyzed with UV-vis spectroscopy and TEM analysis.

Solid state reaction: Equimolar amounts of H₂AuCl₄ and P[N']₃ solids were added to a grinding jar. These were allowed to grind together for 15 min at 600 RPM, which afforded a brown solid. After suspending the solid in THF and filtering, the solid became purple on drying; as in the case with the solution synthesis, the filtrate was yellow. The resulting particles were also analyzed with UV-Vis and TEM.

Synthesis of platinum nanoparticles

Solvent reaction: PtCl₂ (1 equiv) was dissolved in THF to produce a brown solution. To this solution, a separate solution of P[N']₃ (1 equiv) in THF was added. The solution did not immediately change color but darkened over the course of the reaction. The reaction was allowed to stir for 2 h. The brown solution was filtered to afford a colorless filtrate and a brown/black precipitate. The precipitate was analyzed with TEM methods.

Solid state reaction: Equimolar amounts of solid PtCl₂ and P[N']₃ were added to a grinding jar. These were allowed to grind together for 15 min at 600 RPM, which afforded a brown solid. After suspending the solid in THF and filtering, the solid became purple on drying; as in the case with the solution synthesis, the filtrate was yellow. The resulting particles were also analyzed with TEM.

Synthesis of silver nanoparticles

Solvent reaction: AgOTf (1 equiv) was dissolved in THF to produce a brown solution. To this solution, a separate solution of P[N']₃ (1 equiv) in THF was added. The solution did not immediately change color but darkened over the course of the reaction. The reaction was allowed to stir for 2 h. The brown solution was filtered to afford a colorless filtrate and a brown/black precipitate. The precipitate was analyzed with TEM methods.

Solid state reaction: Equimolar amounts of AgOTf and P[N']₃ solids were added to a grinding jar. These were allowed to grind together for 15 min at 600 RPM, which afforded a brown solid. After suspending the solid in THF and filtering, the solid became purple on drying; as in the case with the solution synthesis, the filtrate was yellow. The resulting particles were also analyzed with TEM.

Attempted preparation of S=P[N(SiMe₃)₂]₃

A solution of K[N'] (1, 2, or 3 equiv) was prepared in 50 mL of THF and was cooled to -78 °C in a dry ice/acetone bath. To this solution, SPCl₃ (1 equiv), which was previously cooled in ice water, was injected. This mixture was allowed to stir for 16 h while slowly warming to room temperature. The THF was removed by vacuum and the remaining product was dissolved in hexane and filtered through a medium porosity glass frit. The hexane was then removed through vacuum until dry, and the product was then analyzed with NMR spectroscopy.

Attempted preparation of $\text{O}=\text{P}[\text{N}(\text{SiMe}_3)_2]_3$

A solution of $\text{K}[\text{N}']$ (1, 2, or 3 equiv) was dissolved in 50 mL of THF and was cooled to $-78\text{ }^\circ\text{C}$ in a dry ice/acetone bath. To this solution, OPCl_3 (1 equiv), which was previously cooled in ice water, was injected. This mixture was allowed to stir for 16 h while slowly warming to room temperature. The THF was removed by vacuum and the remaining product was dissolved in hexane and filtered through a medium porosity glass frit. The hexane was then removed through vacuum until dry, and the product was then analyzed with NMR spectroscopy.

CHAPTER 4

Reaction environment and ligand lability in group 4 Cp₂MX₂

(X,Y = Cl, OtBu) complexes

4.1 Introduction

As one of the fundamental methods of organometallic synthesis, salt metathesis ($RM + M'X \rightarrow RM' + MX$; M = typically group 1 or 2 metal) is broadly employed in both main-group and transition metal chemistry.¹³⁴ The outcome of the reaction depends on many factors, including solvent polarity, the electropositivity of the metals, and if isolated by crystallization, the solubility of the intended product. In some cases, kinetically and/or thermodynamically favored products are obtained regardless of the reaction stoichiometry.¹³⁵⁻¹³⁶ In addition, mechanochemical synthesis, which employs mechanical forces to promote the breaking and formation of chemical bonds, has the potential to direct salt metathesis in ways different from those typically found in solution-based routes.¹³⁷⁻¹³⁸ We report here the influence of solvent polarity and mechanochemical activation in the formation of group 4 metal Cp_xMCl_y(OtBu)_{4-(x+y)} complexes, whose formation via halide metathesis is unusually dependent on reaction environment.

The Cp[∗]/OR complexes of the group 4 metals, Cp[∗]_{2-x}M(OR)_{2+x}, are of interest for their ability to serve as initiators of syndiotactic polymerization of styrene (M = Ti);¹³⁹ in combination with MAO, they are highly active initiators of α-olefin polymerization.¹⁴⁰⁻¹⁴¹ Both chiral¹⁴² and non-chiral¹⁴³⁻¹⁴⁴ versions of the complexes have been investigated in the polymerization of lactide monomers and ε-caprolactone.¹⁴² For M = Zr and Hf, the Cp[∗]₂M(OR)₂ species are effective CVD precursors of thin-film zirconia and hafnia.^{12, 145}

Despite their applications in catalytic and materials chemistry, there are few reliable synthetic routes available for the $\text{Cp}'_2\text{M}(\text{OR})_2$ complexes. Typical approaches start either from a cyclopentadienyl precursor or a metal tetraalkoxide, but they do not always yield stoichiometrically precise results. In the case with $\text{OR} = \text{OtBu}$, for example, the formation of $\text{Cp}_2\text{Ti}(\text{OtBu})_2$ has been reported from the reaction of $\text{Li}[\text{OtBu}]$ and Cp_2TiCl_2 in THF,¹⁴⁶ although as described below, $\text{Cp}_2\text{Ti}(\text{OtBu})_2$ is only one of several products generated by this route. The Zr analogue has been prepared similarly ($\text{Cp}_2\text{ZrCl}_2 + (\text{Li or Na})[\text{OtBu}]$),¹⁴⁷ but this yields an inseparable mixture of $\text{Cp}_2\text{ZrCl}(\text{OtBu})$ and $\text{Cp}_2\text{Zr}(\text{OtBu})_2$, even with the use of more than 2 equiv of the alkoxide.¹² A cleaner route to $\text{Cp}_2\text{Zr}(\text{OtBu})_2$, but with unspecified yield, has been reported through alcoholysis ($\text{Cp}_2\text{ZrCl}_2 + \text{excess HOtBu/Et}_3\text{N}$).¹² In contrast, more predictable synthesis exist for mono(cyclopentadienyl) complexes; $\text{CpTi}(\text{OtBu})_3$ is produced from the reaction of CpTiCl_3 with HOtBu ,¹⁴⁸ for example, and for all three metals, the metathetical exchange between $\text{M}(\text{OtBu})_4$ and Cp_2Mg in benzene produces the $\text{CpM}(\text{OtBu})_3$ complexes.¹⁴⁰ Notably, however, salt metathesis is not used as a standard route to the mono-Cp compounds.

4.2 Results and discussion

Titanium complexes. In what was intended to be a straightforward reproduction of the preparation of $\text{Cp}_2\text{Ti}(\text{OtBu})_2$,¹⁴⁶ the reaction of Cp_2TiCl_2 (TDC) with $\text{Li}[\text{OtBu}]$ in THF was conducted at the specified concentrations of 0.5 and 1.0 M, respectively. It yielded $\text{Cp}_2\text{Ti}(\text{OtBu})_2$ (δ 5.98 (Cp); 1.16 (OtBu)) as the major product (61%), but there were also substantial amounts (26%) of the mono(cyclopentadienyl) species $\text{CpTi}(\text{OtBu})_3$ (δ 6.24 (Cp); 1.26 (OtBu)),¹⁴⁸⁻¹⁴⁹ and a smaller but easily detectable (13%) amount of the tetraalkoxide,

Ti(OtBu)₄ (δ 1.36) (Table 8, #1). This result is at variance with the literature report,¹⁴⁶ for which Cp₂Ti(OtBu)₂ was the only stated product (obtained in >90% purity); apart from possible instrumental limitations (e.g., the use of 90 MHz ¹H NMR), we are unsure of the reason for this discrepancy. As part of the investigation into Cp₂Ti(OtBu)₂ formation, other reactions were conducted with K[OtBu], to remove potential complications from the solvated Li⁺ ion.¹⁵⁰ With a K[OtBu]:TDC ratio of 2:1 in THF (#2), the product distribution again contained the three previously observed alkoxide species (although Ti(OtBu)₄ is in trace amounts), but there was also evidence for a new, previously unreported species, Cp₃Ti(OtBu) (**1**) (δ 5.74, $w_{1/2}$ = 22 Hz (Cp); δ 1.01 (OtBu)). When the amount of K[OtBu] relative to TDC was increased to 4:1, Cp₂Ti(OtBu)₂ and Cp₃Ti(OtBu) were no longer among the observable compounds (#3); only CpTi(OtBu)₃ and Ti(OtBu)₄ were detected.

Table 8. Summary of Cp₂MX₂ and M'[OtBu] reactions

No.	Cp ₂ MCl ₂	M'[OtBu]	Medium	Cp ₂ MCl(OtBu)	Cp ₂ M(OtBu) ₂	CpTi(OtBu) ₃	Ti(OtBu) ₄	Cp ₃ Ti(OtBu) (1)
1	M = Ti	2, M = Li	THF		0.61	0.26	0.13	
2	M = Ti	2, M = K	THF		0.70	0.13	0.02	0.15
3	M = Ti	4, M = K	THF			0.60	0.40	
4	M = Ti	2, M = K	hexanes		0.37	0.40	0.02	0.21
5	M = Ti	3, M = K	hexanes			0.93	0.07	
6	M = Ti	2, M = K			0.32	0.47	0.18	0.03
7	M = Ti	3 or 4, M = K				0.88	0.12	
8	M = Zr	2, M = K		0.81	0.19			
9	M = Zr	3 or 4, M = K			1.00			
10	M = Hf	1, M = K	hexanes	1.00				
11	M = Hf	1, M = K		1.00				
12	M = Hf	2, M = K	hexanes	0.14	0.86			
13	M = Hf	2, M = K		0.59	0.41			
14	M = Hf	3 or 4, M = K			1.00			

^a = ball milling at 600 rpm for 15 min. The symbol for mechanical milling has been proposed in ref. 3a.

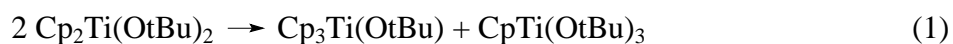
Solution reactions were run for 18 hr.

To determine whether such extensive ring/alkoxide scrambling was a consequence of using THF, the solvent was changed to a nonpolar alkane. In hexanes, an 18 hr reaction of K[OtBu]:TDC in a 2:1 ratio generated Cp₂Ti(OtBu)₂ and CpTi(OtBu)₃ in nearly equal amounts; only traces ($\leq 2\%$) of Ti(OtBu)₄ were detectable in NMR spectra (#4). The amount of **1** was somewhat greater than that found from the reaction in THF, and it could be crystallized from the reaction mixture. It should be noted that the reaction of the unmilled reagents in hexanes is slow; the red solution of TDC and the accompanying slurry of K[OtBu] displayed no immediate color change, and workup of a reaction after 1 hr revealed that over half (57%) of the TDC remained unreacted; there was no evidence at this point for formation of **1**. At higher ratios of K[OtBu]:TDC in hexanes, the reaction outcomes were similar to

those found in THF; i.e., CpTi(OtBu)₃ and Ti(OtBu)₄ are the only observed complexes, although CpTi(OtBu)₃ is by far the major product (93%, with a 3:1 K[OtBu]:TDC ratio) (#5).

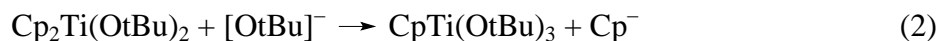
In order to remove the influence of solvent entirely, a mixture of white K[OtBu] and red Cp₂TiCl₂ (TDC) was ground in a ball mill in a 2:1 ratio (600 rpm, 15 min); the resulting orange powder was extracted with hexanes, filtered and evaporated to dryness (#6). Once again, all four alkoxide products were formed, but Cp₂Ti(OtBu)₂ constituted only about a third of the total product. CpTi(OtBu)₃ comprised almost half; Ti(OtBu)₄ represented 18% of the product, and **1** was present in near trace amounts (3%). When the amount of K[OtBu] relative to TDC was increased to 3:1, Cp₂Ti(OtBu)₂ and **1** were no longer among the observable compounds (#7); the amount of CpTi(OtBu)₃ (88%) is closer to that of the reaction in hexanes (93%) than to that in THF (60%). A further increase in the K[OtBu]:TDC ratio to 4:1 did not change the product distribution. The reactions by ball milling occur much more quickly than those in solution; after 15 min of milling, no TDC is observed among the products; this behavior distinguishes the hexanes reactions from the ball milled cases, even though hexanes are used during extraction of the latter.¹⁵¹

The formation of **1** is of special note, as it has not previously been reported as a member of the Cp_xTi(OtBu)_{4-x} family. This product is only observed from 2:1 K[OtBu]:TDC reaction mixtures, but is produced both in solution (THF, hexanes) and ball milling reactions. The absence of **1** at higher ratios (≥ 3:1) of K[OtBu]:TDC could be the result of its formation being the result of cyclopentadienyl/alkoxide scrambling such as that in eq. 1.



Specifically, if **1** is formed rapidly under elevated alkoxide concentrations directly from $\text{Cp}_2\text{Ti}(\text{OtBu})_2$, and if the reaction in eq. 1 is relatively slow, little of the bis(alkoxide) complex will be available to generate **1** through redistribution.

An alternative, perhaps sterically preferable route to **1** could be through the action of a $\text{Cp}_2\text{TiCl}(\text{OtBu})$ intermediate. Although it was not observed under the reaction conditions used here, the monochloro complex is certainly a likely species (it would form from the reaction of one equivalent of $\text{K}[\text{OtBu}]$ with TDC). Once $\text{Cp}_2\text{Ti}(\text{OtBu})_2$ reacts with $[\text{OtBu}]^-$ to release Cp^- (eq 2), the latter could add to $\text{Cp}_2\text{TiCl}(\text{OtBu})$ to form **1** (eq. 3).¹⁵²



Both of these possibilities (which are not mutually exclusive) are discussed further below.

Zirconium and hafnium complexes. With Zr and Hf, less ligand scrambling occurs during the formation of cyclopentadienyl alkoxide complexes. An equiv of $\text{Li}[\text{OtBu}]$ is reported to react with Cp_2ZrCl_2 in THF to form only $\text{Cp}_2\text{ZrCl}(\text{OtBu})$.¹² The use of 2 equiv (or more) of the alkoxide in THF, however, generates an inseparable mixture of $\text{Cp}_2\text{ZrCl}(\text{OtBu})$ and $\text{Cp}_2\text{Zr}(\text{OtBu})_2$ (**2**). We find that the use of diethyl ether produces **2** in a cleaner form from a 2:1 ratio of $\text{K}[\text{OtBu}] : \text{Cp}_2\text{ZrCl}_2$, and that material can be sublimed under vacuum for additional purification (see Experimental section). As in THF, ball milling $\text{K}[\text{OtBu}]$ and Cp_2ZrCl_2 in a 2:1 ratio also produces a $\text{Cp}_2\text{ZrCl}(\text{OtBu}) : \mathbf{2}$ mixture, in a 0.81:0.19 ratio (#8). Increasing the $\text{K}[\text{OtBu}] : \text{Cp}_2\text{ZrCl}_2$ ratio to 3:1 or 4:1, however, yields only **2** (#9). Interestingly, there is no evidence for ring displacement, i.e., no $\text{CpZr}(\text{OtBu})_3$ or $\text{Zr}(\text{OtBu})_4$ formation, as was observed in the titanium chemistry.

Reactions with the hafnium system follow a similar pattern. The reaction of K[OtBu] and Cp₂HfCl₂ in a 1:1 ratio in hexanes produces exclusively Cp₂HfCl(OtBu) (**3**) (#10). When the same mixture is again milled without solvent (#11), **3** is again the only product. Interestingly, when repeated with THF, the reaction does not proceed detectably within 18 hr, and only starting materials are recovered.

Allowing K[OtBu] and Cp₂HfCl₂ to react in hexanes in a 2:1 ratio produces a **3** : Cp₂Hf(OtBu)₂ (**4**) mixture in a 0.14:0.86 ratio (#12), but grinding the same ratio still leaves **3** as the majority product (#13). Only **4** is found when the K[OtBu] : Cp₂HfCl₂ ratios are boosted to 3:1 or 4:1 under ball milling conditions (#14).

Structures. Crystals of **1** were grown from hexanes, and its structure was determined with X-ray crystallography (Figure 13). A distorted tetrahedral environment around the titanium center is defined by the centroids of two η⁵-Cp rings, one η¹-Cp ring, and the oxygen atom of the (OtBu) group. This is the arrangement predicted for a Cp₃TiX species in order to avoid an excessively electron-rich 20 e⁻ environment.¹⁵³⁻¹⁵⁴ The Ti-ring centroid distance of 2.11 Å (ave) is slightly longer than the 2.06 Å found in Cp₂TiCl₂, possibly the result of steric crowding.¹⁵⁵ There are few structurally authenticated Ti-(η¹-Cp) bonds that can be compared to that in **1**, but its length (2.304(1) Å) is shorter than the 2.366(4) Å found in the sterically comparable (η⁵-Cp)₂(η¹-Cp)Ti(N=P(tBu)₃),¹⁵⁶ presumably because of the electron richness of the latter. The Ti-O distance is slightly shorter than normal, but is similar to the 1.792(3) Å length in Cp₂Ti(OtBu)C(Ph)=CH(Ph).¹⁵⁷ The Ti-O-C angle is very wide (ca. 171°), which is consistent with partial multiple bonding, electrostatic repulsion¹⁵⁸ or steric crowding¹⁵⁹ involving the Ti-O interaction.

Neither $\text{Cp}_2\text{HfCl}(\text{OtBu})$ nor $\text{Cp}_2\text{Hf}(\text{OtBu})_2$ has been previously described, nor has the crystal structure of $\text{Cp}_2\text{Zr}(\text{OtBu})_2$ (**2**) been reported, and hence the crystal structures of **2–4** were obtained. The zirconium and hafnium $\text{Cp}_2\text{M}(\text{OtBu})_2$ molecules are isostructural, and crystallize as monomers with the metals coordinated by two η^5 -Cp rings and two terminal OtBu ligands in a distorted tetrahedral environment. The Cp ligands and OtBu groups are disordered over crystallographic mirror planes (50:50). A drawing of **2** is provided in Figure 14; a depiction of the hafnium analogue **4** is in the ESI.†

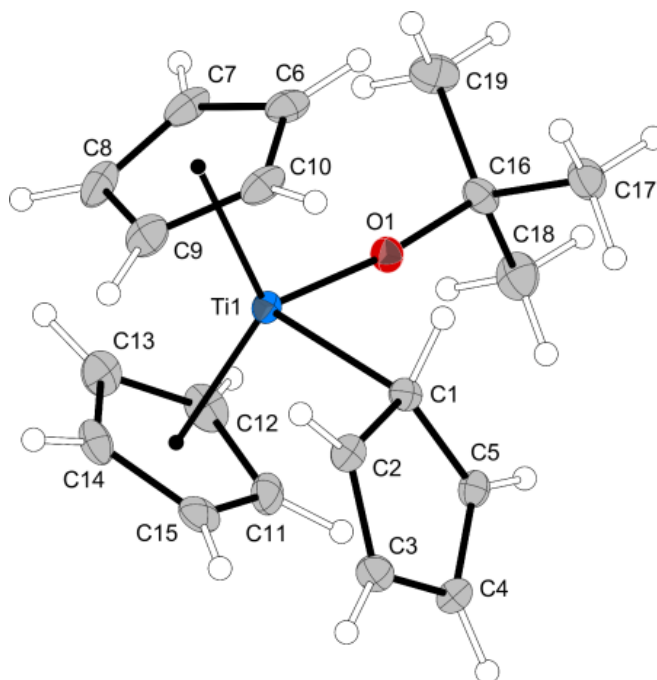


Figure 13. Thermal ellipsoid of $\text{Cp}_3\text{Ti}(\text{OtBu})$

Thermal ellipsoid plot of **1** (50% level); hydrogens are drawn with arbitrary radii. Selected bond distances (Å) and angles (deg): Ti1–O, 1.794(1); O1–C16, 1.416(2); Ti1–Cp1 (ring centroid/C6–C10), 2.115; Ti1–Cp2 (ring centroid/C11–C15), 2.108; Ti1–C1, 2.304(1); O1–Ti1–C1, 90.06(5); Ti1–O1–C16, 170.88(9); Cp1–Ti1–Cp2, 129.2.

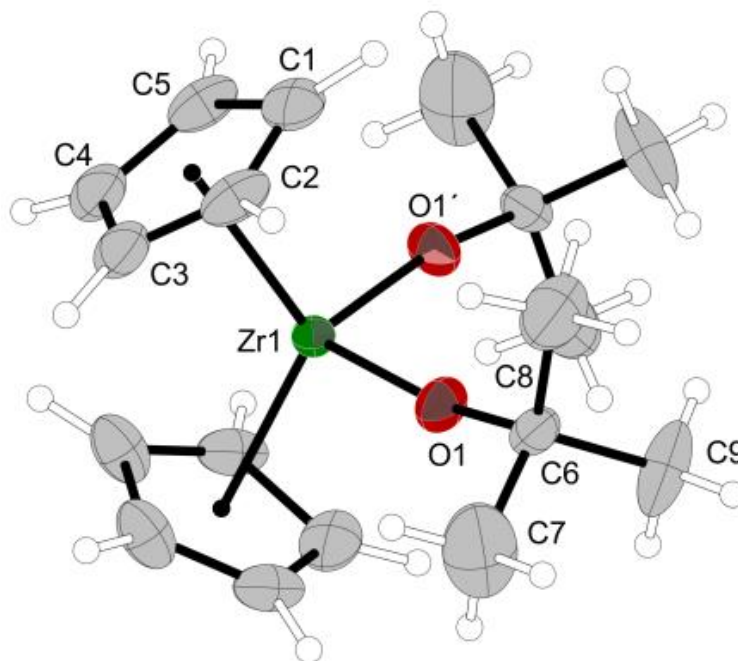


Figure 14. Thermal ellipsoid plot of $\text{Cp}_2\text{Zr}(\text{OtBu})_2$

Thermal ellipsoid plot of **2** (40% level); hydrogens are drawn with arbitrary radii. Selected bond distances (Å) and angles (deg) for **2** (listed first) and for **4**: M–O, 1.925(2), 1.915(7); O1–C6, 1.421(4), 1.441(13); M–Cp′(ring centroid), 2.274, 2.252; O1–M–O1′, 99.3(5), 100.1(1); M–O1–C6, 169.7(1), 166.6(4); Cp′–M–Cp′, 123.3, 123.5.

Despite the bulk of the $-\text{OCMe}_3$ groups, the Zr–O distance of 1.925(2) Å is slightly shorter than in related molecules (cf. 1.973(3) Å in $\text{Cp}_2\text{Zr}(\text{OCHPh}_2)_2$,²⁴ 2.01(1) Å in $\text{Cp}_2\text{Zr}(\text{OPh})_2$ ²⁵). This is accompanied by a wide Zr–O–C angle (169.7(1)°) (cf. 144.2(2)° and 153.7(2)° in $\text{Cp}_2\text{Zr}(\text{OCHPh}_2)_2$,¹⁶⁰ 147.1(1)° in $\text{Cp}_2\text{Zr}(\text{OPh})_2$ ^{159, 161}).

The hafnium complex **3** is isostructural with its zirconium analogue.¹² Both are monomers with the metals coordinated by two η^5 -Cp rings, a chloride and a terminal OtBu ligand in a distorted tetrahedral manner (Figure 15). The Hf–O distance is 0.022 Å longer than in the Zr complex, in line with the small difference in covalent radii between the two metals.⁵³ The only other structurally authenticated complex that offers a direct comparison with **3** is $\text{Cp}_2\text{HfCl}(\text{O-2-methyladamantoxy})$; notwithstanding the bulk of the substituted adamantoxy

group, the Hf–O distance of 1.900(2) Å is slightly shorter than in **3**, but the Hf–O–C angles are within 1.0° of each other.¹⁴¹ As with the related molecules **1**, **2**, and **4**, the wide angles (>170°) are consistent with the existence of d_{π} – p_{π} interactions.

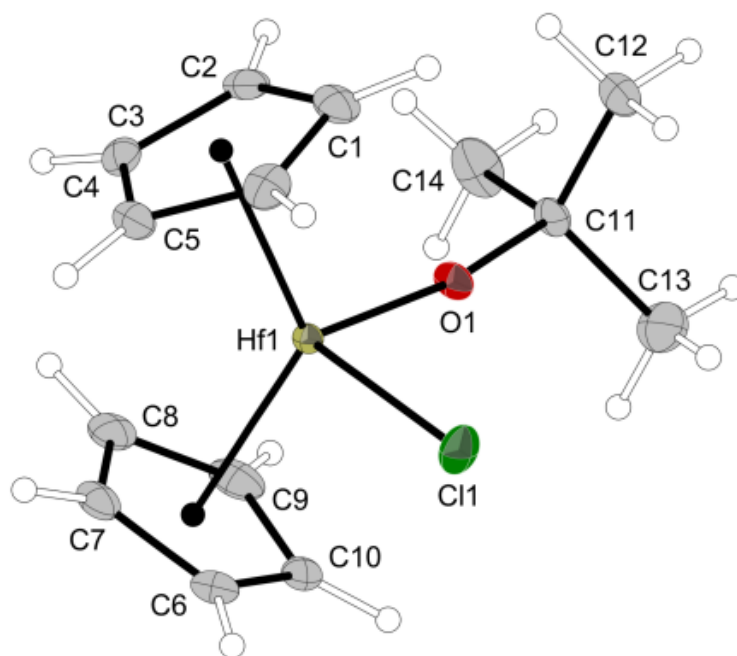


Figure 15. Thermal ellipsoid plot of Cp₂HfCl(OtBu)

Thermal ellipsoid plot of **3** (50% level); hydrogens have arbitrary radii. Selected bond distances (Å) and angles (deg): Hf1–O1, 1.917(2); Hf1–C11 = 2.4633(8); O1–C11, 1.423(4); M–Cp'(ring centroid), 2.085 (ave); O1–Hf1–C11, 96.53(7); Hf1–O1–C11, 171.1(2); Cp'–M–Cp', 130.6.

Calculation results. DFT calculations of the relative energies of some of the transformations observed here were completed with the M06 functional;^{116, 162} in addition, reaction energies were also studied in THF with a solvation model (PCM).¹⁶³ All the conformations were found to be minima on their respective potential energy surfaces. A summary of energy changes is given in Figure 16.

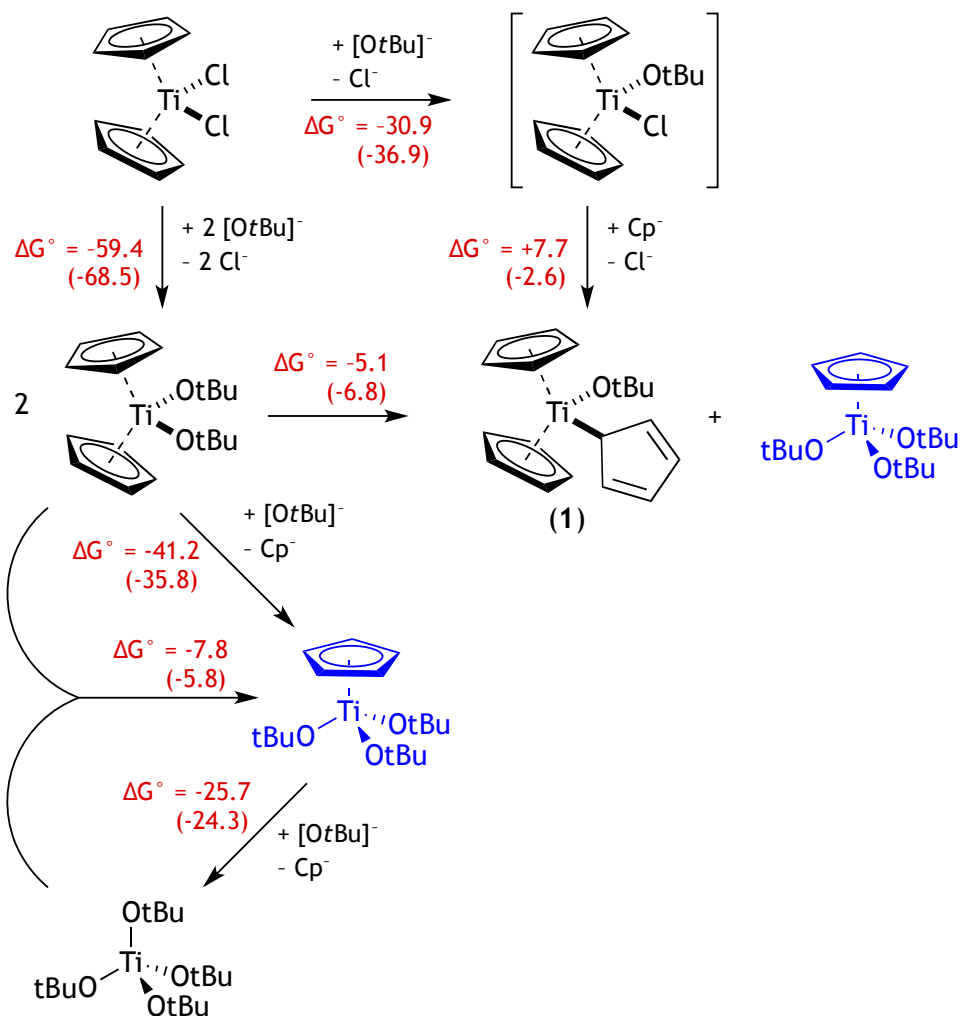


Figure 16. Energy interrelationships between various $\text{Cp}_{2-x}\text{Ti}(\text{OtBu})_{2+x}$ molecules.

Free energies are in kcal mol⁻¹; values in parenthesis include a solvent correction in THF, using the PCM approach. $\text{Cp}_2\text{TiCl}(\text{OtBu})$ was not observed among the products of the reactions in this work, but it is a likely intermediate, and could be involved in the formation of $\text{Cp}_3\text{Ti}(\text{OtBu})$.

The conversion of TDC into $\text{Cp}_2\text{Ti}(\text{OtBu})_2$ is a thermodynamically favored reaction, reflecting the greater strength of Ti–O relative to Ti–Cl bonds. The subsequent conversion of $\text{Cp}_2\text{Ti}(\text{OtBu})_2$ into $\text{CpTi}(\text{OtBu})_3$ is also strongly favored, as is the formation of $\text{Ti}(\text{OtBu})_4$ from $\text{CpTi}(\text{OtBu})_3$. In a reaction with a 2:1 ratio of $\text{K}[\text{OtBu}]$ to TDC, however, there would be

little [OtBu]⁻ available to react with CpTi(OtBu)₃, accounting for the limited formation of Ti(OtBu)₄ (Table 1; #2,4,6).

The two potential routes to **1** discussed above (eq. 1 and 3) are thermodynamically reasonable, especially when a solvent correction is applied. The driving force (ΔG°) for two Cp₂Ti(OtBu)₂ molecules to produce Cp₃Ti(OtBu) (eq. 1) is -5.1 kcal mol⁻¹ (increasing to -6.8 kcal mol⁻¹ with the THF correction). The gas-phase value for the conversion of the proposed Cp₂TiCl(OtBu) into Cp₃Ti(OtBu) (eq. 3) is +7.7 kcal mol⁻¹ (ΔG°), but this drops to -2.6 kcal mol⁻¹ with the THF correction. Other potential routes are unlikely either for steric and/or thermodynamic reasons (e.g., Cp₂Ti(OtBu)₂ + CpTi(OtBu)₃ → Cp₃Ti(OtBu) + Ti(OtBu)₄, $\Delta G^\circ = +10.5$ kcal mol⁻¹; +4.7 kcal mol⁻¹ with the THF correction).

4.3 Conclusions

In summary, the production of group 4 Cp_{2-x}M(OtBu)_{2+x} complexes by halide metathesis is a sensitive function of the reaction conditions employed, and in particular, whether a polar solvent is used or not. Cp ring displacement occurs readily in titanium systems but not at all with the heavier members of group 4; this probably reflects the stronger M–Cp bonding found in Zr and Hf complexes as compared to Ti.¹⁶⁴

Several differences mark the use of mechanochemical activation in these systems. The most obvious is the speed of the reactions, completed in minutes, instead of the hours required by solution synthesis. Also of note is that the product distributions obtained with ball milling and from reactions run in hexanes correspond more closely to each other than to those from reactions conducted in THF (e.g., the 2:1 reactions of K[OtBu] and Cp₂TiCl₂ in hexanes (#4) and by milling (#6) produce roughly half the amount of Cp₂Ti(OtBu)₂ as does the same

reaction in THF (#2); the major product from hexanes/milling is also the same, CpTi(OtBu)₃). This may basically reflect that fact that in both hexanes/milling a polar reaction medium is absent. Unless there are unusual issues of stereochemistry involved,³ solid-state activations may be more broadly useful in recreating the products of organometallic halide metatheses conducted in alkanes, but at much higher speed, a possibility we are exploring.

4.4 Experimental

General Considerations. All syntheses were conducted under rigorous exclusion of air and moisture using Schlenk line and glovebox techniques. Proton (¹H) and carbon (¹³C) NMR spectra were obtained at ambient temperature on a Bruker AV-400 MHz spectrometer. Proton and carbon spectra were referenced to the residual resonances of C₆D₆. Variable temperature ¹H NMR was obtained on a Bruker DRX-500 instrument and referenced to residual resonances of tol-d₈. Metal and combustion analyses were performed by ALS Environmental, Tucson, AZ.

Bis(cyclopentadienyl)metal dichlorides were obtained from Strem Chemicals and used as received. Anhydrous inhibitor-free tetrahydrofuran (THF) was stored over molecular sieves prior to use. Hexanes and diethyl ether were distilled under nitrogen in the presence of potassium metal prior to use. Deuterated benzene and deuterated toluene (tol-d₈) were purchased from Cambridge Isotopes and were distilled from Na/K (22/78) alloy prior to use.

Synthesis of Complexes

Mechanochemical protocol. Ball milling reactions used 50 stainless steel (440 grade) ball bearings (6 mm) that were thoroughly cleaned with hexanes and acetone prior to use.

Planetary milling was performed with a Retsch PM100 mill, 50 mL stainless steel grinding jar type C, and a safety clamp for air-sensitive grinding. A typical reaction involved 300 mg total sample weight, sealed under an inert atmosphere. The ground mixture was extracted with minimal hexanes (<100 mL) and filtered through a medium porosity ground glass frit. The filtrate was then dried under vacuum prior to NMR analysis. For the preparation of larger quantities of compounds, solution-based synthesis, detailed below, were employed.

Cp₃Ti(OtBu) (1). A 125 mL Erlenmeyer flask was equipped with a magnetic stirrer bar and charged with Cp₂TiCl₂ (1.24 g, 5.0 mmol) in 25 mL THF. A solution containing K[OtBu] (1.12 g, 10.0 mmol) in 25 mL THF was added to the flask. Upon addition of K[OtBu], the red Cp₂TiCl₂ solution in the flask turned yellow-brown and maintained this color. After 18 h, the reaction mixture was dried to remove THF. The resulting material was then extracted with hexanes and filtered through a fritted filter to remove precipitated KCl; the precipitate was washed twice with 10 mL aliquots of hexanes. The solvent was removed from the red solution to leave a red solid and yellow oil. The product was then washed with hexanes, and hexanes was removed by pipet to leave red solid with no observable yellow oil (0.36 g, 23%). ¹H NMR (400 MHz, C₆D₆, 298 K): δ 1.01 (s, 9H, OC(CH₃)₃), 5.74 (br s, *w*_{1/2} = 22 Hz, 10H, C₅H₅). The single broad resonance for the Cp ligands in Cp₃Ti(OtBu) is evidently the result of fluxional behavior. Cooling a sample to 225 K results in the Cp peak shifting upfield to δ5.32 ppm and broadening further to *w*_{1/2} = 53 Hz; there is no sign of splitting. Conversely, raising the temperature to 325 K causes it to narrow to *w*_{1/2} = 11 Hz. ¹³C NMR (100 MHz, C₆D₆, 298 K): δ 31.61 (s, CH₃), 84.93 (s, OC(CH₃)₃), 112.40 (s, C₅H₅). Anal. Calcd for C₁₉H₂₄O₂Ti: C, 72.2; H, 7.6. Found: C, 71.6; H, 7.5.

Solution synthesis of Cp₂Zr(OtBu)₂ (2). A 125 mL Erlenmeyer flask was equipped with a magnetic stirrer bar and charged with Cp₂ZrCl₂ (0.294 g, 1.01 mmol). A solution containing K[OtBu] (0.224 g, 2.00 mmol) in 70 mL diethyl ether was added to the flask. Upon dissolution, the material in the flask turned canary yellow, but became peach-colored after 5 min of additional stirring. After 8 h, the reaction mixture was filtered through a fritted filter to remove precipitated KCl; the precipitate was washed twice with 10 mL aliquots of diethyl ether. The solvent was removed from the yellow filtrate under vacuum to leave a yellow-brown solid. The product was recrystallized by slow evaporation of hexanes (0.32 g, 87% yield). The white crystals could be sublimed under 500 mTorr of vacuum at 150 °C. The compound was identified by its characteristic NMR spectrum:¹² ¹H NMR (400 MHz, C₆D₆, 298 K): δ 1.16 (s, 18H, OC(CH₃)₃), 5.99 (s, 10H, C₅H₅). ¹³C NMR (100 MHz, C₆D₆, 298 K): δ 32.58 (s, CH₃), 76.23 (s, OC(CH₃)₃), 113.30 (s, C₅H₅). Anal. Calcd for C₁₈H₂₈O₂Zr: Zr, 24.8. Found: Zr, 24.9.

Cp₂HfCl(OtBu) (3). A 125 mL Erlenmeyer flask was equipped with a magnetic stirrer bar and charged with Cp₂HfCl₂ (0.2514 g, 0.66 mmol) in 40 mL hexanes. A solution containing K[OtBu] (0.0747 g, 0.66 mmol) in 10 mL hexanes was added to the flask. Upon mixing, the material in the flask became cloudy-white. After 18 h, the reaction mixture was filtered through a fritted filter to remove precipitated KCl; the precipitate was washed twice with 10 mL aliquots of hexanes. The solvent was removed from the colorless filtrate under vacuum to leave a white solid. The product was recrystallized by slow evaporation of hexanes (0.233 g, 84% yield). ¹H NMR (400 MHz, C₆D₆, 298 K): δ 1.08 (s, 18H, OC(CH₃)₃), 5.91 (s, 10H, C₅H₅). ¹³C NMR (100 MHz, C₆D₆, 298 K): δ 31.18 (s, CH₃), 78.35 (s, OC(CH₃)₃), 111.94 (s, C₅H₅). Anal. Calcd for C₁₄H₁₉ClHfO: C, 40.3; H, 4.6; Hf, 42.8. Found: C, 39.8; H,

4.5; Hf, 43.4.

Cp₂Hf(OtBu)₂ (4). A 125 mL Erlenmeyer flask was equipped with a magnetic stir bar and charged with Cp₂HfCl₂ (0.306 g, 0.81 mmol) in 40 mL hexanes. A solution containing K[OtBu] (0.181 g, 1.61 mmol) in 10 mL hexanes was added to the flask. Upon mixing, the material in the flask became turbid. After 18 h, the reaction mixture was filtered through a fritted filter to remove precipitated KCl; the precipitate was washed twice with 10 mL aliquots of hexanes. The solvent was removed from the colorless filtrate under vacuum to leave a white solid (0.31 g, 85% crude yield). The solid can be sublimed under 300 mTorr of vacuum at 120 °C. ¹H NMR analysis indicated that the sublimed product contained ca. 14% of **3**. ¹H NMR for **4** (400 MHz, C₆D₆, 298 K): δ 1.16 (s, 18H, OC(CH₃)₃), 5.99 (s, 10H, C₅H₅). ¹³C NMR (100 MHz, C₆D₆, 298 K): δ 32.00 (s, CH₃), 75.49 (s, OC(CH₃)₃), 110.31 (s, C₅H₅). Anal. Calcd for (C₁₈H₂₈HfO₂)_{0.86}(C₁₄H₁₉ClHfO)_{0.14}: C, 46.6; H, 6.0. Found: C, 45.5; H, 6.4.

General Procedures for X-ray Crystallography

Compounds 1 and 3. A suitable crystal of each sample was located, mounted in a polyimide loop, and mounted on an Agilent SuperNova (Dual, Cu at zero, EosS2) diffractometer. The crystals were kept at 100 K during data collection. Using Olex2,¹⁶⁵ the structure was solved with the SHELXT¹⁶⁶ structure solution program using direct methods and refined with the SHELXL¹⁶⁷ refinement package using least squares minimization. All non-hydrogen atoms were refined with anisotropic displacement parameters. Except for the unique hydrogen H1 on C1 in **1**, all hydrogen atoms were placed in ideal positions and refined as riding atoms with relative isotropic displacement parameters. The methyl groups were

idealized and refined as rotating groups. Table 2 and CCDC 1496571 and 1496573 contain additional crystallographic data for additional crystal and refinement information.

Compounds 2 and 4. A suitable crystal of each sample was located, attached to a glass fiber, and mounted on a Bruker SMART APEX II CCD platform diffractometer for data collection.¹⁶⁸ The structures were solved using SIR97¹⁶⁹ and refined using SHELXL-97 (for $\text{Cp}_2\text{Zr}(\text{OtBu})_2$)¹⁷⁰ and SHELXL-2013.¹⁷¹ In both cases, the space group $P4_2m$ was determined based on systematic absences. A direct-methods solution was calculated which provided most non-hydrogen atoms from the E-map. Full-matrix least squares/ difference Fourier cycles were performed which located the remaining non-hydrogen atoms. All non-hydrogen atoms were refined with anisotropic displacement parameters. All hydrogen atoms were placed in ideal positions and refined as riding atoms with relative isotropic displacement parameters. Table 2 and CCDC 1496572 and 1496574 contain additional crystallographic data.

General computational considerations

All calculations were performed with the Gaussian 09W suite of programs.¹¹¹ The global hybrid M06 DFT functional^{116, 162} was used, which includes accounting for dispersion interactions, and includes 27% of exact exchange. The def2TZVPD basis set was used on the metal atoms and chlorine; for Zr and Hf an effective core potential was used to account for relativistic effects. The def2SVPD basis was used on all other atoms.¹¹⁶ An ultrafine grid was used for all calculations (Gaussian keyword: int=ultrafine). Molecules were studied both in vacuum and in THF with a solvation model (PCM).¹⁶³ The nature of the stationary points was determined with analytical frequency calculations; all optimized geometries were found to be

minima ($N_{\text{imag}} = 0$).

(This work was adapted from: Boyde, N. C., et al. *Dalton Trans.* **2016**, 45, 18635)

CHAPTER 5

Multicomponent mechanochemical synthesis of cyclopentadienyl titanium

alkoxy halides

5.1 Introduction

The neutral d^0 $Cp'_xML_yL'_{4-(x+y)}$ framework comprises an enormous number of complexes in early transition metal and actinide chemistry.¹⁷² Part of the reason for this is that with four potentially different ligands on the metal center (i.e., Cp', Cp'', L', L''), the combinational possibilities with the metallocene structure are considerable. In addition, the range of compatible L and L' ligands is large, and includes halides, phosphines,¹⁷³ carbonyls,¹⁷⁴ alkoxides, carbenes,¹⁷⁵⁻¹⁷⁶ metal-based ligands,¹⁷⁷⁻¹⁷⁸ and substituted Cp rings,¹⁷⁹ among others. Many applications have been developed for the complexes, principally in catalysis (e.g., syndiotactic polymerization of styrene,¹³⁹ olefin polymerization,^{140-141, 180-181} polymerization of lactide monomers and ϵ -caprolactone¹⁴²⁻¹⁴⁴), but also in CVD production of thin-film oxides^{12, 145} and carbides.¹⁸² The very flexibility that makes the metallocene framework so versatile also complicates the synthesis of specific compositions.

Consider a special subset of the complexes in which the cyclopentadienyl ligands are C_5H_5 , L' is a halide and L'' is an alkoxide; even so restricted, 15 general compositions can satisfy the $Cp_xMX_y(OR)_{4-(x+y)}$ formula (Figure 17). Remarkably, for the set of $M = Ti$, $X = Cl$, and $R = OtBu$, all of the compounds with the exception of $Cp_2TiCl(OtBu)$ are known ($Cp_3Ti(OtBu)$ was reported only recently).¹⁷⁹ This is one of the better represented families, however; with the sole change of X to Br, for example, none of the heteroleptic bromo $Cp_xTiBr_y(OtBu)_{4-(x+y)}$ or $TiBr_x(OtBu)_{4-x}$ complexes have been described. Even when known,

the assembly of particular ligands sets in a $\text{Cp}_2\text{M(L)X}'$ complex is not always straightforward. The dichlorides Cp_2MCl_2 are commonly used starting materials for bis(cyclopentadienyl) derivatives, but the reaction of Cp_2TiCl_2 and 2 equiv $\text{Li}[\text{OtBu}]$ yields not only $\text{Cp}_2\text{Ti}(\text{OtBu})_2$ (61%), but also $\text{CpTi}(\text{OtBu})_3$ (26%) and $\text{Ti}(\text{OtBu})_4$ (13%).¹⁷⁹ Similarly, the reaction of Cp_2ZrCl_2 and $(\text{Li or Na})[\text{OtBu}]$ yields an inseparable mixture of $\text{Cp}_2\text{ZrCl}(\text{OtBu})$ and $\text{Cp}_2\text{Zr}(\text{OtBu})_2$, even with the use of more than 2 equiv of the alkoxide.¹²

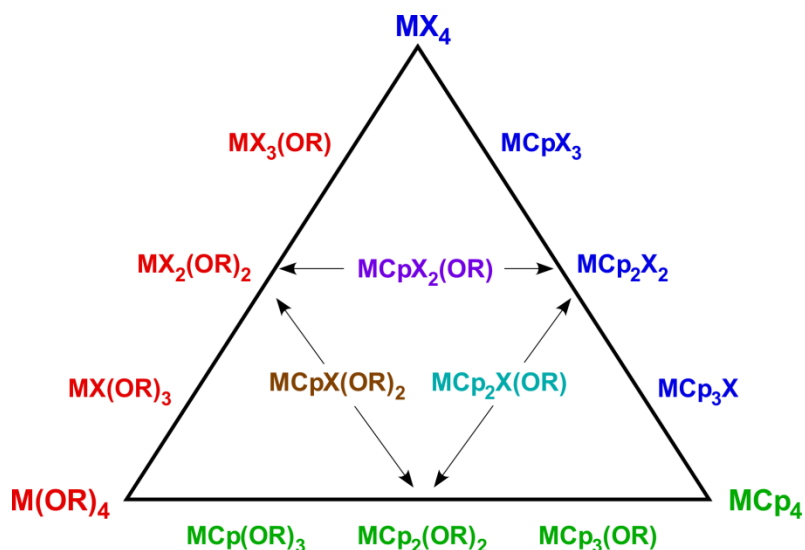


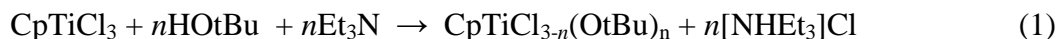
Figure 17. Combinatorial possibilities of mixed group 4 $\text{Cp}_x\text{MX}_y(\text{OR})_{4-(x+y)}$ complexes, starting from the homoleptic species MX_4 , $\text{M}(\text{OR})_4$, and MCp_4 . Complexes along the edges have two types of ligands; those in the interior have three.

We have explored the use of both solvent-based and mechanochemical reactions to expand the palette of known synthetic routes to $\text{Cp}_x\text{TiX}_y(\text{OR})_{4-(x+y)}$ ($\text{X} = \text{Cl, Br; R} = \text{Me, Et, OiPr, OtBu}$). Mechanochemical methods of synthesis, which use mechanical force (typically grinding or milling) to promote reactions, usually under solvent-free conditions, have been investigated for the preparation of inorganic¹⁸³⁻¹⁸⁶ and organometallic compounds.¹⁸⁷ Such reactions can occur on a much faster time scale than equivalent than solution methods,¹⁸⁸ and

can yield unique products that have not successfully been isolated from solution.¹⁸⁹⁻¹⁹⁰ The distribution of products and isomers can also be tuned.^{138, 179, 191} The solvent-free approach also provides the flexibility to use reagents that are not compatible with typical solvents, especially ethers. As demonstrated below, this proves to be especially valuable in work with titanium halides.

5.2 Results and Discussion

Synthesis. A long-known method for conducting halide-alkoxide exchange in group 4 cyclopentadienyl halide complexes is through reaction with the desired alcohol and an added base, typically Et₃N.¹⁹² This provides control over substitution, as indicated in eq. 1 ($n = 2$ or 3).¹⁴⁸



We used a related approach starting from Cp₂TiCl₂ to prepare Cp₂TiCl(OMe)¹⁹³ (**1**) and the previously unknown Cp₂TiCl(OiPr) (**2**). These reactions are slow (ca. 16 h), and when considering the synthesis of the mono-alkoxy derivative Cp₂TiCl(OtBu) (**3**) we investigated halide metathesis instead. This approach has been used to form Cp₂ZrCl(OtBu) in THF,¹² although it fails for Cp₂HfCl(OtBu).¹⁷⁹ Mechanochemical activation works successfully for both of the heavier group 4 metals, however, and it was adopted for the preparation of **3**. It was not assured that the reaction would be clean, as our previous investigation into t-butoxide substitution on Cp₂TiCl₂ demonstrated that at ratios of [OtBu]⁻ : Cp₂TiCl₂ ≥ 2, mixtures of products were obtained whose composition depended on whether or not solvent was used in the reaction, and if so, whether it was THF or hexanes.¹⁷⁹ With the use of equimolar ratios of K[OtBu] to Cp₂TiCl₂, however, mechanochemical activation yielded **3** exclusively (63%

isolated yield) by grinding for 15 min at 600 rpm. The synthesis of **3** completes the set of $\text{Cp}_x\text{TiX}_y(\text{OtBu})_{4-(x+y)}$ compounds (Figure 17) for $X = \text{Cl}$, and $R = \text{OtBu}$.

TiBr_4 reacts with ethereal solvents at room temperature,¹⁹⁴ and thus mechanochemistry was chosen for the preparation of alkoxybromo derivatives.¹⁹⁵ The one pot synthesis of $\text{Cp}_2\text{TiBr}(\text{OtBu})$ (**4**) was accomplished by milling TiBr_4 , $\text{Li}[\text{OtBu}]$, LiCp in a 1:1:2 molar ratio for 15 min (eq 2):



Non-stoichiometric products are not uncommonly generated from mechanochemically induced halide metathesis,¹⁷⁹ and **4**, isolated in modest yield (52%) is also accompanied by $\text{CpTiBr}(\text{OtBu})_2$ (**6**). Adjusting the reaction stoichiometry of TiBr_4 , $\text{Li}[\text{OtBu}]$, LiCp to 1:1:1 and 1:2:1 ratios forms $\text{CpTiBr}_2(\text{OtBu})$ (**5**) and $\text{CpTiBr}(\text{OtBu})_2$ (**6**), respectively. Perhaps not surprisingly, compound **5**, formed from the simplest ratio of reagents, is the bromo complex that is consistently formed most cleanly. Compound **6**, which is produced with a larger amount of the t-butoxide than **5**, is usually accompanied with the homoleptic alkoxide $\text{Ti}(\text{OtBu})_4$. Such differences reflect the role that kinetic factors play in mechanochemical synthesis, as grinding and milling environments are often far from equilibrium.¹⁹⁶⁻¹⁹⁹

All the compounds **1-6** are air- and moisture sensitive, and soluble in hydrocarbons; with the exception of **6**, they are solids at room temperature. The mono(cyclopentadienyl)-monobromo complex **6** is isolated as an orange oil.

Crystal Structures. Crystals of **1** and **2** that were suitable for X-ray diffraction were grown from toluene; those for **3–5** were grown from hexanes. Comparative listings of selected bond lengths and angles are found in Table 1.

Cp₂TiCl(OMe) (1). Both the synthesis and an X-ray structure determination of **1** have been reported.¹⁹³ The room temperature (295 K) structure was affected by disorder in the Cp rings that could not be satisfactorily modeled. Interestingly, in the low-temperature version, the Cp rings are not disordered, but there is a second chlorine position possibly arising from co-crystallized Cp₂TiCl₂; its occupancy refined (9%) with a Ti-Cl bond similarity restraint. Nevertheless, both the original and our low-temperature redetermination agree on the pseudotetrahedral nature of the molecule, defined by the centroids of the two Cp rings, the chloride, and the oxygen of the methyl group. The Ti-Cl, Ti-O, and Ti-ring centroid distances in the two structures differ by less than 0.01 Å, and the Cl-Ti-O angles differ by only 0.19°. The major difference involves only the methoxy ligand; the O1-C1 bond distance is 0.05 Å longer in the redetermined structure, and the Ti-O-C bond angle has contracted by 2.9°. Although the crystallographic issues that affect both structures place limits on what can be said definitively, the low-temperature structure parameters are more in line with those of Cp₂TiCl(OEt); e.g., the C-O distance in the ethoxy derivative (1.415(4) Å) is not statistically distinguishable from that in the low-temperature **1**, and the Ti-O-C angles, although differing by 5.3°, are closer than the ethoxy/room temp methoxy values (8.2°). Computational results (see below) also provide a better fit with the present low-temperature structure.

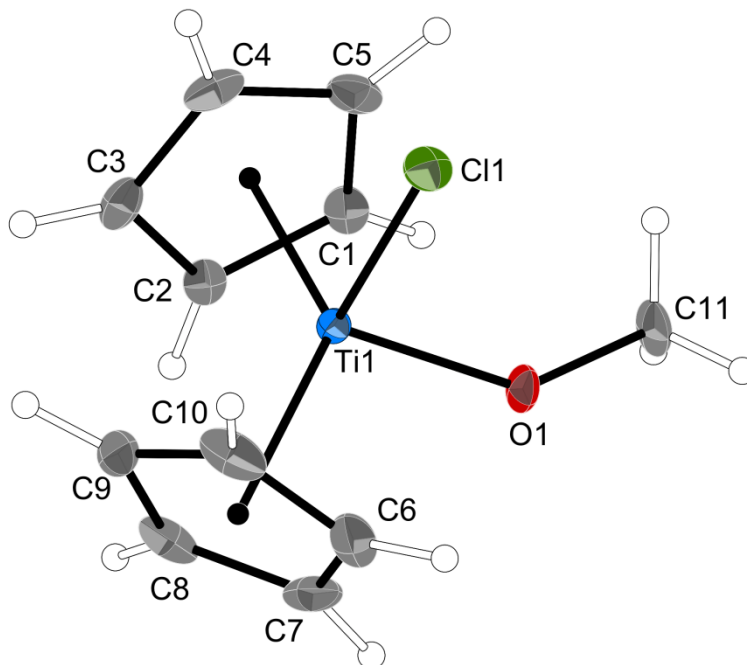


Figure 18. Thermal ellipsoid plot of $\text{Cp}_2\text{TiCl}(\text{OMe})$

Thermal ellipsoid plot of $\text{Cp}_2\text{TiCl}(\text{OMe})$ (50% level); hydrogens have arbitrary radii. A second chloride (2.326 Å from Ti see text) has been removed for clarity. Selected bond distances (Å) and angles (deg): Ti1–O1, 1.8300(19); Ti1–C11 = 2.4215(3); O1–C11, 1.419(2); Ti–Cp'(ring centroid), 2.083 (ave); O1–Ti1–C11, 93.61(5); Ti1–O1–C11, 138.53(13); Cp'–Ti–Cp', 130.9.

$\text{Cp}_2\text{TiCl}(\text{OiPr})$ (2). Compound **2** shares the same pseudotetrahedral structure with **1** and $\text{Cp}_2\text{TiCl}(\text{OEt})$; in the case of **2**, both the Cp rings and OiPr ligand are disordered. One set of these is depicted in Figure 19. In particular, the alkoxide ligand is disordered across a crystallographically imposed mirror plane; i.e., Cl1, Ti1, O1, C7 and C8 all lie in the plane; C6 is disordered above and below it (50:50). The general details of **2** mimic those of **1**, in that the Ti–ring centroid distances differ only by 0.03 Å, and the Ti–Cl bond lengths are within 0.02 Å of each other. Although allowance must be made for the possible effects of disorder, details of the geometry of the isopropoxy ligand suggest a change in the metal ligand bonding compared to that in **1** and $\text{Cp}_2\text{TiCl}(\text{OEt})$. The Ti–O bond has shortened to 1.802(3) Å, and the Ti–O–C angle has widened to 160.0(3)°, features that are consistent

with some π bonding character between Ti and the isopropoxy oxygen. The C–O distance of 1.309(6) Å, however, although not an unprecedented value for such a bond, is nearly 0.1 Å shorter than that found in any of the other complexes in this study. It also is not supported by computational modeling (see below), suggesting that the ligand disorder may indeed be creating an artificially shortened bond length.

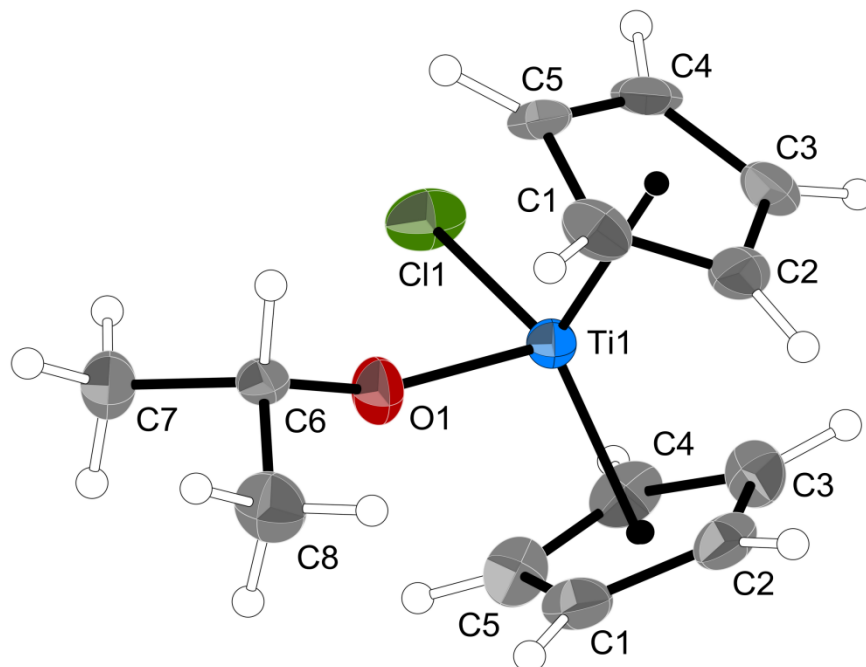


Figure 19. Thermal ellipsoid plot of $\text{Cp}_2\text{TiCl}(\text{OiPr})$

Thermal ellipsoid plot of **2** (40% level); hydrogens have arbitrary radii. Only one conformation of the disordered isopropyl and cyclopentadienyl ligands is shown. Selected bond distances (Å) and angles (deg): Ti1–O1, 1.802(3); Ti1–Cl1 = 2.4031(16); O1–C6, 1.309(6); Ti–Cp⁺(ring centroid), 2.052 (ave); O1–Ti1–Cl1, 94.87(13); Ti1–O1–C6, 160.0(3); Cp⁺–Ti–Cp⁺, 129.0.

$\text{Cp}_2\text{TiCl}(\text{OtBu})$ (3**).** Compound **3** is not affected by the disorder problems in **1** and **2**, and interpretations of its structural features can be made more confidently. Comparisons of **3** are most readily made to the disorder-free structure of $\text{Cp}_2\text{TiCl}(\text{OEt})$, which is proposed to represent a sterically unencumbered $\text{Cp}_2\text{TiCl}(\text{OR})$ complex.²⁰⁰ In this regard, the similarities

between $\text{Cp}_2\text{TiCl}(\text{OEt})$ and **3** are noteworthy. The Ti–Cp(centroid) distances and Cp–Ti–Cp' angles in the two complexes differ by only 0.016 Å and 1.0°, respectively. The Ti–Cl distances are also nearly identical (0.005 Å difference), and ca. 0.04 Å longer than in Cp_2TiCl_2 .

The differences between the compounds, however, are the most revealing. The Ti–O–C angle in **3** is 172.5°, 39.3° wider than in $\text{Cp}_2\text{TiCl}(\text{OEt})$, and which to our knowledge is the widest such angle reported for a $\text{Cp}_2\text{TiCl}(\text{OR})$ complex.²⁰¹ It might be thought that given the bulk of the OtBu ligand there could be some steric influence on this value, but the closest intramolecular contact between a carbon atom of the tOBu group and a Cp carbon is at 3.49 Å (C8...C13). Although the comparison is not exact, in $\text{Cp}_2\text{TiCl}(\text{OEt})$ the methylene carbon displays nearest contacts at 3.15 Å and 3.23 Å to Cp carbon atoms. More telling is the short (1.786 Å) Ti–O bond distance in **3**, compared to the 1.855 Å distance in the ethoxide. There is clearly no steric impediment to adopting the very short Ti–O distance in **3**, and it seems clear that the OtBu group is serving as a strong π donor in this complex.

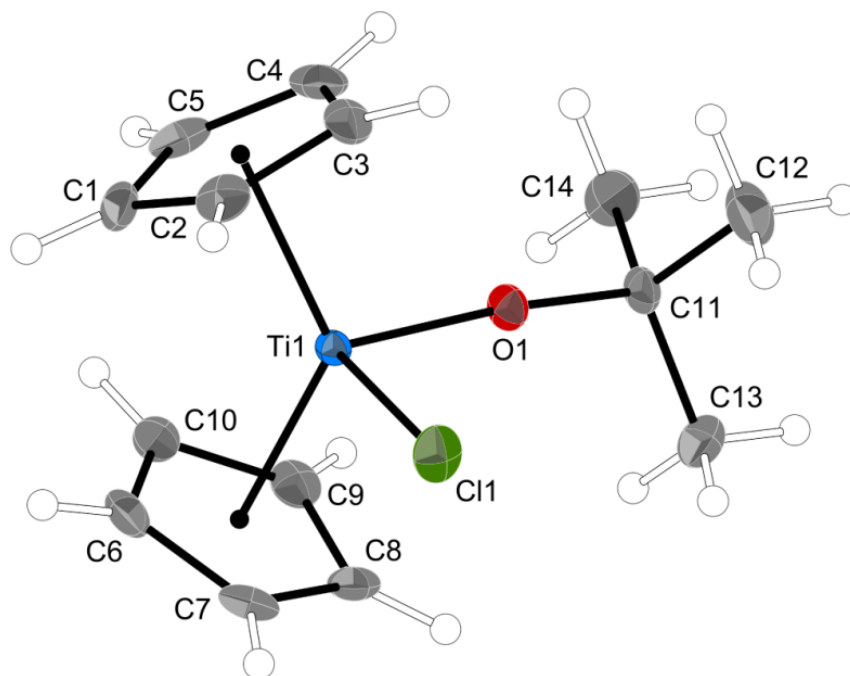


Figure 20. Thermal ellipsoid plot of $\text{Cp}_2\text{TiCl}(\text{OtBu})$

Thermal ellipsoid plot of **3** (50% level); hydrogens have arbitrary radii. Selected bond distances (\AA) and angles (deg): Ti1–O1, 1.7864(9); Ti1–Cl1 = 2.4101(4); O1–C11, 1.4204(14); Ti–Cp'(ring centroid), 2.103 (ave); O1–Ti1–Cl1, 94.40(3); Ti1–O1–C11, 172.48(8); Cp'–M–Cp', 129.5.

$\text{Cp}_2\text{TiBr}(\text{OtBu})$ (4**).** There are two crystallographically independent, but closely similar molecules in the unit cell; only molecule “A” will be discussed here. Not unexpectedly, the bromoalkoxy derivative **4** is isostructural with the chloroalkoxy derivative **3**. They share the same pseudotetrahedral framework, with closely similar Ti–Cp(centroid) distances ($< 0.01 \text{ \AA}$ difference). The Ti–Br bond length matches that in Cp_2TiBr_2 exactly,²⁰² and is 0.12 \AA longer than the Ti–Cl distance in **3**, which is slightly shorter than the difference in covalent radii (0.18 \AA).⁵³ The tert-butoxy ligand bonding is also similar to that in **3**, in regards to the Ti–O and O–C distances and the Ti–O–C angle (0.012 \AA , 0.006 \AA , and 3.3° difference, respectively). The differences, although small, are in the direction that indicates

that the less electronegative bromide ligand provides less competition for π bonding to the metal than does chloride. This is reflected in the contraction of the Ti–O bond and the widening of the Ti–O–C angle. There is even less reason to suppose any steric influence on the wide Ti–O–C distance in **4**, as the closest intramolecular contact between a carbon atom of the tOBu group and a Cp carbon is now at 3.68 Å (C1...C14).

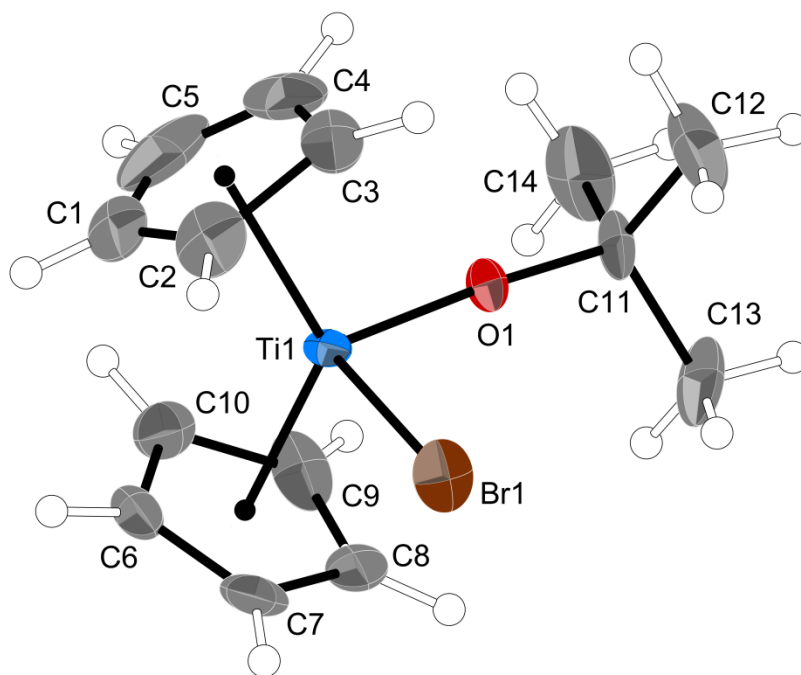


Figure 21. Thermal ellipsoid of $\text{Cp}_2\text{TiBr}(\text{OtBu})$

Thermal ellipsoid plot of **4** (50% level); hydrogens have arbitrary radii. Selected bond distances (Å) and angles (deg): Ti1–O1, 1.774(3); Ti1–Br1 = 2.534(2); O1–C11, 1.414(5); Ti–Cp'(ring centroid), 2.096 (ave); O1–Ti1–Br1, 84.67(16); Ti1–O1–C11, 175.8(3); Cp'–Ti–Cp', 128.8.

CpTiBr₂(OtBu) (5). Like **4**, there are two crystallographically independent, but closely similar molecules in the unit cell of **5**; only molecule “A” will be discussed here. Also like **4**, compound **5** has a pseudotetrahedral geometry, with one of the Cp rings of **4** replaced

with another Br (Figure 22). The molecule possesses approximate, although not crystallographically imposed, C_s symmetry; the atoms C₅, Ti, C₁, C₆, and C₈ are all within 0.03 Å of a least-squares plane drawn through their centers. Consistent with the reduced coordination number, all the distances to the metal have decreased relative to **4**. The Ti–Cp(centroid) distance is smaller in **5** by 0.067 Å, and the Ti–Br distances are 0.10 Å closer. The already short Ti–O distance in **4** is now reduced by 0.047 Å, to 1.727 Å. The Ti–O–C angle in **5** is 173.9°, slightly but not appreciably different from the value in **4**.

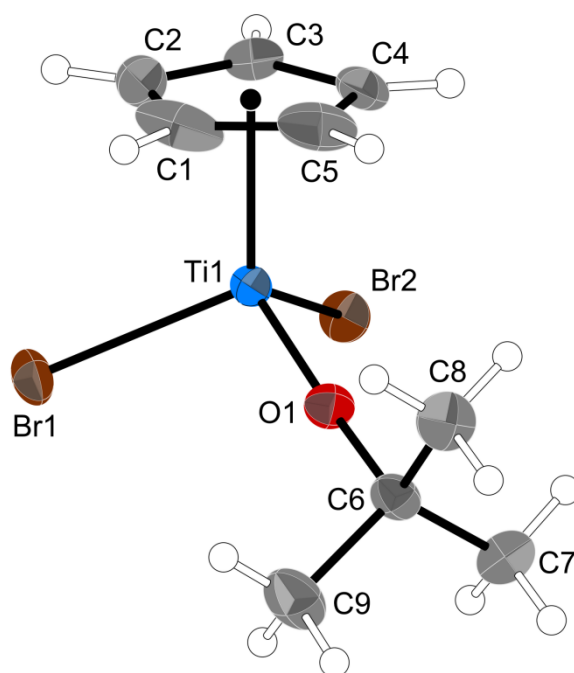


Figure 22. Thermal ellipsoid plot of CpTiBr₂(OtBu)

Thermal ellipsoid plot of **5** (50% level); hydrogens have arbitrary radii. Selected bond distances (Å) and angles (deg): Ti1–O1, 1.7274(18); Ti1–Br1 = 2.4333(5); Ti1–Br2 = 2.4326(5); O1–C11, 1.445(3); Ti–Cp(ring centroid), 2.024 (ave); Br1–Ti1–Br2, 103.05(2); O1–Ti1–Br1, 101.69(7); O1–Ti1–Br2, 101.88(7); Ti1–O1–C6, 173.95(19).

Calculation results. The new complexes described here provide a basis for examining a long-standing issue of the unusual geometries displayed by terminal transition metal alkoxides.[ref] Many such alkoxides of the 2nd and 3rd row early transition metals and lanthanides (e.g., Zr, Nb, Ta, Sm) possess nearly linear M–O–R angles and short M–O distances, although there is no obvious correlation between the distances and angles.²⁰³ Several sources for the linear structures have been proposed, including steric crowding (bulkier alkoxides tend to display the most linear M–O–R angles), π -bonding between occupied p orbitals of the ligand and empty metal orbitals, or conversely, ionic contributions to the bonding ($M^{\delta+}O^{\delta-}$). A role has also been assigned to electrostatic repulsion between the α carbon of the alkoxide and the metal centers.¹⁵⁸ There are also issues with solid-state artifacts, specifically crystal packing effects and disordered ligands, which can obscure inferences made about bonding arrangements.

With early first-row metals, a wide range of M–O–R angles has been observed, including widely different angles for the same alkoxide type on the same metal center (e.g., in the 2-methyl-quinolin-8-olate complex $Ti(C_{10}H_8NO)_2(OiPr)_2$, the two isopropoxide ligands have Ti–O–C angles of 126.7° and 154.1°).²⁰⁴ We were interested in the opportunity that the present set of complexes offered for illuminating the bonding forces involved in the $Cp_xMX_y(OR)_{4-(x+y)}$ series. Density functional theory calculations were undertaken specifically to look for evidence of π -bonding in the alkoxides with the most linear Ti–O–C bonds.

Preliminary studies using the hybrid M06¹⁶² and APF-D²⁰⁵ global hybrid functionals provided somewhat disappointing reproduction of the crystallographic structures, with

deviations in Ti–O bond lengths up to 0.08 Å and differences of more than 8° in Ti–O–C angles. Tests with the double hybrid B2PLYP functional,²⁰⁶ which incorporates perturbative second-order correlation (PT2) that is obtained from the Kohn-Sham (GGA) orbitals and eigenvalues, were more encouraging, and were used for subsequent studies. Not unexpectedly, reproducing internal angles is more difficult than bond distances. Individual molecules are discussed below.

1) Cp₂TiCl(OMe) (**1**). Although the calculated Ti–O–C angle is 4.6° smaller than that in the original room-temperature structure determination, it is only 1.7° smaller than that in the present redetermined low-temperature geometry, providing confidence that, despite some continuing issues with disorder, the latter is the more reliable figure.

2) Cp₂TiCl(OiPr) (**2**). The wide Ti–O–iPr angle of 160.0° found in the crystal structure cannot be matched by the B2PLYP calculations, which underestimates it by 12.3° (the underestimation was even larger (15.4°) with the M06 functional), but the large difference leads us to believe that the crystallographically observed structure, suffering as it does from disorder both in the isopropoxy group and cyclopentadienyl rings, cannot be used uncritically. The Ti–Cl and Ti–O bonds exhibit only modest under- and overestimation (by 0.16 Å and 0.029 Å, respectively).

3) Cp₂TiCl(OtBu) (**3**). The calculated Ti–O–C angle is smaller than the crystallographic value by 4.5°, although the Ti–Cl and Ti–O bonds are in good agreement, with a mismatch of 0.016 Å (under) and 0.014 Å (over), respectively.

4) $\text{Cp}_2\text{TiBr}(\text{OtBu})$ (**4**). The calculated Ti–O–C angle underestimates the crystallographic value by 5.2° , although the Ti–Br and Ti–O bonds are slightly overestimated, by 0.051 \AA and 0.023 \AA , respectively.

5) $\text{CpTiBr}_2(\text{OtBu})$ (**5**). The calculated Ti–O–C angle is larger than the crystallographic value by 5.0° ; the Ti–Br and Ti–O bonds display good agreement, with a mismatch of 0.003 \AA (under) and 0.028 \AA (over), respectively.

π -Bonding in cyclopentadienyl alkoxide complexes. Where there is no evidence for steric crowding or crystallographic disorder, a wide Ti–O–C angle accompanied by a shortened Ti–O bond is consistent with the operation of metal-ligand π -bonding.²⁰⁷ The three new compounds reported here, $\text{Cp}_2\text{TiCl}(\text{OtBu})$, $\text{Cp}_2\text{TiBr}(\text{OtBu})$, and $\text{CpTiBr}_2(\text{OtBu})$, all meet these structural criteria, as they have Ti–O–C angles $>170^\circ$ and Ti–O bonds of $< 1.80 \text{ \AA}$

An inspection of the selected orbitals of $\text{Cp}_2\text{TiCl}(\text{OtBu})$ makes it obvious that two of them display evidence of π -bonding between Ti and O (Figure 23; the x axis is coincident with the Ti–O bond; the Cl lies in the xz plane). In MO#69 (HOMO-6, Figure 23a), the Ti is involved in sigma bonding to the Cl as well as π -type bonding to the oxygen. An NBO analysis of the composition indicates that for oxygen, 98% of its contribution to the MO is from its $2p_z$ orbital. For Ti, both its $3d_{z^2}$ and $3d_{xz}$ orbitals are involved, in a ratio of roughly 3:5. In MO#68 (HOMO-7, Figure 23b), the Ti is again involved in π -type bonding to the oxygen. The contribution from oxygen is 30.5% of the total MO, and 99% of this is from the $2p_y$ orbital. Almost 84% of titanium's contribution is from the $3d_{xy}$ orbital, with smaller amounts from the $3d_{yz}$. Much lower in energy (MO#48) are orbitals that represent Ti–O sigma bonding (Figure 23c) and the C–H bonds in the OtBu ligand. More than 95% of the

contribution of oxygen to the MO is from the $2p_x$ orbital. Most of oxygen's contribution is from the $3d_{x^2-y^2}$ orbital.

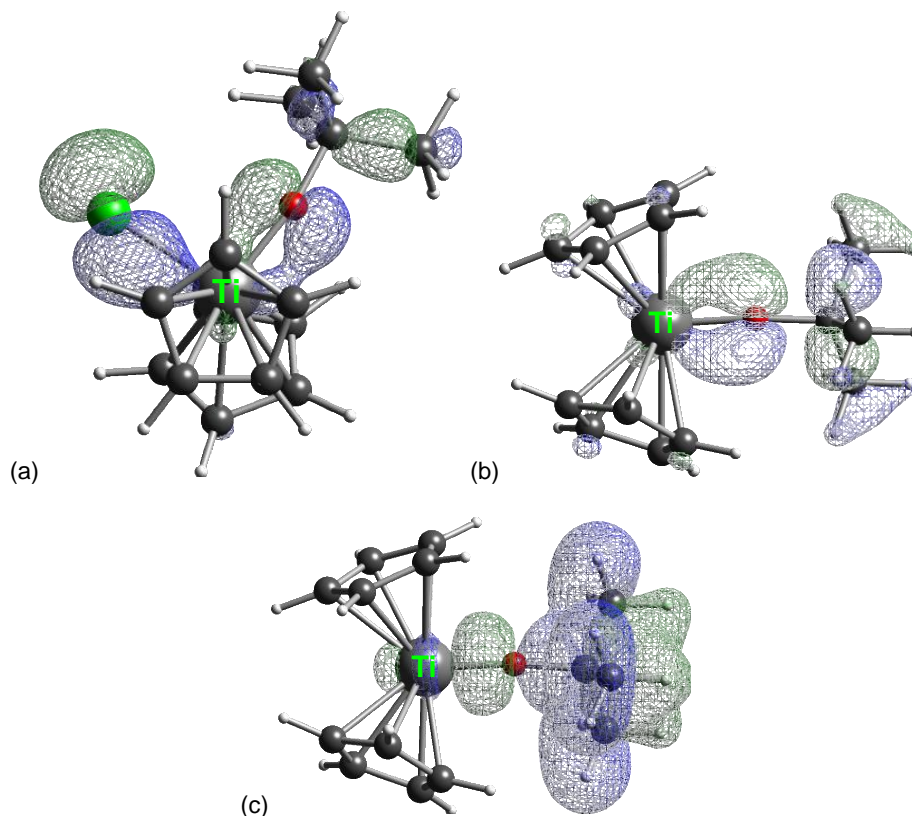


Figure 23. Molecular orbitals of $\text{Cp}_2\text{TiCl}(\text{OtBu})$

(a) MO#69 of $\text{Cp}_2\text{TiCl}(\text{OtBu})$. (b) MO#68 of $\text{Cp}_2\text{TiCl}(\text{OtBu})$. The isodensity surface for the two orbitals is 0.050. (c) MO#48 of $\text{Cp}_2\text{TiCl}(\text{OtBu})$; isodensity surface = 0.025.

A similar arrangement of orbitals exists for $\text{CpTiBr}_2(\text{OtBu})$. In MO#76 (HOMO-8, Figure 24a), the Ti is involved in sigma bonding to the Cl as well as π -type bonding to the oxygen. An NBO analysis of the composition indicates that for oxygen, over 99% of its contribution to the MO is from its $2p_y$ orbital. For Ti, 88% of its contribution is from the $3d_{xy}$ orbital. Complementary Ti–O π -bonding is found in MO#75 (HOMO-9, Figure 24b), in which over 99% of the contribution of oxygen is from its $2p_z$ orbital; almost 85% of oxygen's

contribution is from the $3d_{xz}$ orbital., with 10.5% from the $4p_z$. As is the case with **3**, the Ti–O sigma interaction is substantially lower in energy (Figure 24c). In MO#57, the overlap is again primarily between the oxygen $2p_x$ orbital and the titanium $3d_{x^2-y^2}$.

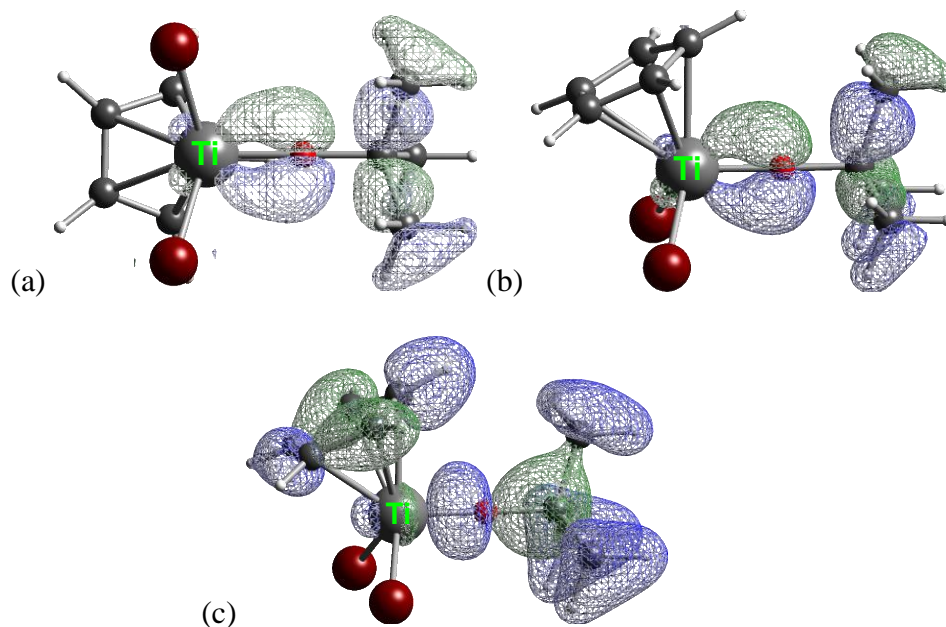


Figure 24. Molecular orbitals of CpTiBr₂(OtBu)

(a) MO#76 of CpTiBr₂(OtBu). (b) MO#75 of CpTiBr₂(OtBu). The isodensity surface for the two orbitals is 0.050. (c) MO#57 of CpTiBr₂(OtBu); isodensity surface = 0.035.

The bonding picture developed here is closely related to that presented for the monocyclopentadienyl CpTiMe₂(OPh) complexes,²⁰⁸ but is more broadly reflective of the ambivalent character of the –OR ligand.²⁰⁹⁻²¹⁰ In brief, it is not possible to draw a satisfactory bonding picture in terms of a single classical Lewis structure. At one limit, the oxygen can be pictured as donating all three of its lone pairs to the titanium, a type of weak triple bond. At the other extreme is an ionic presentation, i.e., [Cp₂TiCl]⁺[OtBu][–], with the actual bonding

situation lying in between (Figure 24). This bonding motif was previously reported to be in a 1:2 ratio; i.e., the Ti–O bond order was approximately one.²⁰⁸

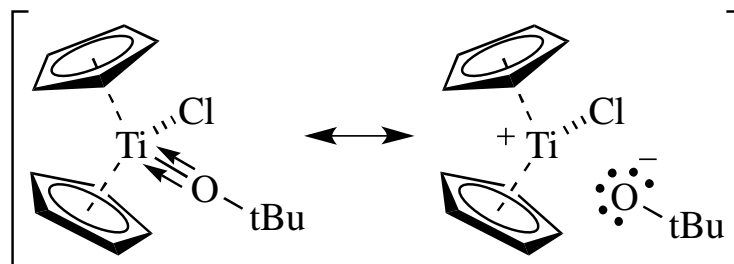


Figure 25. Limiting bonding arrangements for $\text{Cp}_2\text{TiCl}(\text{OtBu})$. Both extremes would support a linear Ti–O–C bond angle.

Table 9. Calculated and crystallographic bond distance and angles of select mixed ligand titanium species

	Ti-Cp (centroid) (Å)	Ti-X (Å)	Ti-O (Å)	Ti-O-R (°)	Ref.
$\text{Cp}_2\text{TiCl}(\text{OMe})$ (1)	2.091 (ave)	2.405(1)	1.839(2)	141.4(3)	¹⁹³
$\text{Cp}_2\text{TiCl}(\text{OMe})$	2.083 (ave)	2.4215(3)	1.8300(19)	138.53(13)	this work
$\text{Cp}_2\text{TiCl}(\text{OMe})$	2.111 (ave.)	2.379	1.844	136.8	Calc
$\text{Cp}_2\text{TiCl}(\text{OEt})$	2.09 (ave.)	2.405(1)	1.855(2)	133.2(2)	²⁰⁰
$\text{Cp}_2\text{TiCl}(\text{OEt})$	2.082 (ave)	2.365	1.860	131.4	Calc
$\text{Cp}_2\text{TiCl}(\text{OiPr})$ (2)	2.052 (ave)	2.4031(16)	1.802(3)	160.0(3)	this work
$\text{Cp}_2\text{TiCl}(\text{OiPr})$	2.116 (ave)	2.387	1.831	147.7	Calc
$\text{Cp}_2\text{TiCl}(\text{OtBu})$ (3)	2.103 (ave)	2.4101(4)	1.7864(9)	172.48(8)	this work
$\text{Cp}_2\text{TiCl}(\text{OtBu})$	2.130(ave)	2.394	1.800	168.0	Calc
$\text{Cp}_3\text{Ti}(\text{OtBu})$	2.112 (η^5)	2.304(1)	1.794(1)	170.88(9)	¹⁷⁹
$\text{Cp}_3\text{Ti}(\text{OtBu})$	2.124	(η^1 -Cp) 2.232	1.743	180.0	Calc
$\text{Cp}_2\text{TiBr}(\text{OtBu})$ (4)	2.096 (ave)	2.534(2)	1.774(3)	175.8(3)	this work
$\text{Cp}_2\text{TiBr}(\text{OtBu})$	2.126 (ave)	2.585	1.797	170.6	Calc
$\text{CpTiBr}_2(\text{OtBu})$ (5)	2.024	2.433(7)(ave)	1.7274(18)	173.95(19)	this work
$\text{CpTiBr}_2(\text{OtBu})$	2.024	2.430	1.755	178.9	Calc

^adef2TZVP(Ti,Br,Cl); defSVP(C,O,H)

5.3 CONCLUSIONS

Mechanochemical synthesis can be used to produce $\text{Cp}_x\text{TiX}_y(\text{OtBu})_{4-(x+y)}$ ($X = \text{Cl}, \text{Br}$) complexes from the mixture of two or three starting materials, depending on whether bis(cyclopentadienyl) or mono(cyclopentadienyl) compounds are desired. Adjustment of the stoichiometric ratios of the reagents is reflected in the composition of the major products, although the outcomes are cleanest if the ratios are 1:1 (as in the production of **3**) or 1:1:1 (as in the formation of **5**). One noticeable advantage of the mechanochemical approach is that TiBr_4 , which reacts at room temperature with ethereal solvents, can be used in the solid state without modification. This probably also applied to TiI_4 , and should make the synthesis of titanium -bromo and -iodo complexes more accessible.

All of the *tert*-butoxide complexes display the hallmarks of π -bonding between the titanium and alkoxide ligand; i.e., short Ti–O bonds and wide Ti–O–C angles. Density functional theory calculations support this interpretation of the bonding.

It is notable that the calculations support an increasingly linear Ti–O–C angle in the order $\text{Me} < \text{Et} < \text{OiPr} < \text{OtBu}$, which comports with the increasing π -donor ability of the ligands. The X-ray crystal structures in general support this ordering, with the notable exception of the ethyloxide complex $\text{Cp}_2\text{TiCl}(\text{OEt})$, whose Ti–O–C angle is the smallest of those studied here. We are at present unsure of the reason for this difference, unless crystal packing effects have a larger than expected influence on the geometry.

5.4 Experimental

General Considerations. All manipulations were performed with the exclusion of air and moisture using high vacuum, Schlenk, or glovebox techniques. Proton and carbon

(^{13}C (1H)) NMR spectra were obtained on a DRX-400 spectrometer at 400 (^1H) and 100.1 (^{13}C) MHz, and were referenced to the residual proton and ^{13}C resonances of C_6D_6 . Elemental analysis was performed by ALS, Tucson, AZ.

Materials. TiBr_4 , LiOtBu , KOtBu , LiCp , and Cp_2TiCl_2 were purchased from commercial suppliers and used as received. Toluene and hexanes were distilled under nitrogen from potassium benzophenone ketyl.¹⁰⁷ Anhydrous THF was stored over molecular sieves. MeOH was obtained from Mbraum MB-SPS. Isopropyl alcohol (IPA) and triethylamine (TEA) were distilled and dried over CaH_2 . C_6D_6 was vacuum distilled from Na/K (22/78) alloy and stored over type 4A molecular sieves prior to use.

Mechanochemical protocol. Ball milling reactions used 50 stainless steel (440 grade) ball bearings ($3/8$ in, 6 mm) that were thoroughly cleaned with hexanes and acetone prior to use. Planetary milling was performed with a Retsch PM100 mill, 50 mL stainless steel grinding jar type C, and a safety clamp for air-sensitive grinding. A typical reaction involved 300 mg total sample weight, sealed under an inert atmosphere. The ground mixture was extracted with minimal hexanes (<100 mL) and filtered through a medium porosity ground glass frit. The filtrate was then dried under vacuum prior to NMR analysis. In the case of TiBr_4 reactions; TiBr_4 was added to the grinding jar first followed by LiCp then $\text{Li}[\text{OtBu}]$. This is to prevent the solid state reaction of the alkoxide with TiBr_4 .

$\text{Cp}_2\text{TiCl}(\text{OMe})$ (1). This was prepared following the literature procedure.¹⁹³ Cp_2TiCl_2 (0.502 g, 2.01 mmol) was added to a Schlenk flask containing 40 mL of THF and a magnetic stir bar. This was stirred at room temperature under N_2 . To this mixture, triethylamine (0.52 mL, 3.7 mmol) and MeOH (0.16 mL, 3.9 mmol) were added. The reaction was allowed to stir

at room temperature for 16 h. The THF was removed in vacuo. The resulting product was then extracted with toluene to yield an orange filtrate. The toluene was removed to afford 0.441 g (90% yield) of an orange solid. ^1H NMR (400 MHz, C_6D_6 , 298 K): δ 4.06 ppm (s, 3H, CH_3), δ 5.88 (s, 10H, C_5H_5). ^{13}C NMR (100 MHz, C_6D_6 , 298 K): δ 70.7 (s OCH_3), δ 117.0 (s C_5H_5).

$\text{Cp}_2\text{TiCl}(\text{OEt})$. This was prepared similar the literature procedure. Cp_2TiCl_2 (0.4876g, 1.96 mmol) was added to a Schlenk flask containing 40 mL of THF and a magnetic stir bar. This was stirred at room temperature under N_2 . To this mixture, triethylamine (0.52 mL, 3.87 mmol) and EtOH (0.22 mL, 3.8 mmol) were added. The reaction was allowed to stir at room temperature for 16 h. The THF was removed in vacuo. The resulting product was then extracted with toluene to yield an orange filtrate. The toluene was removed to afford 0.297 g (59 % yield) of an orange solid. ^1H NMR (400 MHz, C_6D_6 , 298 K): This was confirmed by the characteristic ^1H NMR shift. (ref)

$\text{Cp}_2\text{TiCl}(\text{OiPr})$ (2). Cp_2TiCl_2 (0.500 g, 2.01 mmol) was added to a Schlenk flask containing 40 mL of THF and a magnetic stir bar. This was stirred at room temperature under N_2 . To this mixture, triethylamine (0.29 mL, 2.08 mmol) and *i*PrOH (0.16 mL, 2.08 mmol) were added. The reaction was allowed to stir at room temperature for 16 h. The THF was removed in vacuo. The resulting product was then extracted with hexanes and filtered through a medium porosity glass fritted glass filter. The hexane was removed, leaving a orange product (0.241 g, 44%). ^1H NMR (400 MHz, C_6D_6 , 298 K): δ 1.03 (d, 6H, $\text{CH}(\text{CH}_3)_2$), δ 4.48 (sept, 1H, $J = 6$ Hz, $\text{CH}(\text{CH}_3)_2$), δ 5.88 (s, 10H, C_5H_5); ^{13}C NMR (100 MHz, C_6D_6 , 298 K): δ 25.5 (s, $\text{CH}(\text{CH}_3)_2$), δ 84.1 (s, $\text{CH}(\text{CH}_3)_2$), 116.5 (s, C_5H_5).

Cp₂TiCl(OtBu) (3). Cp₂TiCl₂ (0.249 g, 1.00 mmol), K[OtBu] (0.113 g, 1.01 mmol), and 50 6 mm ball bearings were added to a grinding jar. The jar was sealed under an inert atmosphere and the reaction was ground at 600 rpm for 15 min. Upon completion, the jar was opened under inert atmosphere to reveal an orange solid which was then extracted with minimal hexanes and filtered through a fritted glass filter. The resulting orange filtrate was then dried, resulting in an orange solid (0.181 g, 63%). ¹H NMR (400 MHz, C₆D₆, 298 K): δ 1.12 (s, 9H, OC(CH₃)₃), δ 5.94 (s, 10H, C₅H₅); ¹³C NMR (100 MHz, C₆D₆, 298 K): δ 31.3 (s, CH₃), δ 87.8 (s OC(CH₃)₃), 116.6 (s, C₅H₅). Anal. Calcd for C₁₄H₁₉ClOTi: C, 58.7; H 6.7; Ti 16.7; Cl 12.4. Found: C, 58.5; H, 6.6; Ti, 16.9; Cl, 10.45.

Cp₂TiBr(OtBu) (4). TiBr₄ (0.457 g, 1.24 mmol), Li[OtBu] (0.101 g, 1.26 mmol), LiCp (0.177 g, 2.46 mmol), and 50 6 mm ball bearings were added to a grinding jar. The jar was sealed under inert atmosphere and the reaction was ground at 600 rpm for 15 min. Upon completion, the jar was opened under inert atmosphere to reveal an orange solid which was then extracted with minimal hexanes and filtered through a fritted glass filter. The resulting filtrate was then dried, resulting in an orange solid (0.214 g, 52%). ¹H NMR (400 MHz, C₆D₆, 298 K): δ 1.10 (s, 9H OC(CH₃)₃), δ 5.92 (s, 10H, C₅H₅). ¹³C (100 MHz, C₆D₆, 298K): δ 31.2 (s, CH(CH₃)₂), δ 88.4(s, CH(CH₃)₂), 116.2 (s, C₅H₅).

CpTiBr₂(OtBu) (5). TiBr₄ (0.576 g, 1.57 mmol), Li[OtBu] (0.127 g, 1.59 mmol), LiCp (0.114 g, 1.58 mmol) and 50 3 mm ball bearings were added to a grinding jar. The jar was sealed under inert atmosphere and the reaction was ground at 600 rpm for 15 min. Upon completion, the jar was opened under inert atmosphere to reveal a yellow-brown solid which was then extracted with minimal hexanes and filtered through a fritted glass filter. The

resulting yellow filtrate was then dried, resulting in a yellow solid (0.241 g, 44%). ^1H NMR (400 MHz, C_6D_6 , 298 K): δ 1.14 (s, 9H C_4H_9), δ 6.16 (s, 10H, C_5H_5); ^{13}C NMR (100 MHz, C_6D_6 , 298 K): δ 30.1 (s, CH_3), δ 92.6 (s $\text{OC}(\text{CH}_3)_3$), 118.0 (s, C_5H_5). Anal. Calcd for $\text{C}_9\text{H}_{14}\text{Br}_2\text{OTi}$: C, 31.25; H 4.08; Found: C, 31.42; H, 3.96.

CpTiBr(OtBu)₂ (6). TiBr_4 (0.3821 g, 1.04 mmol), $\text{Li}[\text{OtBu}]$ (0.1674 g, 2.09 mmol), LiCp (0.747 g, 1.04 mmol) and 50 6 mm ball bearings were added to a grinding jar. The jar was sealed under inert atmosphere and the reaction was ground at 600 rpm for 15 min. Upon completion, the jar was opened under inert atmosphere to reveal an orange paste that was then extracted with minimal hexanes and filtered through a fritted glass filter. The resulting yellow filtrate was then placed under vacuum, resulting in an orange oil (0.2167 g, 62%). ^1H NMR (400 MHz, C_6D_6 , 298 K): δ 1.19 (s, 18H, C_4H_9), δ 6.22 (s, 5H, C_5H_5); ^{13}C (100 MHz, C_6D_6 , 298K); δ 31.8 (s, $\text{CH}(\text{CH}_3)_2$), δ 86.8 (s, $\text{CH}(\text{CH}_3)_2$), 115.0 (s, C_5H_5).

CHAPTER 6

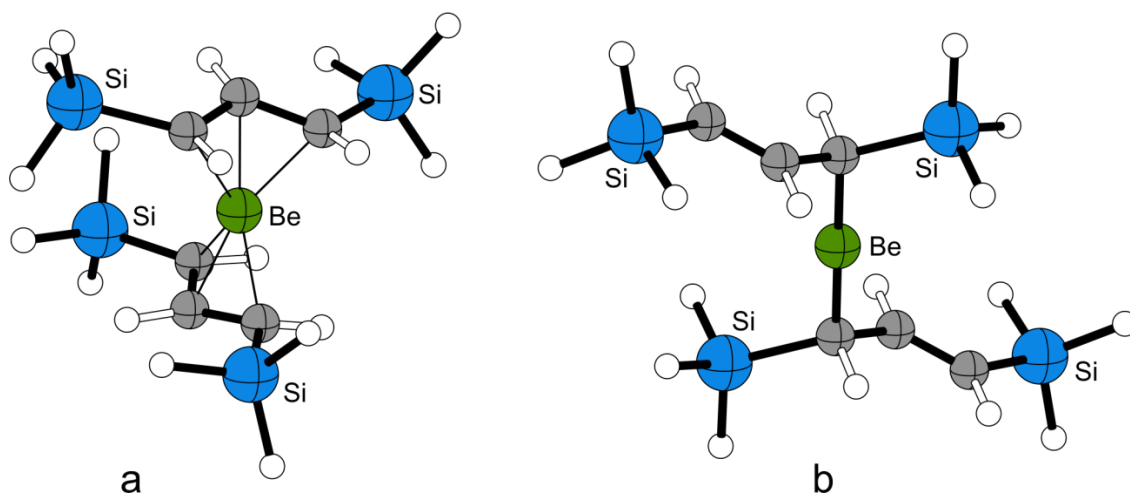
Symmetric Assembly of a Sterically Encumbered Allyl Complex: Mechanochemical and Solution Synthesis of the Tris(allyl)beryllate, $K[\text{BeA}'_3]$ ($\text{A}' = 1,3\text{-(SiMe}_3)_2\text{C}_3\text{H}_3$)

6.1 Introduction

The physical and chemical properties of first-row elements often differ appreciably from their second-row and heavier counterparts; for the group 2 metals, the outlier (“black sheep”²¹¹) designation belongs to beryllium. To a considerably greater extent than its heavier congeners, even magnesium, the small size of the Be^{2+} cation (0.27 Å for CN = 4; cf. 0.57 Å for Mg^{2+})²¹² and its corresponding high charge/size ratio ensures its bonds will be strongly polarized and possess substantial covalent character. Not surprisingly, beryllium compounds with the same ligand sets commonly have different structures from those of the other, more electropositive alkaline earth (Ae) metals. The bis(trimethylsilyl)amides of Mg–Ba, for example, have a common dimeric bridged structure, $[\text{Ae}(\text{N}(\text{SiMe}_3)(\mu\text{-N}(\text{SiMe}_3)_2)_2)]_2$,²¹³ whereas that of beryllium is a 2-coordinate monomer.²¹ Similarly, the bis(cyclopentadienyl) complex Cp_2Be has an $\eta^1, \eta^5\text{-Cp}$ structure²¹⁴ that is unlike that of the heavier metallocenes.²¹⁵ Investigation of these differences, and indeed research with all beryllium compounds, has traditionally been limited because of concerns about toxicity,²¹⁶ but that has not prevented its compounds from serving as useful benchmarks of the steric and electronic consequences of crowded metal environments.²¹⁷⁻²²⁰

One of these consequences is the relative stability of η^1 - vs. η^3 -bonded allyl ligands in compounds of highly electropositive metals. We found some time ago that the bulky allyl

[A']⁻ (A' = [1,3-(SiMe₃)₂C₃H₃]) can be used to form the ether adduct BeA'₂·OEt₂, which displays η¹-bonded A' ligands in the solid state.²²¹ The compound is fluxional in solution, and exhibits symmetric, “π-type” bonding in its NMR spectra (e.g., only one peak is observed for the SiMe₃ groups). Density functional theory (DFT) calculations suggested that a base-free Be(C₃H₃E₂)₂ (E = H, SiH₃) complex would be more slightly more stable with delocalized, π-type allyls than with monodentate, sigma-bonded ligands (Scheme 1). If so, beryllium allyls would join those of magnesium, in which monodentate allyl ligands are uniformly found in complexes that are ether-solvated,²²² but that in the absence of ethers, cation-π interactions with the metal can create “slipped-π” bonding.²²³



Scheme 1. Optimized geometries of Be(1,3-(SiH₃)₂C₃H₃)₂. At the B3PW91/aug-cc-pVDZ level, the π-bound structure (a) is 4.0 kcal mol⁻¹ lower in energy (ΔG°) than the σ-bound geometry (b).²²¹

The coordinated ether in BeA'₂·OEt₂ proved impossible to remove without destroying the complex,²²¹ and thus we investigated mechanochemical methods of synthesis as a means to bypass the use of ethereal solvents.¹³⁷ As detailed below, an unsolvated neutral complex

was not isolated via this route, and the beryllate anion that was produced instead has structural parallels with previously described -ate complexes of Zn²²⁴ and Sn.²²⁵ In all of these species, the alkali metal counterion, usually K⁺ but sometimes Na⁺ and Li⁺, appears to play a critical role in the assembly of the symmetric complexes.

6.2 Results and Discussion

Solid-state synthesis. The reaction of BeCl₂ and K[A[∧]] was conducted mechanochemically with a planetary ball mill, followed by an extraction with hexanes. Initial investigations used 2:1 molar ratios of BeCl₂ and K[A[∧]], based on the assumption that the product formed would be BeA[∧]₂ (eq. 1). Although the reagents are off-white (K[A[∧]]) and white (BeCl₂), the ground reaction mixture (15 min/600 rpm) is orange. Extraction with hexanes, followed by filtration, yielded an orange filtrate and ultimately a dark orange solid (**1**) on drying.

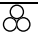





A single crystal analysis (described below) revealed that **1** is the potassium tris(allyl)beryllate, K[BeA[∧]₃]. This forms in spite of the fact that the 2:1 ratio of reagents used (eq. 1) is not optimum for its production. As detailed below, conducting the reaction with 1:1 and 3:1 molar ratios of K[A[∧]] and BeCl₂ still yields **1** as the sole hexane-extractable product. It is possible that the excess halide is captured in the form of polyhalide anions such as [BeCl₄]²⁻ or [Be₂Cl₆]²⁻,²²⁶ although these have not been definitively identified.

Synthesis in solution. The reaction of K[A[∧]] and BeCl₂ was also examined in solution, using diethyl ether, hexanes, and THF. These results are summarized in Table 1.

Previous reactions with diethyl ether involved stirring for 2 hr at room temperature, which formed $\text{BeA}'_2 \cdot \text{OEt}_2$ from a 2:1 reaction (#5); Schlenk equilibrium was observed in a 1:1 mixture that was allowed to react for one hour (#4). When the 2:1 reaction in Et_2O is allowed to proceed for 16 hr, however, the formation of **1** is observed (#6) exclusively. Reaction in hexanes mimics the solid-state reactions, in that **1** is the exclusively detected organoberyllium product from a 1:1 reaction after 1 hr (#7). Longer reactions and higher ratios of $\text{K}[\text{A}']$ to BeCl_2 (e.g., 3:1) do not change this outcome. THF reactions were performed to compare another coordinating ethereal solvent to the previously explored diethyl ether reactions. These reactions (#8 and 9) showed evidence of Schlenk equilibrium with the unisolated THF adducts. These were identified through beryllium NMR but further isolation was not completed. The formation of **1** is observed in THF (#10) exclusively.

Table 10. Summary of $\text{K}[\text{A}']$ and BeCl_2 reactions; amounts of reagents given as molar ratios

No.	$\text{K}[\text{A}']:\text{BeCl}_2$	Medium ^[a]	Time	Organoberyllium product(s)	Yield (%) ^[b]
1	1:1		15 min	$\text{K}[\text{BeA}'_3]$	97
2	2:1		15 min	$\text{K}[\text{BeA}'_3]$	21
3	3:1		15 min	$\text{K}[\text{BeA}'_3]$	25
4	1:1	Et_2O	1 hr	$2\text{A}'\text{BeCl} \rightleftharpoons \text{BeA}'_2 + \text{BeCl}$	n/a ^[c,d]
5	2:1	Et_2O	2 hr	$\text{BeA}'_2 \cdot \text{OEt}_2$	77 ^[c]
6	2:1	Et_2O	16 hr	$\text{K}[\text{BeA}'_3]$	98
7	1:1	hexanes	1 hr	$\text{K}[\text{BeA}'_3]$	24
8	1:1	THF	16 hr	$2\text{A}'\text{BeCl} \rightleftharpoons \text{BeA}'_2 + \text{BeCl}$	n/a ^[d]
9	2:1	THF	1 hr	$2\text{A}'\text{BeCl} \rightleftharpoons \text{BeA}'_2 + \text{BeCl}$	n/a ^[d]
10	3:1	THF	16 hr	$\text{K}[\text{BeA}'_3]$	42

^[a]  = ball milling at 600 rpm. The symbol for mechanical milling has been proposed in ref. ¹³⁷. ^[b] Unrecrystallized; limiting reagent taken into account. ^[c] Ref. ²²¹ ^[d] Products were observed with ⁹Be NMR, and were not isolated.

NMR spectra. The ¹H NMR spectrum of **1** displays resonances typical of a π -bound A' ligand, with a triplet representing $\text{H}_{(\beta)}$, a doublet representing the equivalent $\text{H}_{(\omega)}$ and $\text{H}_{(\gamma)}$,

and a singlet for the two equivalent TMS groups. The appearance of such a symmetric spectrum even when σ -bound ligands are expected is consistent with a high degree of fluxionality, as was also observed in the σ -bound complex $\text{BeA}'_2\cdot(\text{Et}_2\text{O})$ ²²¹. The triplet resonance of the allyl ligands, at δ 7.00, is shifted downfield from that of $\text{BeA}'_2\cdot(\text{Et}_2\text{O})$ (δ 6.53); the doublet resonance at δ 3.21 is slightly upfield (cf. δ 3.33 in $\text{BeA}'_2\cdot(\text{Et}_2\text{O})$). The NMR chemical shifts for **1** are in line with those observed for other $\text{M}[\text{M}'\text{A}'_3]$ complexes (Table 2). In particular, the NMR shifts of the allyl ligands are sensitive both to the identity of the central divalent metal and to that of alkali metal counterion, evidence that the compounds exist as contact ion pairs in solution. Compound **1** and $\text{K}[\text{ZnA}'_3]$ share the greatest similarities, consistent with their having the same counterion (K^+) and central metals of similar electronegativity (χ Be (1.57); Zn (1.65)).⁶⁴

John and co-workers have demonstrated that ^9Be NMR chemical shift values can be diagnostic for coordination numbers in solution.²²⁷ Typically, organoberyllium complexes with low formal coordination numbers, such as $\text{BeMe}_2\cdot\text{Et}_2\text{O}$ (coordination number 3, $\delta = 20.8$ ppm in Et_2O), are observed well downfield of 0 ppm. $[\text{BeA}'_2(\text{Et}_2\text{O})]$ has a ^9Be chemical shift of $\delta = 18.2$ ppm, which is consistent with a three-coordinate geometry in solution²²¹. The ^9Be of **1** is at $\delta = 22.8$ ppm, which to our knowledge is the most positive shift yet reported for a 3-coordinate species.²²⁸ DFT methods were used to predict the ^9Be chemical shift value of **1** (B3LYP-D3/6-311+G(2d,p)//B3LYP-D3/6-31G(d)). It was calculated at $\delta = 25.9$ ppm, in reasonable agreement with the observed value (referenced to $[\text{Be}(\text{OH}_2)_4]^{2+}$ with an isotropic shielding constant of 108.98 ppm).

Table 11 ^1H NMR shifts (ppm) and bond distances in $\text{M}[\text{M}'\text{A}'_3]$ complexes.

Complex	$\delta \text{H}_{(\alpha)} / \text{H}_{(\gamma)}$	$\delta \text{H}_{(\beta)}$	δSiMe_3	M–C (σ) Å	M'...C(olefin) Å	Ref.
Li[ZnA' ₃]	6.46	3.50	0.15	2.117(3) ^[b]	2.745(4), 2.268(3) ^[b]	224
Na[ZnA' ₃]	7.59	4.00	0.16	2.103(3)	2.857(3), 2.567(3)	224
K[BeA' ₃]	7.00	3.21	0.22	1.805(10)	3.153(7), 2.940(7)	this work
K[ZnA' ₃]	7.05	3.42	0.23	2.068(4)	3.205(3), 2.945(3)	224
K(thf)[SnA' ₃]	6.43	4.42	0.42, 0.23 ^[a]	2.344(7)	3.201(7), 3.164(8), 3.065(8)	225

^[a]Two resonances are observed for the SiMe₃ groups, as the A' ligands are not fluxional. ^[b]Distance(s) affected by crystallographic disorder.

Crystal Structure of K[BeA'₃]. The structure of **1** was determined from single crystal X-ray diffraction; Appendix # contains crystal and refinement information. In the solid state, **1** exhibits approximate C_3 -symmetry, with σ -bound A' ligands and a potassium cation engaging in cation- π interactions with the three double bonds of the allyls. It is isostructural with the previously reported $\text{M}[\text{ZnA}'_3]$ (M = Li, Na, K) and $\text{K}[\text{SnA}'_3]$ complexes.²²⁴⁻²²⁵ The beryllium center is in a nearly planar trigonal environment (sum of C-Be-C' angles = 357.7°) (Figure 26).

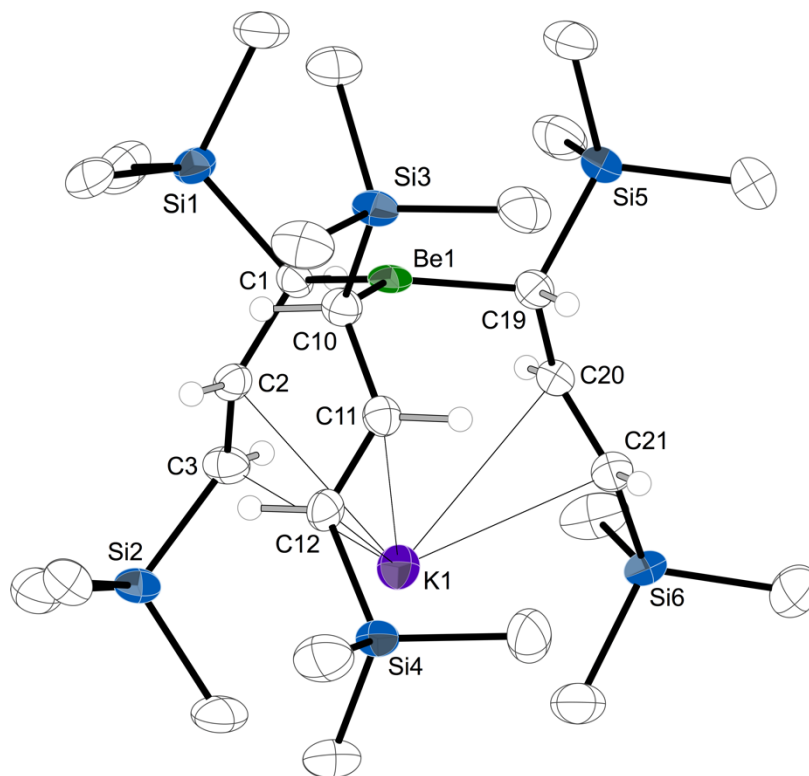


Figure 26. Thermal ellipsoid plot of KBeA_3

Thermal ellipsoid plot of **1**, illustrating the numbering scheme used in the text. Ellipsoids are drawn at the 50% level, and for clarity, hydrogen atoms have been removed from the trimethylsilyl groups. Selected bond distances (Å) and angles (deg): Be1–C1, 1.795(6); Be1–C10, 1.810(6); Be1–C19, 1.811(6); C(2)–C(3), 1.351(5); C(11)–C(12), 1.350(5); C(20)–C(21), 1.358(5); K(1)–C(2), 3.138(4); K(1)–C(3), 2.940(4); K(1)–C(11), 3.206(4); K(1)–C(12), 2.943(4); K(1)–C(20), 3.114(4); K(1)–C(21), 2.938(4); C(1)–Be(1)–C(10), 119.1(3); C(1)–Be(1)–C(19), 119.0(3); C(10)–Be(1)–C(19), 119.4(3). Crystal structure originally obtained by Nicholas R. Rightmire.

The average Be–C distance of 1.805(10) Å has few direct points of comparison with other molecules, as **1** is only the second crystallographically characterized $[\text{BeR}_3]^-$ complex, the other being lithium tri-*tert*-butylberyllate.²²⁹ The latter's Be center, like that in **1**, is in a nearly perfectly planar trigonal environment (sum of C–Be–C angles = 359.9°). In the solid state, however, tri-*tert*-butylberyllate is a dimer, $[\text{Li}\{\text{Be}(t\text{-C}_4\text{H}_9)_3\}]_2$, with some corresponding distortions in the Be–C bond lengths;²²⁹ Be–C distances range from 1.812(4) Å to 1.864(4) Å,

averaging to 1.843(6) Å. The Be–C length in **1** is indistinguishable from the Be–C_{carbene} length of 1.807(4) Å in the [Ph₂Be(IPr)] (IPr = 1,3-bis(2,6-di-isopropylphenyl)-imidazol-2-ylidene) complex, which also has a 3-coordinate Be center.²³⁰ The anionic methyl groups in [Ph₂Be(IPr)] are at a noticeably shorter distance, however (1.751(6) Å, ave.). A similar relationship between the Be–C_{carbene} and Be–CH₃ bond lengths exists in the related [Me₂Be(IPr)]²³¹ and [Me₂Be(IMes)] (IMes = *N,N'*-bis(2,4,6-trimethylphenyl)imidazol-1-ylidene) complexes.²¹¹ A comparison of the Be–C length in **1** could also be made with the Be–C distance of 1.84 Å in lithium tetramethylberyllate, Li₂[BeMe₄], although the bond distance would be expected to be slightly longer in the latter owing to the higher coordination number of beryllium and the greater negative charge.²³²

The C–C and C=C bonds in the alkyl groups in **1** are localized at 1.475(5) Å and 1.353(9) Å, respectively. The K⁺...C(olefin) contacts average 3.153(7) Å and 2.940(7) Å to the carbon atoms β (C2, C11, C20) and γ (C3, C12, C21) to the beryllium atom, respectively. These distances are comparable to, but slightly shorter than, the range of K⁺...C contacts found in the related zincate structure (3.205(3) Å and 2.945(3) Å, respectively), which reflects the shorter M–C_(α) bonds in **1**. The distance between Be and K (3.59 Å) is long enough to rule out significant metal-metal interactions.

Computational investigations. It has previously been suggested that the occurrence of C₃-symmetric M[M'A₃L] (M' = Zn, M = Li, Na, K; M' = Sn, M = K; L = thf) complexes is the result of a templating effect of the associated alkali metal counterion.¹³⁸ The rationale for this proposal is that the neutral MA₃ (M = As, Sb, Bi) complexes always occur in two diastereomeric forms, with *R,R,R* (equivalently, *S,S,S*) and *R,R,S* (or *S,S,R*) arrangements of

the allyl ligands around the central element. The anionic $[\text{MA}_3']^-$ complexes, in contrast, are always found in the C_3 symmetric R,R,R (or S,S,S) configuration, and it is not unreasonable to assume that the counterion is responsible for the difference.

A DFT investigation was undertaken to explore the possible origins of this effect. The geometry of the free $[\text{BeA}'_3]^-$ anion was optimized with calculations employing the dispersion-corrected APF-D functional.²⁰⁵ Three conformations were examined: the C_3 -symmetric form (S,S,S) found in the X-ray crystal structure of **1**, a related S,S,S form with one A' ligand rotated antiparallel to the other two (C_1 symmetry), and a R,R,S form, also with one ligand antiparallel to the other two, derived from the structure of the neutral AlA'_3 complex (Figure 27).¹⁸⁹

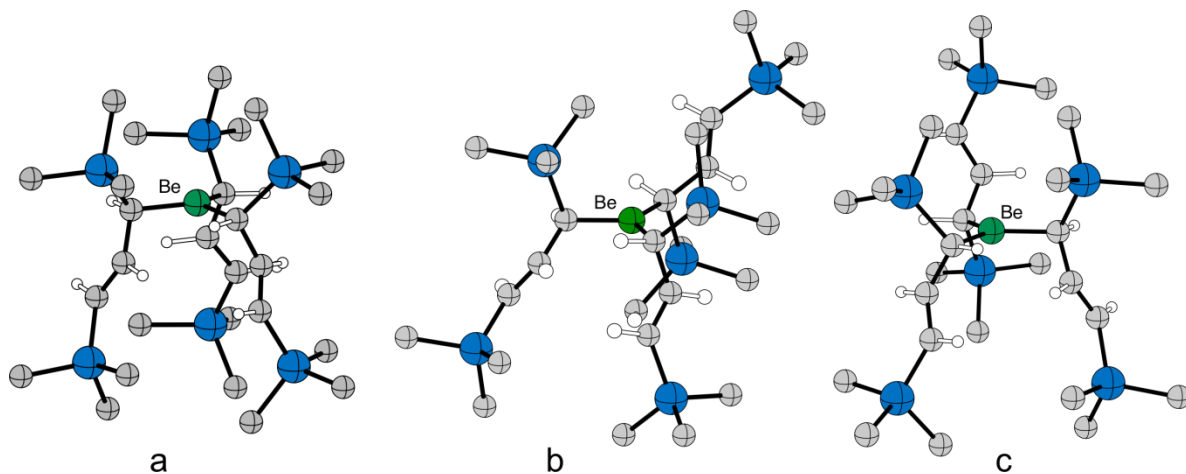


Figure 27. Geometry optimized structures of the $[\text{BeA}'_3]^-$ anions

Geometry optimized structures of the $[\text{BeA}'_3]^-$ anions: (a) as found in the crystal structure of **1**; (b) Related R,R,R form with one A' ligand rotated (C_1 symmetry); R,R,S form derived from the structure of AlA'_3 .

Not surprisingly, the calculated structures possess similar average Be–C bond lengths, ranging from 1.782 Å (the C_3 -symmetric form (a)) to 1.788 Å (for the rotated R,R,R form (b)). Energetically, the R,R,S form is the most stable; the rotated R,R,R form is 10.1 kJ mol⁻¹ higher

in energy (ΔG°), and the C_3 -symmetric form is the highest (20.3 kJ mol⁻¹ in ΔG°).²³³ The origin of these energy differences is not immediately obvious, but it may be related to the relative amounts of interligand congestion present. The low energy R,R,S form, for example, has no Me...Me' contacts less than 4.0 Å, the sum of the van der Waals radii.⁶⁴ In contrast, the C_3 symmetric form has multiple contacts between methyl groups of less than 4.0 Å, including two as short as 3.76 Å. At this level of theory, the energetics of the free anions do not provide a rationale for the exclusive formation of the R,R,R form.

Not surprisingly, incorporation of the K⁺ ion into the complex alters the relative stability of the species. The optimized geometries of the C_3 -symmetric K[BeA₃'] found in the X-ray crystal structure of **1** and a related R,R,S form were calculated similarly to the isolated anions, and are depicted in Figure 28.

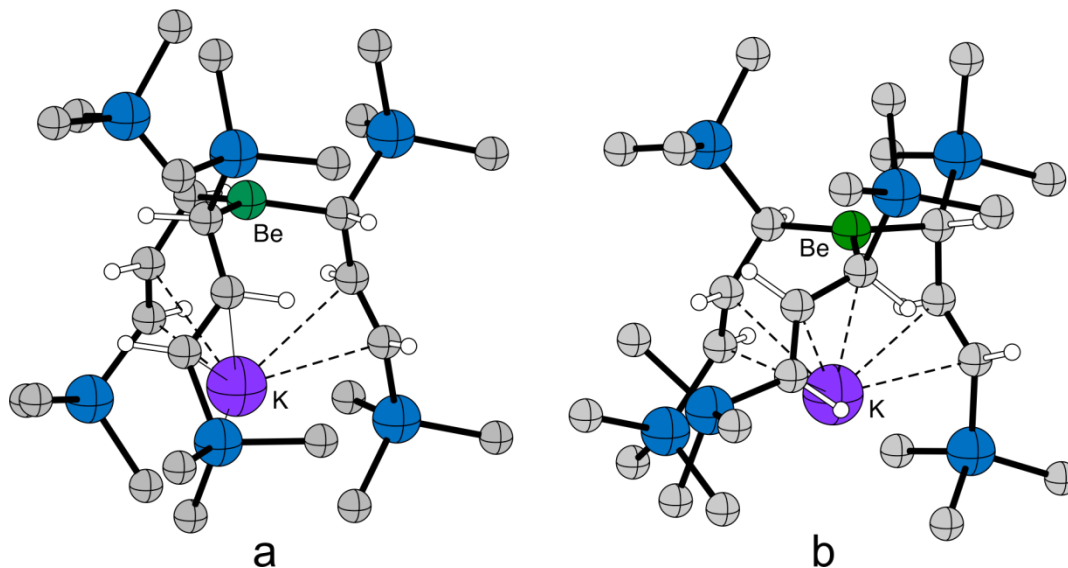


Figure 28. Geometry optimized structures of the K[BeA₃'] complex: (a) as found in the crystal structure of **1**; (b) Related R,R,S form.

The C_3 -symmetric form is 6.1 kJ mol^{-1} more stable than the R,R,S form. This is not a consequence of closer $K^+ \cdots (C=C)$ distances, which are nearly the same (avg. 3.91 \AA in the C_3 form; 2.86 \AA in the R,R,S arrangement). The asymmetric arrangement of the ligands in the R,R,S form does lead to closer interligand $C \cdots C$ contacts in the allyl frameworks, however, as small as 3.37 \AA , whereas there are no similar contacts less than 3.78 \AA in the C_3 form. The somewhat greater stability of the C_3 form, possibly coupled with greater ease of crystal packing, may contribute to the exclusive appearance of that form in the crystal structure. It is likely that a similar analysis holds for the isostructural Zn and Sn complexes.

The failure to produce an unsolvated BeA'_2 in the absence of a coordinating solvent (i.e., either mechanochemically or in hexanes) was also examined computationally with the aid of the SolidG program.⁶³ Both $BeA'_2 \cdot Et_2O$ and **1** are found to have coordination sphere coverage (G_{complex}) above 90% (i.e., 97.0% (Figure 29a) and 92.6% (Figure 29b), respectively). Although the coverage of the metal center in the hypothetical BeA'_2 varies somewhat with the angle between the ligands, the minimum energy position depicted in Figure 29c (C_2 symmetry) has only 78.7% coverage. It is not unreasonable to assume that a monomeric BeA'_2 may be too coordinately unsaturated to be readily isolable, and will bind an ethereal solvent molecule, or if that is not available, an additional A' ligand, counterbalanced with a K^+ ion.

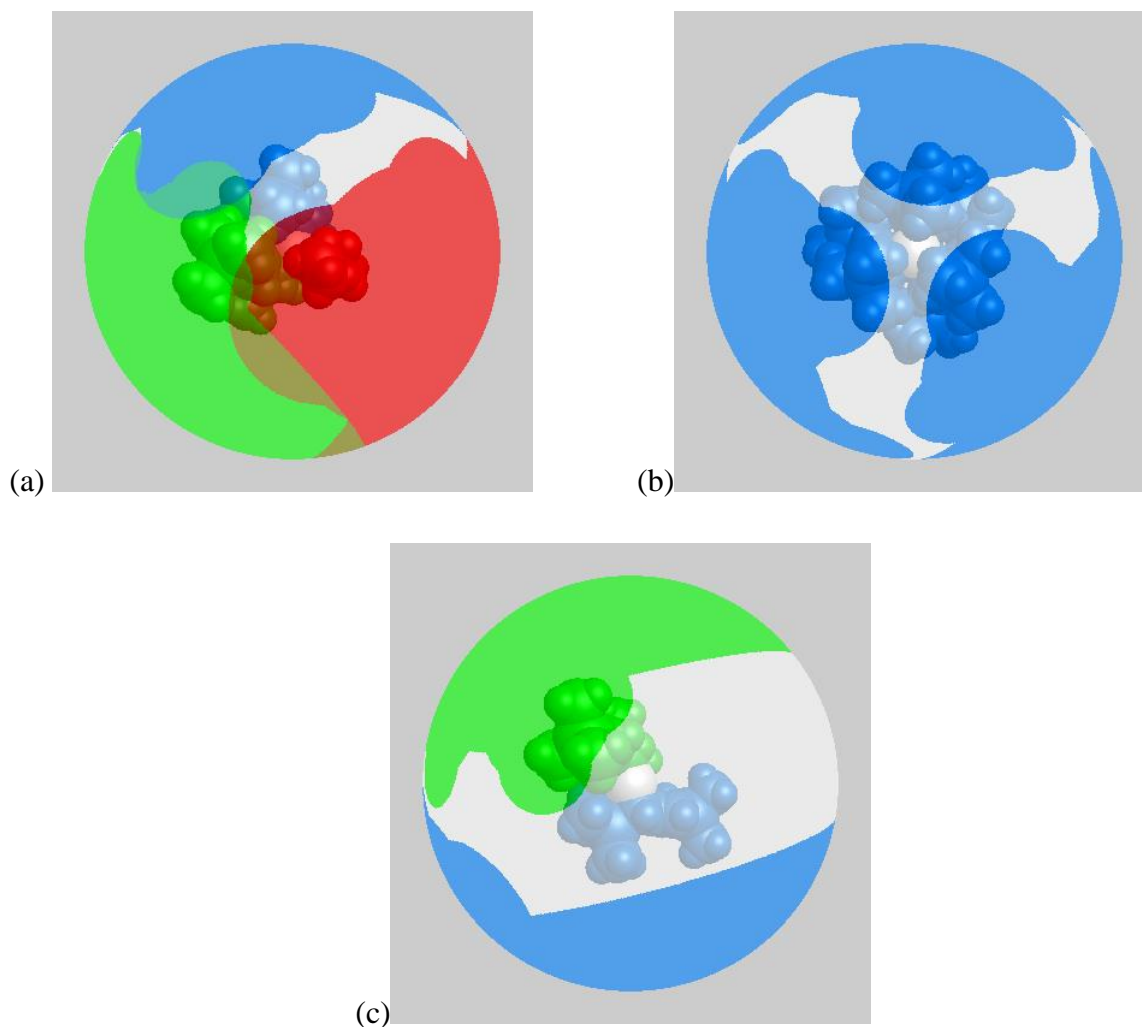


Figure 29. Visualization of the extent of coordination sphere coverage (G_{complex}) of $\text{BeA}'_2 \cdot \text{Et}_2\text{O}$, BeA'_2 , and KBeA'_3

Visualization of the extent of coordination sphere coverage (G_{complex}) of: (a) $\text{BeA}'_2 \cdot \text{Et}_2\text{O}$ (the coverage from the two allyls are assigned blue and green; that from the ether is in red); (b) **1** (all three allyls are in blue); and (c) BeA'_2 , using optimized coordinates (APF-D/6-311G(2d) (Be); 6-31G(d) (other atoms)) and the program Solid-G⁶³. The G_{complex} value takes into account the net coverage; regions of the coordination sphere where the projections of the ligands overlap are counted only once.

6.3 Conclusions

The generation of products from reagents that are not in the optimum stoichiometric ratio is a known feature of some Group 2 reactions,²³⁴⁻²³⁵ a testament to the role that kinetic factors play in s-block chemistry. It is perhaps not surprising that when mechanochemical activation is used with alkaline earth reagents, a nonstoichiometric product such as the organoberyllate **1** is formed, as grinding and milling environments are often far from equilibrium.¹⁹⁶⁻¹⁹⁹ Yet the fact that **1** is also generated in hexanes indicates how non-ethereal synthesis can reveal features of reactions that are obscured when they are conducted in coordinating solvents. It is now apparent that the production of the previously described $\text{BeA}'_2 \cdot \text{Et}_2\text{O}$, which was the expected complex from a 2:1 reaction of $\text{K}[\text{A}'^-]$ and BeCl_2 in diethyl ether,²²¹ actually depends critically on the presence of the solvent to prevent further reaction of the beryllium center with an additional A'^- ligand. This also appears to be the case for THF which was briefly investigated. Without such solvent support, whether conducted mechanochemically or in hexanes, the reaction between $\text{K}[\text{A}'^-]$ and BeCl_2 rapidly forms the kinetic product **1**.

Parallels of the beryllium chemistry to the related tris(allyl) '-ate' complexes of Zn and Sn are instructive, although they cannot be pushed too far. All the $[\text{MA}_3]^-$ species possess approximate C_3 symmetry, and it is likely that the associated alkali metal cation is intimately involved in templating their constructions. The formation of the zinc species $\text{K}[\text{ZnA}'_3]$ is also similar to that of **1** in that it is formed from the reaction of 2 equiv of $\text{K}[\text{A}'^-]$ and ZnCl_2 , i.e., in a non-stoichiometric reaction.²²⁴ Yet both it and $\text{K}(\text{thf})[\text{SnA}'_3]$ are synthesized in THF, so it is clear that the driving force for '-ate' formation over that of the

neutral (Zn,Sn)A'₂ species is greater than that for **1**.²³⁶ This may reflect the somewhat lower covalency of Be–C versus Zn–C and Sn–C bonds, and the greater robustness of M²⁺ ← :OR₂ interactions with beryllium.

6.4 Experimental

General Considerations. All syntheses were conducted under rigorous exclusion of air and moisture using Schlenk line and glovebox techniques. NOTE: *Beryllium salts should be handled with appropriate protective equipment.* After grinding was completed, the jars were opened according to glovebox procedures to protect the compounds and to prevent exposure to dust.²³⁷ Proton (¹H) and carbon (¹³C) spectra were obtained on an Advance AV-400 MHz spectrometer, and were referenced to residual resonances of C₆D₆. Beryllium (⁹Be) spectra were obtained on a Bruker DRX-500 at 70.2 MHz, and were referenced to BeSO₄(aq). Combustion analysis was performed by ALS Environmental, Tucson, AZ.

Materials. Beryllium chloride was purchased from Strem, stored under an N₂ atmosphere and used as received. The K[A'] (A' = 1,3-(SiMe₃)₂C₃H₃) reagent was synthesized as previously described.²³⁸⁻²³⁹ Toluene, hexanes, and diethyl ether were distilled under nitrogen from potassium benzophenone ketyl.¹⁰⁷ Deuterated benzene (C₆D₆) was distilled from Na/K (22/78) alloy prior to use. Stainless steel (440 grade) ball bearings (6 mm) were thoroughly cleaned with hexanes and acetone prior to use. Planetary milling was performed with a Retsch model PM100 mill, 50 mL stainless steel grinding jar type C, and safety clamp for air-sensitive grinding.

Mechanochemical synthesis of K[BeA'₃] (1). Solid BeCl₂ (56.7 mg, 0.71 mmol) and K[A'] (319 mg, 1.42 mmol) were added to a 50 mL stainless steel grinding jar (type C). The

jar was charged with stainless steel ball bearings (6 mm dia, 50 count) and closed tightly with the appropriate safety closer device under an N₂ atmosphere. The reagents were milled for 15 min at 600 rpm, resulting in a light orange solid. The product was extracted under inert atmosphere with minimal hexanes (< 100 mL) and filtered through a medium porosity ground glass frit, providing a dark orange filtrate. Drying under vacuum yielded a dark orange solid (61.5 mg, 21% yield of K[BeA'₃]) which was recrystallized by the slow evaporation of toluene over one month to provide dark orange-brown crystals of **1** suitable for single crystal X-ray diffraction. For a 3:1 K[A']:BeCl₂ reaction, 812 mg (3.62 mmol) K[A'] and 95.2 mg (1.19 mmol) BeCl₂ were added to a grinding jar. After extraction, 183 mg (25% yield) of orange solid was collected. Anal. Calcd (%) for C₂₇H₆₃BeKSi₆: C, 53.65; H, 10.51; Be, 1.49. Found: C, 52.09; H, 9.79; Be, 1.04. The values are somewhat low, possibly from the high air-sensitivity of the compound, but the C:H molar ratio is 2.34:1.00, close to the expected 2.33:1.00. ¹H NMR (400 MHz, C₆D₆, 298K): δ 0.22 (s, 54H, SiMe₃); 3.21 (d, 6H, J = 13.12 Hz, H_(α,γ)); 7.00 (t, 3H, J₁ = 15.6 Hz, H_(β)). ¹³C NMR (100 MHz, C₆D₆, 298K): δ 1.02 (s, SiMe₃); 70.71 (s, C_(α,γ)); 166.09 (s, C_(β)). ⁹Be NMR (70.2 MHz, C₆D₆, 298K); δ 22.8 (s).

General procedures for reactions with solvents: Reactions were performed for either 1 or 16 hr, and were run under inert atmosphere at room temperature. The ratio of K[A'] and BeCl₂ was varied such that the reactions of emphasis were 1:1, 2:1, and 3:1. A general reaction involved dissolving the beryllium chloride (ca. 0.1 g) in the solvent of choice (Et₂O, hexanes, or THF); to this solution solid K[A'] was added slowly and solvent was used to quantitatively transfer all material. Upon mixing the solution was allowed to stir for the given time. In the case of Et₂O and THF, the solvent was removed in vacuo, and the resulting material was extracted with hexanes, filtered through a medium porosity glass frit, then dried

in vacuo. In the case of reaction in hexanes, the reaction mixture was filtered through a medium porosity fritted glass filter, and the hexane was removed in vacuo. The resulting product in all cases was then analyzed with proton and beryllium NMR. NMR for THF reactions 8, 9, and 10 can be seen in appendix.

Procedures for X-ray crystallography. A crystal (0.20 x 0.20 x 0.08 mm³) was placed onto the tip of a thin glass optical fiber and mounted on a Bruker SMART APEX II CCD platform diffractometer for a data collection at 100.0(5) K¹⁶⁸. A preliminary set of cell constants and an orientation matrix were calculated from reflections harvested from three orthogonal wedges of reciprocal space. The full data collection was carried out using MoK α radiation (graphite monochromator) with a frame time of 60 seconds and a detector distance of 4.02 cm. A randomly oriented region of reciprocal space was surveyed: four major sections of frames were collected with 0.50° steps in ω at four different ϕ settings and a detector position of -38° in 2θ . The intensity data were corrected for absorption.²⁴⁰ Final cell constants were calculated from the *xyz* centroids of 2886 strong reflections from the actual data collection after integration.²⁴¹ See Table 3 for additional crystal and refinement information.

The structure was solved using SIR2011²⁴² and refined using SHELXL-2014/7.¹⁷¹ The space group $P\bar{1}$ was determined based on intensity statistics. A direct-methods solution was calculated which provided most non-hydrogen atoms from the E-map. Full-matrix least squares/difference Fourier cycles were performed which located the remaining non-hydrogen atoms. All non-hydrogen atoms were refined with anisotropic displacement parameters. The allylic hydrogen atoms were found from the difference Fourier map and refined freely. All

other hydrogen atoms were placed in ideal positions and refined as riding atoms with relative isotropic displacement parameters.

General Procedures for Calculations. All calculations were performed with the Gaussian 09W suite of programs;¹¹¹ an ultrafine grid was used for all cases (Gaussian keyword: int=ultrafine). Each conformation of the $[\text{BeA}'_3]^-$ complexes was studied with the APF-D functional, a global hybrid with 23% exact exchange.²⁰⁵ The 6-31+G(d) basis set was used for C,H,Si; the 6-311+G(2d) basis was used for Be. For the neutral $\text{K}[\text{BeA}'_3]$ conformations, the APF-D functional was used with the 6-31G(d) basis set for C,H,Si; 6-311G(2d) was used for Be and K. The nature of the stationary points was determined with analytical frequency calculations; all of these optimized geometries were found to be minima ($N_{\text{imag}} = 0$). For the SolidG calculations, the structures were preoptimized with the APF-D/6-311G(2d) (Be,K); 6-31G(d) (C,H,Si) protocol.

(This work was adapted from: Boyde, N. C., et al. *Inorganics*, **2017**, 5(2) 36)

Section A1.

Crystallographic, computational, spectral data of Group 15 M[N(SiMe₃)₂]₃

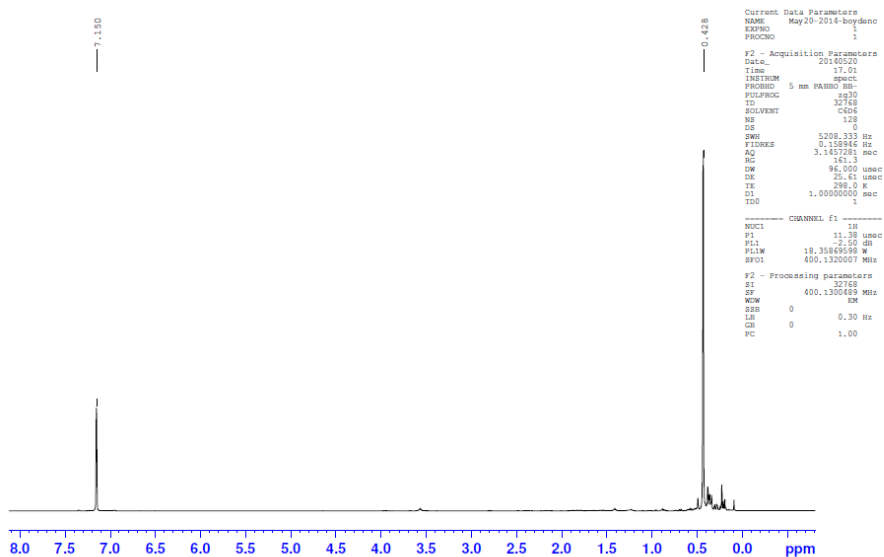


Figure 30. ¹H NMR of P[N(SiMe₃)₂]₃

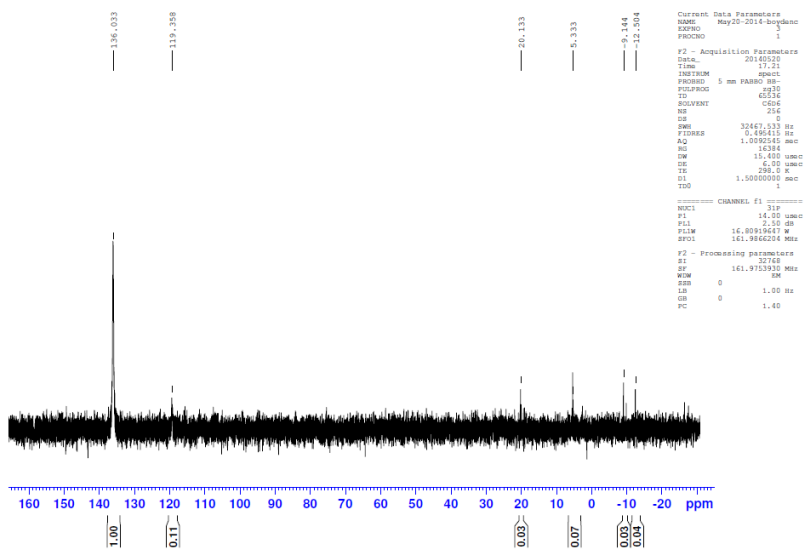


Figure 31. ³¹P NMR of P[N(SiMe₃)₂]₃

Table 12. Crystal Data and Summary of P[N(SiMe₃)₂]₃

compound	P[N(SiMe ₃) ₂] ₃ (1)	
formula	C ₁₈ H ₅₄ PN ₃ Si ₆	
formula weight	512.13	
color of cryst	colorless	
cryst dimens, mm	0.40 x 0.35 x 0.30	
space group	<i>P</i> $\bar{1}$	
cell dimens	<i>a</i> , Å	8.9279(5)
	<i>b</i> , Å	19.0519(10)
	<i>c</i> , Å	20.6374(10)
	α , deg	115.0854(12)
	β , deg	97.9463(13)
	γ , deg	95.3845(15)
volume, Å ³	3102.8(3)	
<i>Z</i>	4	
calcd density, Mg/m ³	1.096	
abs coeff, mm ⁻¹	0.331	
<i>F</i> (000)	1128	
radiation type	Mo- <i>K</i> α (0.71073 Å)	
temperature, K	100(2)	
limits of data collection	2.15 \leq θ \leq 26.38 °	
index ranges	-11 \leq <i>h</i> \leq 11, -23 \leq <i>k</i> \leq 22, -14 \leq <i>l</i> \leq 25	
total reflcns collected	34 673	
unique reflcns	12 599 (<i>R</i> _{int} = 0.0385)	
transmission factors	0.8789–0.9072	
data/restraints/param	12 599 / 0 / 561	
<i>R</i> indices (<i>I</i> > 2 σ (<i>I</i>))	<i>R</i> ₁ = 0.0422, <i>wR</i> ₂ = 0.0967	
<i>R</i> indices (all data)	<i>R</i> ₁ = 0.0540, <i>wR</i> ₂ = 0.1034	
goodness of fit on <i>F</i> ²	1.009	
max/min peak in final diff map, e ⁻ /Å ³	0.757/-0.554	

Table 13. Fractional coordinates and equivalent isotropic displacement parameters (\AA^2) for P[N(SiMe₃)₂]. U_{eq} is defined as one third of the trace of the orthogonalized U_{ij} tensor.

	<i>x</i>	<i>y</i>	<i>z</i>	U_{eq}
Si1	0.52388(7)	0.60003(4)	0.36568(3)	0.02103(14)
Si2	0.28561(7)	0.46172(3)	0.33723(3)	0.01850(13)
Si3	0.45341(7)	0.36163(4)	0.13266(3)	0.01784(13)
Si4	0.11323(7)	0.35885(4)	0.10608(4)	0.02258(14)
Si5	0.33559(7)	0.59150(4)	0.12941(3)	0.02129(14)
Si6	0.14068(7)	0.63097(3)	0.24482(3)	0.01809(13)
Si7	-0.10634(8)	1.02429(4)	0.14426(3)	0.02498(15)
Si8	-0.44110(7)	0.98654(4)	0.15051(3)	0.02186(14)
Si9	-0.26187(7)	1.20973(3)	0.32469(3)	0.01743(13)
Si10	0.01005(7)	1.18314(4)	0.41141(3)	0.01966(13)
Si11	-0.33410(7)	1.00339(4)	0.38725(4)	0.02326(14)
Si12	-0.14998(7)	0.89850(4)	0.28534(3)	0.02119(14)
P1	0.38177(7)	0.50983(4)	0.21629(3)	0.01024(18)
P1'	0.2338(3)	0.48947(14)	0.21914(13)	0.0110(7)
P2	-0.13907(7)	1.04734(4)	0.28305(3)	0.01029(19)
P2'	-0.2886(2)	1.05238(13)	0.28812(12)	0.0107(6)
N1	0.36856(19)	0.52513(10)	0.30462(9)	0.0164(4)
N2	0.2967(2)	0.41147(10)	0.15810(9)	0.0164(4)
N3	0.26832(19)	0.57123(10)	0.19820(9)	0.0139(3)
N4	-0.2478(2)	1.02421(11)	0.19756(9)	0.0207(4)
N5	-0.15808(19)	1.14233(9)	0.34145(9)	0.0129(3)
N6	-0.2264(2)	0.98762(10)	0.31788(10)	0.0169(4)
C1	0.6216(3)	0.65466(15)	0.32244(15)	0.0328(6)
H1A	0.6657	0.6191	0.2841	0.049
H1B	0.7012	0.6955	0.3585	0.049
H1C	0.5483	0.6776	0.3025	0.049
C2	0.4595(3)	0.67670(15)	0.44530(15)	0.0373(6)
H2A	0.3544	0.6799	0.4309	0.056
H2B	0.5226	0.7268	0.4607	0.056
H2C	0.4687	0.6625	0.4849	0.056
C3	0.6789(3)	0.55868(15)	0.40187(12)	0.0260(5)
H3A	0.6358	0.528	0.4237	0.039
H3B	0.756	0.6009	0.4379	0.039
H3C	0.7244	0.5259	0.3626	0.039
C4	0.3028(3)	0.51307(16)	0.43850(12)	0.0326(6)
H4A	0.4092	0.5309	0.4616	0.049
H4B	0.2578	0.4773	0.4549	0.049
H4C	0.2503	0.5573	0.451	0.049
C5	0.0745(3)	0.42533(15)	0.30396(14)	0.0320(6)
H5A	0.0197	0.4633	0.3342	0.048
H5B	0.0489	0.3764	0.3061	0.048
H5C	0.0466	0.4176	0.2545	0.048
C6	0.3828(3)	0.37502(15)	0.31886(15)	0.0335(6)
H6A	0.3665	0.3428	0.2672	0.05
H6B	0.3414	0.345	0.3417	0.05
H6C	0.4909	0.3925	0.3383	0.05

Table 13 (cont.)

	x	y	z	U_{eq}
C7	0.6330(3)	0.40310(16)	0.20403(13)	0.0288(5)
H7A	0.6715	0.455	0.2107	0.043
H7B	0.7085	0.37	0.1889	0.043
H7C	0.6112	0.4057	0.2492	0.043
C8	0.4058(3)	0.25621(14)	0.11427(13)	0.0306(6)
H8A	0.3805	0.2536	0.157	0.046
H8B	0.4927	0.2308	0.102	0.046
H8C	0.3198	0.2302	0.0743	0.046
C9	0.5054(3)	0.36154(15)	0.04771(12)	0.0279(5)
H9A	0.4184	0.3366	0.0082	0.042
H9B	0.589	0.3333	0.0358	0.042
H9C	0.5356	0.4147	0.0557	0.042
C10	0.0417(3)	0.27854(14)	0.12999(14)	0.0318(6)
H10A	0.0476	0.2284	0.0917	0.048
H10B	-0.063	0.2807	0.1357	0.048
H10C	0.1038	0.2855	0.1748	0.048
C11	0.1142(3)	0.30715(16)	0.00605(13)	0.0358(6)
H11A	0.1449	0.3451	-0.0108	0.054
H11B	0.0132	0.2791	-0.0201	0.054
H11C	0.1852	0.2708	-0.0021	0.054
C12	-0.0329(3)	0.42411(16)	0.11422(16)	0.0366(6)
H12A	-0.0442	0.4498	0.1642	0.055
H12B	-0.1295	0.3933	0.0841	0.055
H12C	-0.0005	0.4629	0.0986	0.055
C13	0.5443(3)	0.5931(2)	0.13103(16)	0.0458(8)
H13A	0.601	0.6356	0.1756	0.069
H13B	0.5694	0.6002	0.0902	0.069
H13C	0.5703	0.5442	0.1281	0.069
C14	0.2318(3)	0.51914(18)	0.03715(13)	0.0415(7)
H14A	0.2476	0.4673	0.0295	0.062
H14B	0.2699	0.5312	0.0011	0.062
H14C	0.1242	0.5215	0.033	0.062
C15	0.3112(4)	0.69185(19)	0.1382(2)	0.0602(10)
H15A	0.2052	0.6972	0.1372	0.09
H15B	0.3439	0.6984	0.0984	0.09
H15C	0.3722	0.7312	0.1835	0.09
C16	-0.0209(3)	0.63463(16)	0.17800(14)	0.0311(6)
H16A	0.0154	0.6306	0.1351	0.047
H16B	-0.0579	0.6835	0.2	0.047
H16C	-0.1027	0.5917	0.1648	0.047
C17	0.2415(3)	0.73359(14)	0.30690(14)	0.0317(6)
H17A	0.3278	0.7321	0.3394	0.048
H17B	0.172	0.7631	0.3348	0.048
H17C	0.2765	0.7582	0.2784	0.048
C18	0.0437(3)	0.60016(14)	0.30525(12)	0.0252(5)
H18A	-0.0185	0.5492	0.2766	0.038
H18B	-0.0199	0.6375	0.3285	0.038

Table 13 (cont.)

	x	y	z	U_{eq}
H18C	0.1197	0.5978	0.3417	0.038
C19	-0.5653(3)	0.95665(18)	0.20274(15)	0.0379(6)
H19A	-0.5274	0.9156	0.212	0.057
H19B	-0.6684	0.9378	0.1749	0.057
H19C	-0.5645	1.0011	0.2483	0.057
C20	-0.4564(3)	0.89597(15)	0.06235(13)	0.0328(6)
H20A	-0.3955	0.9078	0.0323	0.049
H20B	-0.5617	0.8787	0.0373	0.049
H20C	-0.4199	0.8551	0.0724	0.049
C21	-0.5314(3)	1.05733(15)	0.12305(13)	0.0302(6)
H21A	-0.5176	1.1075	0.1648	0.045
H21B	-0.639	1.0377	0.104	0.045
H21C	-0.4837	1.0631	0.0862	0.045
C22	-0.0498(3)	0.92507(15)	0.09761(14)	0.0366(6)
H22A	-0.0235	0.9053	0.1327	0.055
H22B	0.0371	0.9297	0.0761	0.055
H22C	-0.1341	0.8895	0.0602	0.055
C23	-0.1789(3)	1.05142(16)	0.07006(14)	0.0360(6)
H23A	-0.2684	1.0143	0.0386	0.054
H23B	-0.1007	1.0508	0.0423	0.054
H23C	-0.2049	1.1031	0.0912	0.054
C24	0.0737(3)	1.09691(17)	0.19663(16)	0.0424(7)
H24A	0.0479	1.1474	0.2249	0.064
H24B	0.1351	1.1009	0.1632	0.064
H24C	0.1304	1.0797	0.2286	0.064
C25	-0.4752(3)	1.18529(17)	0.31057(17)	0.0376(7)
H25A	-0.5076	1.1296	0.2818	0.056
H25B	-0.5226	1.2126	0.2857	0.056
H25C	-0.5051	1.2011	0.357	0.056
C26	-0.2164(3)	1.22569(13)	0.24619(12)	0.0265(5)
H26A	-0.1081	1.2433	0.2544	0.04
H26B	-0.2712	1.2648	0.2414	0.04
H26C	-0.2464	1.1773	0.2023	0.04
C27	-0.2157(4)	1.30908(15)	0.40424(14)	0.0400(7)
H27A	-0.2447	1.3056	0.446	0.06
H27B	-0.2712	1.3446	0.3929	0.06
H27C	-0.1075	1.3282	0.4147	0.06
C28	0.1458(3)	1.25251(15)	0.39520(13)	0.0297(5)
H28A	0.1861	1.2236	0.3525	0.045
H28B	0.2286	1.2786	0.4367	0.045
H28C	0.0922	1.2909	0.3881	0.045
C29	-0.0371(3)	1.23539(16)	0.50425(12)	0.0326(6)
H29A	-0.044	1.2889	0.5144	0.049
H29B	0.042	1.2345	0.5403	0.049
H29C	-0.1335	1.2095	0.5055	0.049
C30	0.1249(3)	1.10826(16)	0.41682(14)	0.0323(6)
H30A	0.0602	1.0679	0.4212	0.048

Table 13 (cont.)

	x	y	z	U_{eq}
H30B	0.2072	1.133	0.4587	0.048
H30C	0.1666	1.0853	0.3734	0.048
C31	-0.4379(3)	1.08880(16)	0.41329(14)	0.0313(6)
H31A	-0.367	1.1359	0.426	0.047
H31B	-0.4832	1.0941	0.4544	0.047
H31C	-0.517	1.0804	0.3729	0.047
C32	-0.2076(3)	1.02237(17)	0.47540(14)	0.0337(6)
H32A	-0.1514	0.9799	0.4677	0.051
H32B	-0.2696	1.0262	0.5109	0.051
H32C	-0.1371	1.0707	0.4928	0.051
C33	-0.4878(3)	0.91560(16)	0.35944(16)	0.0368(6)
H33A	-0.5834	0.925	0.3396	0.055
H33B	-0.4988	0.9071	0.4013	0.055
H33C	-0.4596	0.8699	0.3232	0.055
C34	-0.2625(3)	0.82539(14)	0.19450(15)	0.0386(6)
H34A	-0.3675	0.8146	0.1981	0.058
H34B	-0.2204	0.7777	0.1789	0.058
H34C	-0.2578	0.8462	0.1597	0.058
C35	-0.1475(4)	0.84952(17)	0.34716(16)	0.0468(8)
H35A	-0.0732	0.8806	0.3913	0.07
H35B	-0.1209	0.7983	0.3232	0.07
H35C	-0.2473	0.8445	0.3588	0.07
C36	0.0561(3)	0.91105(16)	0.27834(19)	0.0450(8)
H36A	0.0707	0.9398	0.2505	0.068
H36B	0.085	0.8603	0.2545	0.068
H36C	0.1185	0.9394	0.3264	0.068

Table 13 Crystal Data and Summary of Sb[N(SiMe₃)₂]₃

compound	Sb[N(SiMe ₃) ₂] ₃ · ¹ / ₂ HN(SiMe ₃) ₂ (3)
formula	C ₂₁ H _{63.5} SbN _{3.5} Si ₇
formula weight	683.63
color of cryst	pale yellow
cryst dimens, mm	0.24 x 0.22 x 0.16
space group	<i>P</i> $\bar{3}$
cell dimens	<i>a</i> , Å 16.0906(10)
	<i>b</i> , Å 16.0906(10)
	<i>c</i> , Å 8.4214(5)
	α , deg 90
	β , deg 90
	γ , deg 120
volume, Å ³	1888.2(3)
<i>Z</i>	2
calcd density, Mg/m ³	1.202
abs coeff, mm ⁻¹	0.968
<i>F</i> (000)	726
radiation type	Mo- <i>K</i> α (0.71073 Å)
temperature, K	100.0(5)
limits of data collection	2.42 \leq θ \leq 33.72
index ranges	-25 \leq <i>h</i> \leq 12, -25 \leq <i>k</i> \leq 0, -13 \leq <i>l</i> \leq 13
total reflcns collected	37 098
unique reflcns	5043 (<i>R</i> _{int} = 0.0606)
transmission factors	0.6419–0.7467
data/restraints/param	5043 / 77 / 157
<i>R</i> indices (<i>I</i> > 2 σ (<i>I</i>))	<i>R</i> ₁ = 0.0596, <i>wR</i> ₂ = 0.1522
<i>R</i> indices (all data)	<i>R</i> ₁ = 0.0715, <i>wR</i> ₂ = 0.1635
goodness of fit on <i>F</i> ²	1.039
max/min peak in final diff map, e ⁻ /Å ³	1.987/-0.990

Table 15. Fractional coordinates and equivalent isotropic displacement parameters (\AA^2) for $\text{Sb}[\text{N}(\text{SiMe}_3)_2]$. U_{eq} is defined as one third of the trace of the orthogonalized U_{ij} tensor.

	<i>x</i>	<i>y</i>	<i>z</i>	U_{eq}
Sb1	0.6667	0.3333	0.85771(6)	0.02521(11)
N1	0.7435(5)	0.4696(2)	0.7523(8)	0.0318(8)
Si1	0.84046(16)	0.54515(13)	0.8773(3)	0.0444(4)
C1	0.9565(5)	0.6064(7)	0.7611(11)	0.073(2)
H1A	0.9665	0.5578	0.7081	0.109
H1B	1.01	0.6441	0.8336	0.109
H1C	0.9531	0.6489	0.6813	0.109
C2	0.8584(7)	0.4785(7)	1.0417(11)	0.075(2)
H2A	0.8663	0.4265	0.9975	0.112
H2B	0.8024	0.4514	1.1121	0.112
H2C	0.9159	0.5224	1.1021	0.112
C3	0.8272(7)	0.6403(7)	0.9742(15)	0.088(3)
H3A	0.8157	0.6773	0.8936	0.132
H3B	0.886	0.683	1.0328	0.132
H3C	0.7729	0.6114	1.048	0.132
Si2	0.70342(14)	0.52354(13)	0.6143(2)	0.0415(3)
C4	0.8072(7)	0.6240(6)	0.5098(12)	0.069(2)
H4A	0.8456	0.5999	0.4584	0.104
H4B	0.847	0.6739	0.5867	0.104
H4C	0.7835	0.6511	0.4293	0.104
C5	0.6262(5)	0.4407(5)	0.4596(9)	0.0565(15)
H5A	0.6594	0.4109	0.408	0.085
H5B	0.6114	0.4762	0.3805	0.085
H5C	0.5664	0.3908	0.5076	0.085
C6	0.6356(7)	0.5761(6)	0.7095(12)	0.069(2)
H6A	0.675	0.6209	0.7932	0.104
H6B	0.5762	0.5247	0.7558	0.104
H6C	0.6201	0.6105	0.6295	0.104
Sb1'	0.6667	0.3333	0.6350(2)	0.0304(6)
N1'	0.733(2)	0.4666(7)	0.750(3)	0.0318(8)
Si1'	0.8258(9)	0.5197(8)	0.8888(16)	0.0444(4)
C1'	0.934(2)	0.632(2)	0.798(5)	0.073(2)
H1D	0.9125	0.6749	0.7554	0.109
H1E	0.9616	0.6125	0.7119	0.109
H1F	0.9826	0.6657	0.8799	0.109
C2'	0.884(3)	0.453(2)	0.966(5)	0.075(2)
H2D	0.9011	0.4247	0.877	0.112
H2E	0.8396	0.4011	1.0368	0.112
H2F	0.9423	0.4965	1.025	0.112
C3'	0.800(3)	0.571(3)	1.068(4)	0.088(3)
H3D	0.7776	0.6152	1.0349	0.132
H3E	0.8585	0.6064	1.1316	0.132
H3F	0.7501	0.5193	1.1319	0.132
Si2'	0.7180(7)	0.5516(6)	0.6440(12)	0.0415(3)
C4'	0.782(2)	0.573(2)	0.444(3)	0.069(2)
H4D	0.7779	0.5132	0.4077	0.104
H4E	0.8498	0.6224	0.4567	0.104
H4F	0.7518	0.5946	0.3662	0.104
C5'	0.5882(14)	0.489(2)	0.568(4)	0.0565(15)

Table 15 (cont.)

	<i>x</i>	<i>y</i>	<i>z</i>	<i>U_{eq}</i>
H5D	0.5777	0.4364	0.4965	0.085
H5E	0.5767	0.5351	0.5109	0.085
H5F	0.544	0.4628	0.6584	0.085
C6'	0.740(2)	0.6624(18)	0.735(4)	0.069(2)
H6D	0.7925	0.6839	0.8115	0.104
H6E	0.6816	0.6518	0.7903	0.104
H6F	0.7569	0.7115	0.653	0.104
C7	0.913(3)	1.028(2)	0.272(5)	0.101(9)
H7A	0.8463	0.9859	0.3073	0.152
H7B	0.9128	1.0444	0.16	0.152
H7C	0.9412	1.0874	0.3357	0.152
C8	1.109(2)	1.046(2)	0.224(6)	0.101(9)
H8A	1.147	1.0138	0.2393	0.152
H8B	1.1391	1.1064	0.2834	0.152
H8C	1.1071	1.0588	0.1112	0.152
C9	0.925(2)	0.851(2)	0.184(5)	0.101(9)
H9A	0.8592	0.8104	0.2211	0.152
H9B	0.9612	0.8171	0.1989	0.152
H9C	0.9246	0.865	0.0706	0.152
Si3	0.9841(14)	0.9662(10)	0.299(2)	0.062(4)
N2	0.985(3)	0.936(3)	0.487(2)	0.079(10)
H2N	0.9822	0.8794	0.4907	0.095
Si4	0.990(2)	0.9760(10)	0.6686(19)	0.062(4)
C10	1.043(3)	0.918(2)	0.797(5)	0.101(9)
H10A	1.1057	0.9333	0.7554	0.152
H10B	1	0.8486	0.7975	0.152
H10C	1.0503	0.9428	0.9059	0.152
C11	0.867(3)	0.941(2)	0.742(5)	0.101(9)
H11A	0.826	0.8711	0.7356	0.152
H11B	0.84	0.9717	0.6757	0.152
H11C	0.8709	0.9617	0.8522	0.152
C12	1.069(3)	1.1100(16)	0.679(5)	0.101(9)
H12A	1.1335	1.1283	0.6406	0.152
H12B	1.0729	1.1313	0.789	0.152
H12C	1.0417	1.1403	0.6123	0.152

Appendix A2

Nanoparticle formation from $P[N(SiMe_3)_2]_3$ and NMR spectra of attempted derivatives

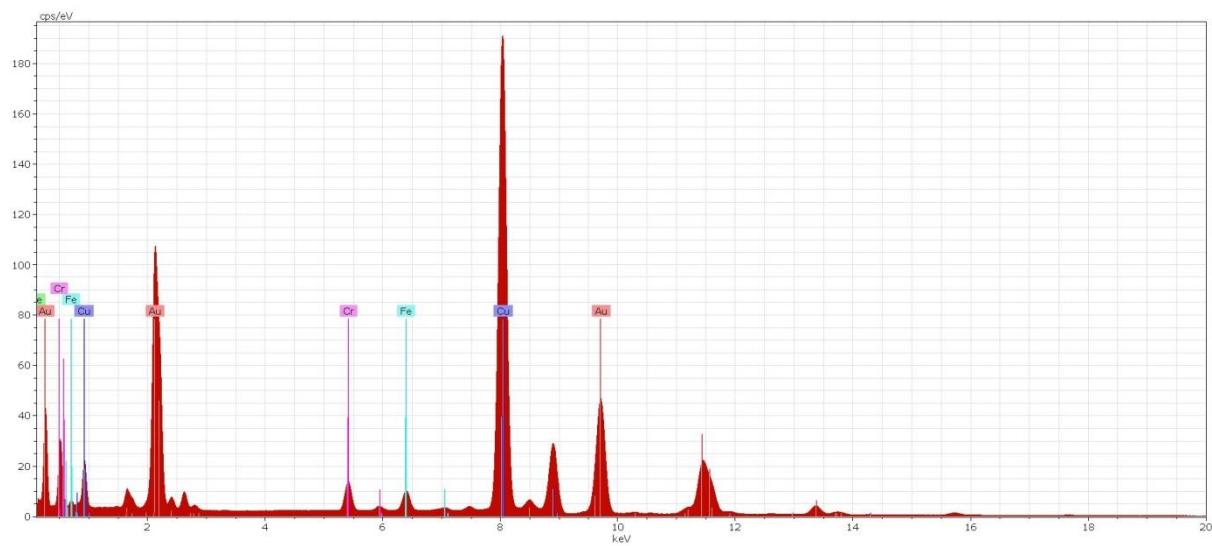


Figure 32. EDS Mapping $HAuCl_4$ Grind

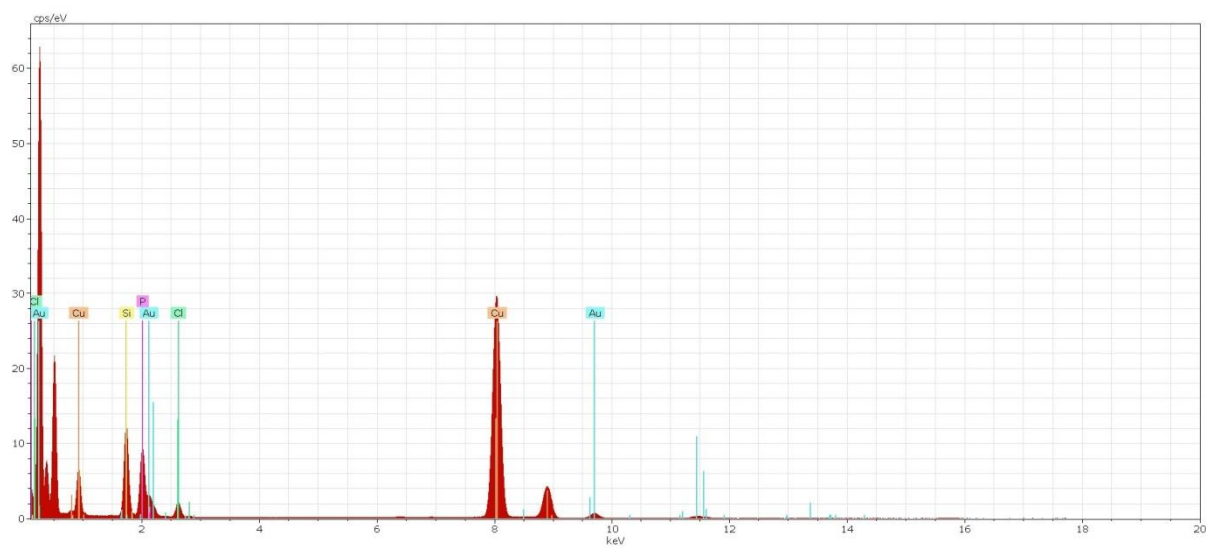


Figure 33. EDS Mapping $HAuCl_4:PN$ THF reaction

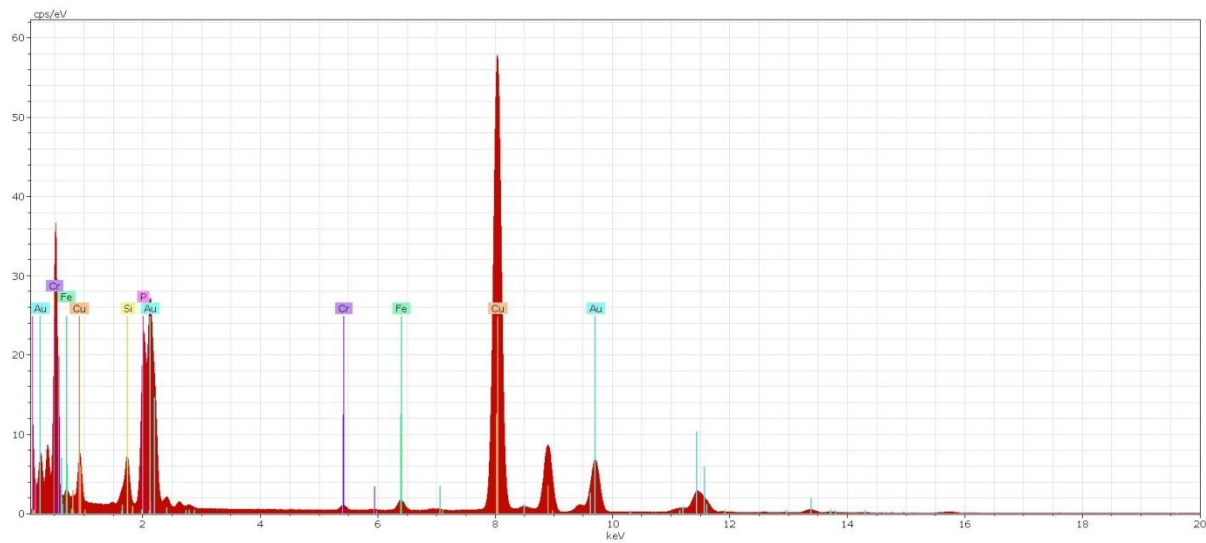


Figure 34. EDS Mapping H_{Au}Cl₄:PN' Grind Reaction

Selected spectra for the $\text{SPCl}_3/\text{OPCl}_3$ reaction with KN'

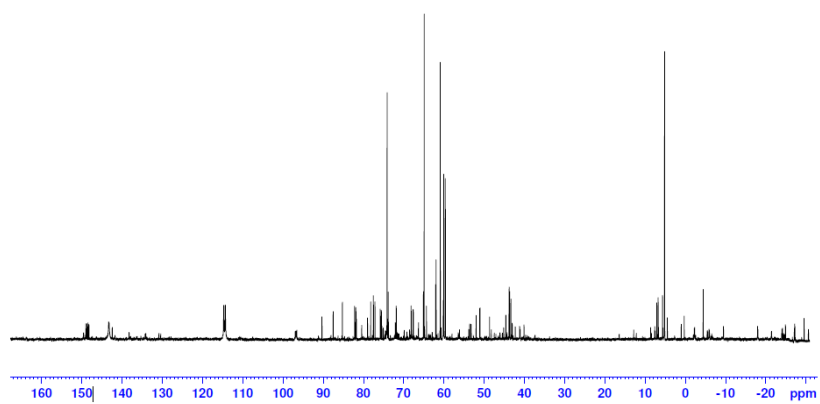


Figure 35. ^{31}P NMR (proton decoupled) 3:1 KN' : SPCl_3

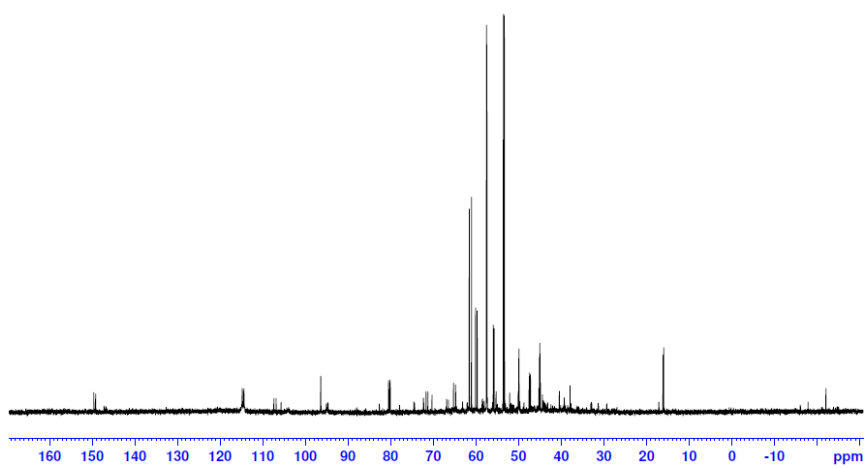


Figure 36. ^{31}P NMR (proton decoupled) 2:1 KN' : SPCl_3

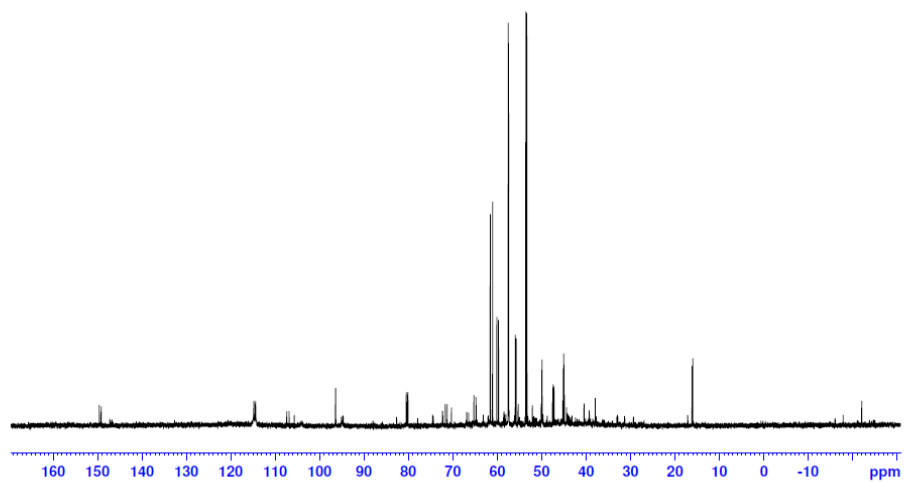


Figure 37. ^{31}P NMR (proton decoupled) 1:1 $\text{KN}'\text{:SPCl}_3$

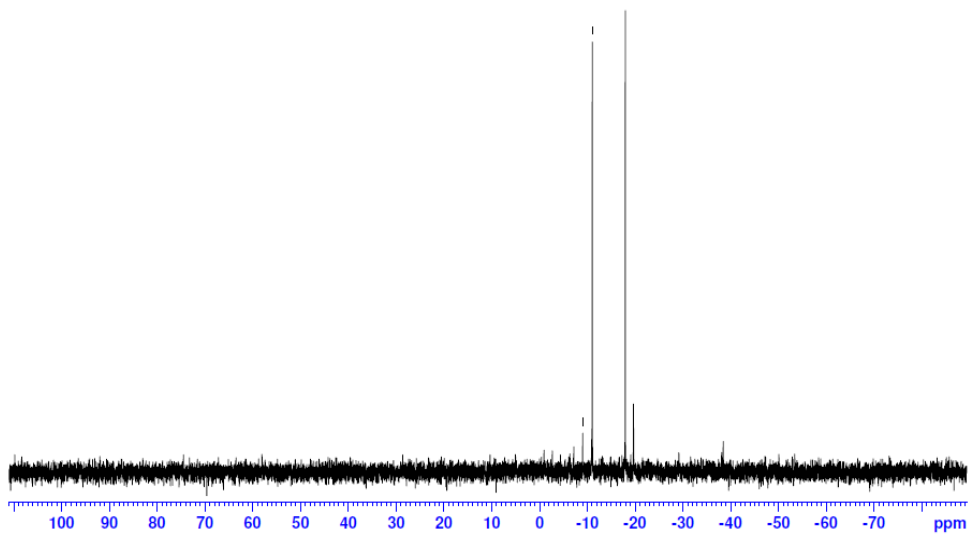


Figure 38. ^{31}P NMR (proton decoupled) 3:1 $\text{KN}'\text{:OPCl}_3$

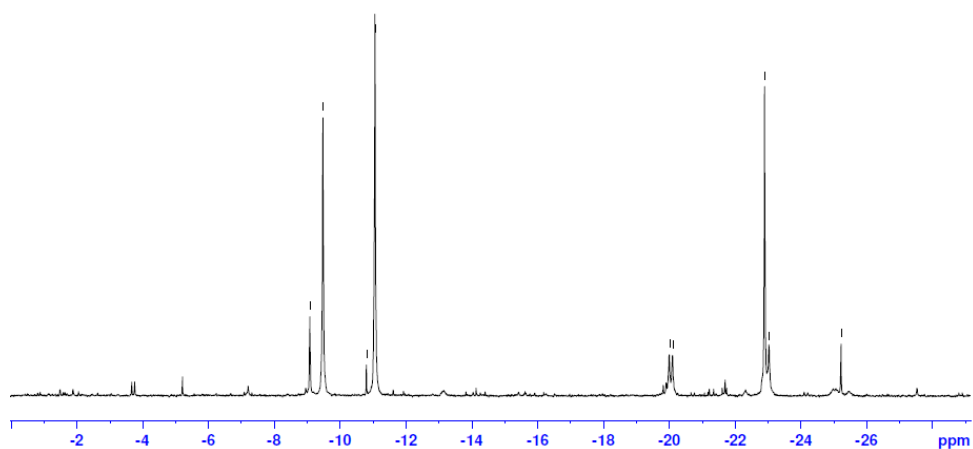


Figure 39. ^{31}P NMR (proton decoupled) 3:1 $\text{KN}':\text{OPCl}_3$ (reaction 2)

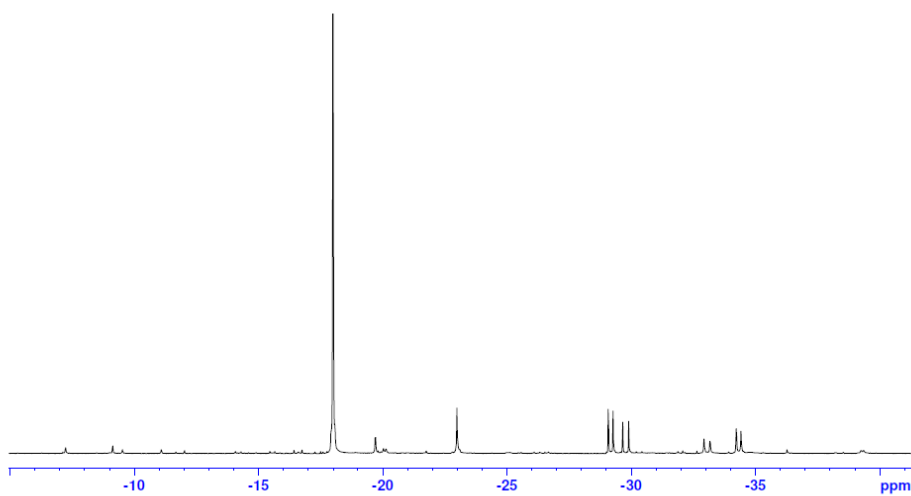


Figure 40. ^{31}P NMR (proton decoupled) 2:1 $\text{KN}':\text{OPCl}_3$

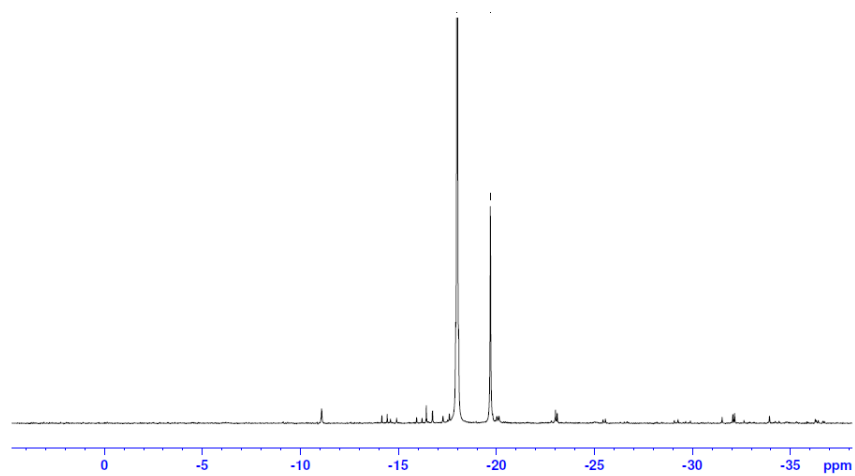


Figure 41. ^{31}P NMR (proton decoupled) 1:1 $\text{KN}':\text{OPCl}_3$

Appendix 3

Crystallographic and fractional coordinates of mixed ligand group 4 species

Table 14. Crystal Data and Summary of Cp₃Ti(OtBu)

formula	C ₁₉ H ₂₄ TiO
formula weight	316.28
color of cryst	red
cryst dimens, mm	0.546 × 0.045 × 0.035
crystal system	tetragonal
space group	<i>P</i> 4 ₂ / <i>n</i>
cell dimens <i>a</i> , Å	19.4641(2)
<i>b</i> , Å	19.4641(2)
<i>c</i> , Å	8.58573(12)
<i>α</i> , deg	90
<i>β</i> deg	90
<i>γ</i> deg	90
volume, Å ³	3252.71(8)
<i>Z</i>	8
calcd density, Mg/m ³	1.292
abs coeff, mm ⁻¹	4.409
<i>F</i> (000)	1344
radiation type	Cu- <i>Kα</i> (1.54184 Å)
temperature, K	100
data collection limits	3.21° ≤ <i>θ</i> ≤ 72.50
index ranges	-19 ≤ <i>h</i> ≤ 21, -24 ≤ <i>k</i> ≤ 23, -10 ≤ <i>l</i> ≤ 10
total reflns	15 228
unique reflns	3189 (<i>R</i> _{int} = 0.0301)
transmission factors	0.398-0.864
data/restraints/param	3189 / 0 / 197
<i>R</i> indices (<i>I</i> > 2 <i>σ</i> (<i>I</i>))	<i>R</i> ₁ = 0.027, <i>wR</i> ₂ = 0.065
<i>R</i> indices (all data)	<i>R</i> ₁ = 0.033, <i>wR</i> ₂ = 0.068
absolute struct param	
goodness of fit on <i>F</i> ²	1.029
max/min peak in final diff map, e ⁻ /Å ³	0.22/-0.29

Table 15. Crystal Data and Summary of Cp₂Zr(OtBu)₂

formula	C ₁₈ H ₂₈ O ₂ Zr
formula weight	367.62
color of cryst	colorless
cryst dimens, mm	0.32 x 0.26 x 0.10
crystal system	tetragonal
space group	<i>P4</i> ₂ <i>m</i>
cell dimens <i>a</i> , Å	8.5606(8)
<i>b</i> , Å	8.5606(8)
<i>c</i> , Å	12.9538(12)
α , deg	90
β deg	90
γ deg	90
volume, Å ³	949.30(15)
<i>Z</i>	2
calcd density, Mg/m ³	1.286
abs coeff, mm ⁻¹	0.581
<i>F</i> (000)	384
radiation type	Mo- <i>K</i> α (0.71073 Å)
temperature, K	173(2)
data collection limits	2.85° ≤ θ ≤ 37.78°
index ranges	-14 ≤ <i>h</i> ≤ 14, -14 ≤ <i>k</i> ≤ 14, -22 ≤ <i>l</i> ≤ 22
total reflcns	35 496
unique reflcns	2737 (<i>R</i> _{int} = 0.0472)
transmission factors	0.8358-0.9442
data/restraints/param	2737 / 28 / 83
<i>R</i> indices (<i>I</i> > 2 σ (<i>I</i>))	<i>R</i> ₁ = 0.033, <i>wR</i> ₂ = 0.076
<i>R</i> indices (all data)	<i>R</i> ₁ = 0.045, <i>wR</i> ₂ = 0.081
absolute struct param	-0.08(8)
goodness of fit on <i>F</i> ²	1.031
max/min peak in final diff map, e ⁻ /Å ³	0.341/-0.445

Table 16. Crystal Data and Summary of Cp₂HfCl(OtBu)

formula	C ₁₄ H ₁₉ ClHfO
formula weight	417.23
color of cryst	colorless
cryst dimens, mm	0.14 × 0.121 × 0.1
crystal system	orthorhombic
space group	<i>Pbca</i>
cell dimens <i>a</i> , Å	15.2640(3)
<i>b</i> , Å	12.0177(3)
<i>c</i> , Å	15.8499(5)
α , deg	90
β deg	90
γ deg	90
volume, Å ³	2907.49(13)
<i>Z</i>	8
calcd density, Mg/m ³	1.906
abs coeff, mm ⁻¹	7.342
<i>F</i> (000)	1600
radiation type	Mo- <i>K</i> α (0.71073 Å)
temperature, K	100
data collection limits	6.32° ≤ θ ≤ 59.66°
index ranges	-19 ≤ <i>h</i> ≤ 20, -15 ≤ <i>k</i> ≤ 16, -21 ≤ <i>l</i> ≤ 21
total reflns	37 558
unique reflns	3899 (<i>R</i> _{int} = 0.0475)
transmission factors	0.498-0.616
data/restraints/param	3899 / 0 / 157
<i>R</i> indices (<i>I</i> > 2 σ (<i>I</i>))	<i>R</i> ₁ = 0.024, <i>wR</i> ₂ = 0.048
<i>R</i> indices (all data)	<i>R</i> ₁ = 0.032, <i>wR</i> ₂ = 0.051
absolute struct param	
goodness of fit on <i>F</i> ²	1.042
max/min peak in final diff map, e ⁻ /Å ³	1.31/-1.74

Table 17. Crystal Data and Summary of Cp₂Hf(OtBu)₂

formula	C ₁₈ H ₂₈ HfO ₂
formula weight	454.89
color of cryst	colorless
cryst dimens, mm	0.18 x 0.16 x 0.12
crystal system	tetragonal
space group	<i>P4</i> ₂ <i>m</i>
cell dimens <i>a</i> , Å	8.4676(7)
<i>b</i> , Å	8.4676(7)
<i>c</i> , Å	12.8196(11)
α , deg	90
β deg	90
γ deg	90
volume, Å ³	919.17(17)
<i>Z</i>	2
calcd density, Mg/m ³	1.644
abs coeff, mm ⁻¹	5.677
<i>F</i> (000)	448
radiation type	Mo- <i>K</i> α (0.71073 Å)
temperature, K	100.0(5)
data collection limits	1.59° \leq θ \leq 38.70°
index ranges	-14 \leq <i>h</i> \leq 14, -14 \leq <i>k</i> \leq 14, -22 \leq <i>l</i> \leq 22
total reflns	34 629
unique reflns	2761 (<i>R</i> _{int} = 0.0345)
transmission factors	0.4405-0.3290
data/restraints/param	2761 / 28 / 83
<i>R</i> indices (<i>I</i> > 2 σ (<i>I</i>))	<i>R</i> ₁ = 0.039, <i>wR</i> ₂ = 0.091
<i>R</i> indices (all data)	<i>R</i> ₁ = 0.044, <i>wR</i> ₂ = 0.093
absolute struct param	-0.023(6)
goodness of fit on <i>F</i> ²	1.170
max/min peak in final diff map, e ⁻ /Å ³	5.421/-2.269

Table 20. Fractional coordinates and equivalent isotropic displacement parameters (\AA^2) for $\text{Cp}_3\text{Ti}(\text{OtBu})$. U_{eq} is defined as one third of the trace of the orthogonalized U_{ij} tensor.

	<i>x</i>	<i>y</i>	<i>z</i>	U_{eq}
Ti1	0.45546(2)	0.31793(2)	0.51643(3)	0.01174(8)
O1	0.53547(5)	0.29889(5)	0.61075(11)	0.0158(2)
C1	0.50415(7)	0.41347(7)	0.40270(15)	0.0136(3)
C16	0.59441(7)	0.29000(7)	0.70530(15)	0.0170(3)
C6	0.43093(8)	0.37742(8)	0.76261(16)	0.0199(3)
H6	0.467	0.3906	0.8309	0.024
C2	0.45534(7)	0.45140(7)	0.30676(16)	0.0151(3)
H2	0.4143	0.4724	0.3428	0.018
C5	0.55981(7)	0.39546(7)	0.29800(15)	0.0149(3)
H5	0.6008	0.3722	0.3269	0.018
C4	0.54382(7)	0.41731(7)	0.15124(16)	0.0177(3)
H4	0.5712	0.4109	0.0609	0.021
C3	0.47836(7)	0.45178(7)	0.15669(16)	0.0173(3)
H3	0.4551	0.4715	0.0702	0.021
C10	0.40223(7)	0.41816(7)	0.64559(17)	0.0195(3)
H10	0.4155	0.4638	0.6206	0.023
C14	0.38048(8)	0.26486(7)	0.32696(17)	0.0206(3)
H14	0.3346	0.2806	0.315	0.025
C15	0.43772(8)	0.28901(7)	0.24548(16)	0.0198(3)
H15	0.4378	0.3248	0.1703	0.024
C11	0.49564(8)	0.25062(7)	0.29471(17)	0.0209(3)
H11	0.5413	0.256	0.2577	0.025
C13	0.40294(8)	0.21276(7)	0.43072(18)	0.0217(3)
H13	0.3751	0.1885	0.503	0.026
C9	0.35013(8)	0.37988(8)	0.57067(18)	0.0215(3)
H9	0.3229	0.3947	0.4852	0.026
C12	0.47388(8)	0.20352(7)	0.40726(18)	0.0219(3)
H12	0.5021	0.1709	0.459	0.026
C7	0.39703(8)	0.31330(8)	0.76174(17)	0.0226(3)
H7	0.4069	0.2753	0.8275	0.027
C8	0.34597(8)	0.31575(8)	0.64591(18)	0.0234(3)
H8	0.3141	0.2802	0.6225	0.028
C17	0.62814(8)	0.36036(8)	0.72639(17)	0.0229(3)
H17A	0.6416	0.3786	0.6245	0.034
H17B	0.6689	0.3557	0.7924	0.034
H17C	0.5955	0.3919	0.7758	0.034
C19	0.57206(9)	0.26004(8)	0.86231(17)	0.0245(3)
H19A	0.5411	0.2924	0.9146	0.037
H19B	0.6126	0.2522	0.9275	0.037
H19C	0.5481	0.2164	0.8452	0.037
C18	0.64310(8)	0.24092(8)	0.62192(18)	0.0248(3)
H18A	0.62	0.1968	0.605	0.037
H18B	0.6842	0.2338	0.6859	0.037
H18C	0.6564	0.2606	0.5213	0.037
H1	0.5160(8)	0.4296(8)	0.5032(19)	0.016(4)

Table 21. Fractional coordinates and equivalent isotropic displacement parameters (\AA^2) for $\text{Cp}_2\text{Zr}(\text{OtBu})_2\text{P}[\text{N}(\text{SiMe}_3)_2]$. U_{eq} is defined as one third of the trace of the orthogonalized U_{ij} tensor.

	<i>x</i>	<i>y</i>	<i>z</i>	U_{eq}
Zr1	0.5	0	0.330591(16)	0.03166(7)
C1	0.7318(9)	0.1888(9)	0.3312(4)	0.072(3)
H1	0.7794	0.2112	0.2666	0.086
C2	0.6067(6)	0.2694(8)	0.3796(5)	0.0565(10)
H2	0.5556	0.3584	0.3517	0.068
C3	0.5709(8)	0.2029(8)	0.4700(5)	0.0619(9)
H3	0.4906	0.2363	0.5155	0.074
C4	0.6716(6)	0.0754(10)	0.4864(6)	0.0619(9)
H4	0.672	0.0083	0.5448	0.074
C5	0.7700(8)	0.0657(6)	0.4020(5)	0.0565(10)
H5	0.8497	-0.0101	0.3924	0.068
O1	0.37819(18)	0.12181(18)	0.23511(15)	0.0510(5)
C6	0.3124(4)	0.2293(4)	0.1637(3)	0.0471(11)
C7	0.1621(13)	0.2856(15)	0.2115(6)	0.121(6)
H7A	0.0934	0.1962	0.2245	0.182
H7B	0.1102	0.3584	0.1642	0.182
H7C	0.1848	0.3389	0.2767	0.182
C8	0.4190(9)	0.3652(7)	0.1411(5)	0.099(3)
H8A	0.431	0.429	0.2034	0.149
H8B	0.3738	0.4289	0.0857	0.149
H8C	0.5214	0.326	0.1193	0.149
C9	0.2798(9)	0.1323(7)	0.0678(4)	0.100(3)
H9A	0.3786	0.0932	0.0395	0.15
H9B	0.2273	0.1972	0.016	0.15
H9C	0.2125	0.0438	0.0859	0.15

Table 22. Fractional coordinates and equivalent isotropic displacement parameters (\AA^2) for $\text{Cp}_2\text{HfCl}(\text{OtBu})$. U_{eq} is defined as one third of the trace of the orthogonalized U_{ij} tensor.

	<i>x</i>	<i>y</i>	<i>z</i>	U_{eq}
Table 18. Fractional Coordinates $\text{Cp}_2\text{HfCl}(\text{OtBu})$				
Hf1	0.5	0	0.32900(2)	0.02548(9)
C1	0.7336(18)	0.1874(18)	0.3291(10)	0.062(9)
H1	0.7817	0.2097	0.2638	0.075
C2	0.6077(16)	0.271(2)	0.3763(14)	0.047(3)
H2	0.5564	0.3605	0.3474	0.056
C3	0.571(2)	0.202(2)	0.4711(12)	0.049(3)
H3	0.4908	0.2352	0.5182	0.059
C4	0.673(2)	0.074(2)	0.4846(12)	0.049(3)
H4	0.6744	0.0052	0.543	0.059
C5	0.773(2)	0.0640(18)	0.3985(13)	0.047(3)
H5	0.854	-0.0124	0.3883	0.056
O1	0.3782(7)	0.1218(7)	0.2323(6)	0.0457(17)
C6	0.3169(12)	0.2390(12)	0.1615(7)	0.031(2)
C7	0.163(2)	0.295(2)	0.2095(13)	0.058(7)
H7A	0.0911	0.205	0.2168	0.086
H7B	0.1151	0.3748	0.1643	0.086
H7C	0.1843	0.3406	0.2783	0.086
C8	0.425(2)	0.3778(19)	0.1416(12)	0.058(5)
H8A	0.4496	0.4302	0.2079	0.087
H8B	0.3732	0.4528	0.0947	0.087
H8C	0.5234	0.3403	0.1095	0.087
C9	0.287(2)	0.1479(18)	0.0621(9)	0.053(4)
H9A	0.3886	0.1216	0.0293	0.08
H9B	0.2244	0.2125	0.0142	0.08
H9C	0.23	0.0504	0.0783	0.08

Table 23. Fractional coordinates and equivalent isotropic displacement parameters (\AA^2) for $\text{Cp}_2\text{Hf}(\text{OtBu})_2$. U_{eq} is defined as one third of the trace of the orthogonalized U_{ij} tensor.

	<i>x</i>	<i>y</i>	<i>z</i>	U_{eq}
Hf1	0.38609(2)	0.34365(2)	0.68544(2)	0.00886(5)
C11	0.40318(5)	0.54242(7)	0.71962(5)	0.01999(17)
O1	0.28320(14)	0.35964(18)	0.61717(14)	0.0142(5)
C1	0.4719(2)	0.3673(3)	0.5501(2)	0.0183(7)
H1	0.4505	0.419	0.5097	0.022
C2	0.4487(2)	0.2534(3)	0.5555(2)	0.0168(7)
H2	0.4095	0.2151	0.5191	0.02
C3	0.4945(2)	0.2068(3)	0.6247(2)	0.0165(7)
H3	0.4912	0.1317	0.6431	0.02
C4	0.5460(2)	0.2920(3)	0.6616(2)	0.0176(7)
H4	0.5833	0.2842	0.7093	0.021
C5	0.5320(2)	0.3908(3)	0.6149(2)	0.0188(7)
H5	0.5585	0.4608	0.6255	0.023
C6	0.3788(2)	0.3406(3)	0.8466(2)	0.0185(7)
H6	0.4024	0.401	0.8778	0.022
C7	0.4246(2)	0.2440(3)	0.8228(2)	0.0182(7)
H7	0.4842	0.2279	0.835	0.022
C8	0.3659(2)	0.1748(3)	0.7772(2)	0.0195(7)
H8	0.3796	0.1048	0.7525	0.023
C9	0.2829(2)	0.2289(3)	0.7748(2)	0.0210(7)
H9	0.231	0.2003	0.7499	0.025
C10	0.2914(2)	0.3327(3)	0.8163(2)	0.0181(7)
H10	0.2468	0.3872	0.8227	0.022
C11	0.2142(2)	0.3621(3)	0.5568(2)	0.0147(6)
C12	0.2486(2)	0.4139(3)	0.4749(2)	0.0203(7)
H12A	0.2697	0.4894	0.4862	0.03
H12B	0.2012	0.4169	0.4332	0.03
H12C	0.2967	0.3685	0.4528	0.03
C13	0.1409(2)	0.4352(4)	0.5937(2)	0.0305(9)
H13A	0.1212	0.4037	0.6474	0.046
H13B	0.0916	0.4378	0.5541	0.046
H13C	0.1632	0.5107	0.603	0.046
C14	0.1827(3)	0.2437(3)	0.5416(2)	0.0272(8)
H14A	0.2317	0.1982	0.5214	0.041
H14B	0.136	0.2441	0.4992	0.041
H14C	0.1603	0.2124	0.5945	0.041

Table 19. Crystal Data and Summary of Cp₂TiCl(OMe)

Compound	Cp ₂ TiCl(OMe)
Empirical formula	C ₁₁ H ₁₃ ClOTi
Formula weight	244.58
Color of compound	orange
Temperature/K	100
Crystal system	orthorhombic
Space group	<i>Pbca</i>
a/Å	12.4890(3)
b/Å	11.4556(2)
c/Å	14.6289(3)
α/°	90
β/°	90
γ/°	90
Volume/Å ³	2092.94(7)
Z	8
ρ _{calc} g/cm ³	1.555
μ/mm ⁻¹	1.056
F(000)	1008
Crystal size/mm ³	0.45 × 0.28 × 0.11
Radiation	MoKα (λ = 0.71073)
2Θ range for data collect/°	6.456 to 65.458
Index ranges	-18 ≤ h ≤ 8, -16 ≤ k ≤ 16, -21 ≤ l ≤ 21
Reflections collected	17 721
Independent reflections	3612 [R _{int} = 0.0271, R _{sigma} = 0.0215]
Data/restraints/parameters	3612/1/138
Goodness-of-fit on F ²	1.054
Final R indexes [I > 2σ (I)]	R1 = 0.0319, wR2 = 0.0659
Final R indexes [all data]	R1 = 0.0618, wR2 = 0.1285
Largest diff. peak/hole/e ⁻ Å ⁻³	0.23/-0.30

Table 20. Crystal Data and Summary of Cp₂TiCl(OiPr)

Compound	Cp ₂ TiCl(OiPr)
Empirical formula	C ₁₃ H ₁₇ ClOTi
Formula weight	272.61
Color of compound	yellow
Temperature/K	223
Crystal system	orthorhombic
Space group	<i>Pnma</i>
a/Å	13.0890(8)
b/Å	10.6775(6)
c/Å	9.3276(6)
α/°	90
β/°	90
γ/°	90
Volume/Å ³	1303.61(14)
Z	4
ρ _{calc} g/cm ³	1.389
μ/mm ⁻¹	3.365
F(000)	1344
Crystal size/mm ³	0.443 × 0.118 × 0.094
Radiation	MoKα (λ = 0.71073)
2Θ range for data collect/°	3.113 to 29.770
Index ranges	-16 ≤ h ≤ 18, -14 ≤ k ≤ 14, -12 ≤ l ≤ 12
Reflections collected	8461
Independent reflections	1808 [R _{int} = 0.0577, R _{sigma} = 0.0150]
Data/restraints/parameters	1808/156/133
Goodness-of-fit on F ²	0.986
Final R indexes [I > 2σ (I)]	R1 = 0.0601, wR2 = 0.1394
Final R indexes [all data]	R1 = 0.0713, wR2 = 0.1461
Largest diff. peak/hole/e ⁻ Å ⁻³	0.23/-0.30

Table 21. Crystal Data and Summary of Cp₂TiCl(OtBu)

Compound	Cp ₂ TiCl(OtBu)
Empirical formula	C ₁₄ H ₁₉ ClOTi
Formula weight	286.64
Color of compound	Yellow
Temperature/K	100
Crystal system	orthorhombic
Space group	<i>Pbca</i>
a/Å	15.01162(13)
b/Å	11.84446(11)
c/Å	15.51368(15)
α/°	90
β/°	90
γ/°	90
Volume/Å ³	2758.40(4)
Z	8
ρ _{calc} g/cm ³	1.380
μ/mm ⁻¹	6.878
F(000)	1200
Crystal size/mm ³	0.223 × 0.125 × 0.084
Radiation	CuKα (λ = 1.54184)
2θ range for data collect/°	11.094 to 145.054
Index ranges	-18 ≤ h ≤ 18, -14 ≤ k ≤ 14, -18 ≤ l ≤ 19
Reflections collected	15 770
Independent reflections	2724 [R _{int} = 0.0254, R _{sigma} = 0.0150]
Data/restraints/parameters	2724/0/157
Goodness-of-fit on F ²	1.050
Final R indexes [I > 2σ (I)]	R1 = 0.0233, wR2 = 0.0593
Final R indexes [all data]	R1 = 0.0241, wR2 = 0.0599
Largest diff. peak/hole/e ⁻ Å ⁻³	0.23/-0.30

Table 22. Crystal Data and Summary of Cp₂TiBr(OtBu)

Compound	Cp ₂ TiBr(OtBu) (4)
Empirical formula	C ₁₄ H ₁₉ BrOTi
Formula weight	331.08
Color of compound	yellow
Temperature/K	100
Crystal system	monoclinic
Space group	<i>P</i> 2 ₁ / <i>c</i>
<i>a</i> /Å	15.0669(4)
<i>b</i> /Å	12.2725(3)
<i>c</i> /Å	15.5128(4)
α /°	90
β /°	90.079(2)
γ /°	90
Volume/Å ³	2868.44(12)
<i>Z</i>	8
ρ_{calc} g/cm ³	1.380
μ /mm ⁻¹	3.365
<i>F</i> (000)	1344
Crystal size/mm ³	0.37 × 0.27 × 0.19
Radiation	MoK α (λ = 0.71073)
2 Θ range for data collect/°	3.762 to 28.415
Index ranges	-20 ≤ <i>h</i> ≤ 20, -16 ≤ <i>k</i> ≤ 16, -19 ≤ <i>l</i> ≤ 21
Reflections collected	26 410
Independent reflections	6965 [<i>R</i> _{int} = 0.0254, <i>R</i> _{sigma} = 0.0150]
Data/restraints/parameters	6965/25/355
Goodness-of-fit on <i>F</i> ²	0.986
Final <i>R</i> indexes [<i>I</i> > 2 σ (<i>I</i>)]	<i>R</i> 1 = 0.0485, <i>wR</i> 2 = 0.1165
Final <i>R</i> indexes [all data]	<i>R</i> 1 = 0.0618, <i>wR</i> 2 = 0.1285
Largest diff. peak/hole/e ⁻ Å ⁻³	0.23/-0.30

Table 23. Crystal Data and Summary of CpTiBr₂(OtBu)

Compound	CpTiBr ₂ (OtBu) (5)
Empirical formula	C ₉ H ₁₄ Br ₂ OTi
Formula weight	345.92
Color of compound	yellow
Temperature/K	100
Crystal system	monoclinic
Space group	<i>P</i> 2 ₁ / <i>c</i>
<i>a</i> /Å	12.9173(2)
<i>b</i> /Å	16.12491(19)
<i>c</i> /Å	12.6854(2)
α /°	90
β /°	111.141(2)
γ /°	90
Volume/Å ³	2464.42(7)
<i>Z</i>	8
ρ_{calc} g/cm ³	1.865
μ /mm ⁻¹	13.187
<i>F</i> (000)	1344
Crystal size/mm ³	0.32 × 0.17 × 0.034
Radiation	CuK α (λ = 1.54184)
2 Θ range for data collect/°	7.338 to 144.476
Index ranges	-15 ≤ <i>h</i> ≤ 15, -19 ≤ <i>k</i> ≤ 19, -11 ≤ <i>l</i> ≤ 15
Reflections collected	23 134
Independent reflections	4810 [<i>R</i> _{int} = 0.0450, <i>R</i> _{sigma} = 0.0264]
Data/restraints/parameters	4810/0/241
Goodness-of-fit on <i>F</i> ²	1.083
Final <i>R</i> indexes [<i>I</i> > 2 σ (<i>I</i>)]	<i>R</i> 1 = 0.0312, w <i>R</i> 2 = 0.0812
Final <i>R</i> indexes [all data]	<i>R</i> 1 = 0.0322, w <i>R</i> 2 = 0.0824
Largest diff. peak/hole/e Å ⁻³	1.20/-0.73

Table 29. Fractional coordinates and equivalent isotropic displacement parameters (\AA^2) for $\text{Cp}_2\text{TiCl}(\text{OtBu})$. U_{eq} is defined as one third of the trace of the orthogonalized U_{ij} tensor.

	<i>x</i>	<i>y</i>	<i>z</i>	U_{eq}
Ti1	0.61171(2)	0.33795(2)	0.31709(2)	0.01119(8)
Cl1	0.60104(2)	0.53713(3)	0.28704(2)	0.02323(9)
O1	0.70849(6)	0.35158(7)	0.38327(6)	0.01702(19)
C11	0.77801(8)	0.35893(11)	0.44513(8)	0.0171(3)
C2	0.61645(9)	0.34300(12)	0.16011(9)	0.0214(3)
H2	0.5909	0.4032	0.1306	0.026
C7	0.46893(9)	0.39049(12)	0.38030(9)	0.0235(3)
H7	0.4433	0.4604	0.3687	0.028
C3	0.70541(9)	0.33782(12)	0.19036(8)	0.0217(3)
H3	0.7483	0.394	0.1847	0.026
C9	0.54996(9)	0.25156(12)	0.44341(8)	0.0207(3)
H9	0.5873	0.2129	0.481	0.025
C5	0.63521(10)	0.17571(12)	0.22810(9)	0.0243(3)
H5	0.6236	0.1057	0.2527	0.029
C14	0.81068(10)	0.24013(13)	0.46433(10)	0.0289(3)
H14A	0.7624	0.1959	0.4869	0.043
H14B	0.8579	0.2434	0.506	0.043
H14C	0.8323	0.2061	0.4122	0.043
C12	0.85143(10)	0.43144(15)	0.40571(10)	0.0327(3)
H12A	0.8723	0.3968	0.3535	0.049
H12B	0.8999	0.4379	0.4458	0.049
H12C	0.8283	0.5052	0.393	0.049
C10	0.50569(9)	0.20487(12)	0.37206(9)	0.0218(3)
H10	0.5091	0.1303	0.3537	0.026
C8	0.52823(9)	0.36639(12)	0.44817(9)	0.0215(3)
H8	0.5492	0.4175	0.4889	0.026
C6	0.45517(8)	0.29112(13)	0.33332(9)	0.0230(3)
H6	0.419	0.2835	0.285	0.028
C13	0.74270(9)	0.41406(12)	0.52714(9)	0.0233(3)
H13A	0.7184	0.4869	0.5135	0.035
H13B	0.7905	0.4226	0.5678	0.035
H13C	0.697	0.3674	0.5517	0.035
C4	0.71695(9)	0.23333(13)	0.23020(8)	0.0238(3)
H4	0.7697	0.2064	0.254	0.029
C1	0.57381(9)	0.24289(13)	0.18200(8)	0.0222(3)
H1	0.5154	0.2236	0.1687	0.027

Table 30. Fractional coordinates and equivalent isotropic displacement parameters (\AA^2) for $\text{Cp}_2\text{TiBr}(\text{OtBu})$. U_{eq} is defined as one third of the trace of the orthogonalized U_{ij} tensor.

	<i>x</i>	<i>y</i>	<i>z</i>	U_{eq}
Br2	0.11158(4)	0.04079(3)	0.22090(4)	0.04717(16)
Ti2	0.11819(4)	-0.16384(5)	0.18357(4)	0.01780(14)
O2	0.21443(19)	-0.1462(2)	0.11896(18)	0.0276(6)
C15	0.2107(3)	-0.1728(4)	0.3094(3)	0.0406(11)
H15	0.2552	-0.1187	0.3162	0.049
C16	0.2202(3)	-0.2708(5)	0.2673(3)	0.0467(13)
H16	0.2733	-0.2974	0.2418	0.056
C17	0.1385(4)	-0.3244(4)	0.2684(3)	0.0450(13)
H17	0.1253	-0.3919	0.2413	0.054
C18	0.0796(3)	-0.2607(4)	0.3166(3)	0.0335(9)
H18	0.02	-0.2787	0.3304	0.04
C19	0.1239(3)	-0.1672(4)	0.3403(2)	0.0346(9)
H19	0.0994	-0.1086	0.3724	0.041
C20	0.0118(3)	-0.2861(4)	0.1258(3)	0.0437(12)
H20	0.0153	-0.3602	0.1432	0.052
C21	-0.0361(3)	-0.2085(5)	0.1647(3)	0.0473(13)
H21	-0.0733	-0.2199	0.2132	0.057
C22	-0.0239(4)	-0.1107(5)	0.1246(5)	0.074(2)
H22	-0.0493	-0.0425	0.1398	0.089
C23	0.0373(4)	-0.1337(5)	0.0529(4)	0.068(2)
H23	0.0598	-0.0832	0.0119	0.082
C24	0.0546(4)	-0.2416(5)	0.0576(3)	0.0527(14)
H24	0.0915	-0.2806	0.0187	0.063
C25	0.2838(3)	-0.1227(4)	0.0596(3)	0.0358(10)
C26	0.2417(7)	-0.0670(8)	-0.0189(6)	0.043(3)
H26A	0.1937	-0.1127	-0.0415	0.065
H26B	0.2868	-0.0565	-0.0636	0.065
H26C	0.2176	0.004	-0.0017	0.065
C27	0.3118(8)	-0.2409(9)	0.0255(8)	0.053(3)
H27A	0.3424	-0.2807	0.0716	0.08
H27B	0.3516	-0.2332	-0.0241	0.08
H27C	0.2586	-0.2813	0.0081	0.08
C28	0.3470(8)	-0.0630(14)	0.1030(8)	0.060(4)
H28A	0.3196	0.0028	0.127	0.09
H28B	0.3944	-0.0422	0.063	0.09
H28C	0.3719	-0.107	0.1498	0.09
C26B	0.2761(6)	0.0055(8)	0.0348(6)	0.039(3)
H26D	0.2246	0.0167	-0.0028	0.058
H26E	0.3301	0.0286	0.0047	0.058
H26F	0.2689	0.0486	0.0875	0.058
C27B	0.2852(8)	-0.1900(10)	-0.0129(8)	0.049(3)
H27D	0.2918	-0.2661	0.0052	0.074
H27E	0.3351	-0.1697	-0.0499	0.074
H27F	0.2295	-0.1816	-0.045	0.074
C28B	0.3770(7)	-0.1231(9)	0.1092(7)	0.037(2)
H28D	0.3746	-0.0722	0.1578	0.055

Table 30 (cont.)

	<i>x</i>	<i>y</i>	<i>z</i>	<i>U_{eq}</i>
H28E	0.4242	-0.1008	0.0695	0.055
H28F	0.3894	-0.1966	0.1307	0.055
Ti1	0.38564(5)	0.34599(6)	0.17061(4)	0.02222(15)
O1	0.29249(19)	0.3597(2)	0.10142(17)	0.0264(6)
C1	0.4789(3)	0.3446(5)	0.0446(3)	0.0475(13)
H1	0.467	0.3955	-0.0001	0.057
C2	0.5351(3)	0.3605(4)	0.1141(4)	0.0452(12)
H2	0.5695	0.4241	0.1245	0.054
C3	0.5330(3)	0.2703(4)	0.1654(3)	0.0388(11)
H3	0.5658	0.2602	0.2171	0.047
C4	0.4745(3)	0.1954(4)	0.1289(3)	0.0442(12)
H4	0.4585	0.1262	0.1514	0.053
C5	0.4438(3)	0.2432(5)	0.0517(3)	0.0515(14)
H5	0.4049	0.2098	0.0113	0.062
C6	0.3841(4)	0.3741(5)	0.3239(3)	0.0580(14)
H6	0.4198	0.4309	0.3468	0.07
C7	0.4048(4)	0.2666(5)	0.3115(3)	0.0566(15)
H7	0.4595	0.2363	0.3304	0.068
C8	0.3435(6)	0.2072(6)	0.2712(4)	0.086(2)
H8	0.3481	0.1341	0.2514	0.103
C9	0.2744(4)	0.2742(6)	0.2651(4)	0.0616(16)
H9	0.2184	0.2506	0.2438	0.074
C10	0.2886(4)	0.3789(5)	0.2913(3)	0.0537(14)
H10	0.2491	0.4392	0.2897	0.064
C11	0.2226(3)	0.3729(4)	0.0415(3)	0.0374(10)
C12	0.1906(4)	0.2622(6)	0.0161(5)	0.0733(19)
H12A	0.2393	0.2215	-0.0104	0.11
H12B	0.1417	0.2693	-0.0252	0.11
H12C	0.1698	0.2233	0.0674	0.11
C13	0.1514(4)	0.4413(7)	0.0836(4)	0.079(2)
H13A	0.1249	0.4005	0.1314	0.118
H13B	0.1054	0.4588	0.0411	0.118
H13C	0.1777	0.5089	0.1055	0.118
C14	0.2603(4)	0.4311(5)	-0.0372(3)	0.0602(17)
H14A	0.2859	0.5011	-0.0195	0.09
H14B	0.2127	0.4439	-0.0791	0.09
H14C	0.3065	0.3859	-0.0635	0.09
Br1	0.42211(12)	0.54688(18)	0.1836(2)	0.0439(4)
Br1B	0.4017(5)	0.5624(3)	0.1540(5)	0.0517(15)

Table 31. Fractional coordinates and equivalent isotropic displacement parameters (\AA^2) for $\text{CpTiBr}_2(\text{OtBu})$. U_{eq} is defined as one third of the trace of the orthogonalized U_{ij} tensor.

	<i>x</i>	<i>y</i>	<i>z</i>	U_{eq}
Br1	0.27514(2)	0.15854(2)	0.18899(3)	0.02922(9)
Br2	0.58998(2)	0.18029(2)	0.30319(2)	0.02675(9)
Ti1	0.42794(3)	0.20252(3)	0.13282(4)	0.01887(11)
O1	0.41448(16)	0.30913(11)	0.13167(17)	0.0252(4)
C1	0.3401(3)	0.1547(3)	-0.0509(3)	0.0495(10)
H1	0.2654	0.167	-0.0882	0.059
C2	0.3837(3)	0.0830(2)	0.0148(3)	0.0401(8)
H2	0.3426	0.0392	0.0272	0.048
C3	0.4980(2)	0.08982(18)	0.0573(3)	0.0310(6)
H3	0.5472	0.0512	0.1034	0.037
C4	0.5274(2)	0.16482(18)	0.0191(3)	0.0308(6)
H4	0.5992	0.1849	0.0367	0.037
C5	0.4306(3)	0.2039(2)	-0.0494(3)	0.0425(8)
H5	0.4264	0.2538	-0.0876	0.051
C6	0.4002(2)	0.39787(16)	0.1179(3)	0.0259(6)
C7	0.5011(3)	0.43702(18)	0.2066(3)	0.0362(7)
H7A	0.5059	0.4191	0.2804	0.054
H7B	0.4944	0.4963	0.2018	0.054
H7C	0.5669	0.4204	0.1936	0.054
C8	0.3916(3)	0.41967(19)	-0.0010(3)	0.0361(7)
H8A	0.4589	0.4041	-0.0116	0.054
H8B	0.3801	0.4783	-0.0126	0.054
H8C	0.3302	0.3904	-0.0543	0.054
C9	0.2945(3)	0.4187(2)	0.1388(3)	0.0423(8)
H9A	0.233	0.3901	0.0848	0.063
H9B	0.2816	0.4774	0.1311	0.063
H9C	0.302	0.4018	0.2138	0.063
Br1B	1.05174(2)	0.15632(2)	0.72324(2)	0.02427(9)
Br2B	0.74003(2)	0.15356(2)	0.61147(2)	0.02563(9)
Ti1B	0.89589(3)	0.19224(2)	0.77918(4)	0.01669(11)
O1B	0.90068(14)	0.29934(10)	0.77113(16)	0.0209(4)
C1B	0.9792(2)	0.1730(2)	0.9737(2)	0.0311(6)
H1B	1.0442	0.2019	1.0123	0.037
C2B	0.9718(3)	0.09300(19)	0.9256(3)	0.0344(7)
H2B	1.0314	0.0594	0.9287	0.041
C3B	0.8591(3)	0.07310(17)	0.8724(3)	0.0319(6)
H3B	0.8305	0.0244	0.8335	0.038
C4B	0.7973(2)	0.14073(18)	0.8889(2)	0.0273(6)
H4B	0.7203	0.1445	0.8618	0.033
C5B	0.8706(2)	0.20093(17)	0.9525(2)	0.0273(6)
H5B	0.851	0.251	0.9766	0.033
C6B	0.9195(2)	0.38764(15)	0.7867(2)	0.0206(5)
C7B	0.8273(2)	0.42923(16)	0.6907(2)	0.0269(6)
H7BA	0.8307	0.4116	0.6198	0.04
H7BB	0.8361	0.4883	0.6975	0.04
H7BC	0.7567	0.4141	0.6943	0.04

Table 31 (cont.)

	x	y	z	U_{eq}
C8B	0.9159(2)	0.41129(16)	0.9009(2)	0.0262(5)
H8BA	0.8448	0.3969	0.9037	0.039
H8BB	0.9276	0.4699	0.9122	0.039
H8BC	0.9731	0.382	0.9593	0.039
C9B	1.0328(2)	0.40473(18)	0.7804(3)	0.0332(6)
H9BA	1.0885	0.3745	0.839	0.05
H9BB	1.0485	0.463	0.7901	0.05
H9BC	1.0331	0.3875	0.708	0.05

Table 32. Fractional coordinates and equivalent isotropic displacement parameters (\AA^2) for $\text{Cp}_2\text{TiCl}(\text{OiPr})$. U_{eq} is defined as one third of the trace of the orthogonalized U_{ij} tensor.

	<i>x</i>	<i>y</i>	<i>z</i>	U_{eq}
Ti1	0.59459(6)	0.25	0.68971(8)	0.0336(2)
Cl1	0.42875(10)	0.25	0.57917(19)	0.0629(4)
O1	0.6640(3)	0.25	0.5229(3)	0.0517(9)
C7	0.6640(5)	0.25	0.2696(5)	0.0605(15)
H7A	0.5918	0.2295	0.271	0.091
H7B	0.6966	0.2072	0.1901	0.091
H7C	0.6722	0.3397	0.2584	0.091
C8	0.8261(4)	0.25	0.4145(7)	0.0646(16)
H8A	0.8302	0.3395	0.3978	0.097
H8B	0.8641	0.2062	0.3406	0.097
H8C	0.8551	0.2306	0.5076	0.097
C1B	0.6945(18)	0.413(2)	0.809(3)	0.054(5)
H1B	0.763	0.3923	0.8279	0.064
C2B	0.610(2)	0.391(3)	0.893(4)	0.051(6)
H2B	0.6125	0.3576	0.986	0.062
C3B	0.524(2)	0.424(2)	0.829(2)	0.055(5)
H3B	0.4586	0.4097	0.8661	0.066
C4B	0.546(2)	0.4819(15)	0.696(2)	0.047(4)
H4B	0.5003	0.5183	0.6302	0.056
C5B	0.655(2)	0.4709(16)	0.690(2)	0.051(5)
H5B	0.6944	0.5002	0.6128	0.061
C1	0.6937(8)	0.4323(10)	0.7186(12)	0.054(2)
H1	0.7568	0.4394	0.6711	0.065
C2	0.6764(10)	0.3808(9)	0.8558(11)	0.050(2)
H2	0.7269	0.3462	0.9155	0.06
C3	0.5719(10)	0.3892(16)	0.8896(17)	0.052(3)
H3	0.5399	0.3626	0.9745	0.062
C4	0.5262(7)	0.4445(8)	0.7727(16)	0.055(3)
H4	0.456	0.4621	0.7652	0.066
C5	0.5983(11)	0.4706(7)	0.6671(11)	0.056(2)
H5	0.5852	0.5075	0.5774	0.067
C6	0.7132(5)	0.2082(6)	0.4105(6)	0.0403(14)
H6	0.7117	0.1155	0.4135	0.048

A4

Crystallographic data of $\text{K}[\text{Be}(\text{1,3}-(\text{SiMe}_3)_2\text{C}_3\text{H}_3)_3]$ Table 24. Crystal Data and Summary for $\text{K}[\text{Be}(\text{1,3}-(\text{SiMe}_3)_2\text{C}_3\text{H}_3)_3]$

Empirical formula	$\text{C}_{27}\text{H}_{63}\text{BeKSi}_6$	
Formula weight	604.42	
Temperature	100.0(5) K	
Wavelength	0.71073 Å	
Crystal system	triclinic	
Space group	$P\bar{1}$	
Unit cell dimensions	$a = 11.936(3)$ Å	$\alpha = 80.165(5)^\circ$
	$b = 13.097(3)$ Å	$\beta = 73.087(5)^\circ$
	$c = 13.758(3)$ Å	$\gamma = 89.739(5)^\circ$
Volume	$2025.3(9)$ Å ³	
Z	2	
Density (calculated)	0.991 Mg/m ³	
Absorption coefficient	0.322 mm ⁻¹	
$F(000)$	664	
Crystal color, morphology	colorless, plate	
Crystal size	$0.20 \times 0.20 \times 0.08$ mm ³	
Theta range for data collection	2.00 to 25.74°	
Index ranges	$-14 \leq h \leq 14, -15 \leq k \leq 15, -16 \leq l \leq 16$	
Reflections collected	23 415	
Independent reflections	7725 [$R(\text{int}) = 0.1195$]	
Observed reflections	4292	
Completeness to $\theta = 25.74^\circ$	99.7%	
Absorption correction	Multi-scan	
Max. and min. transmission	0.7453 and 0.6317	
Refinement method	Full-matrix least-squares on F^2	
Data / restraints / parameters	7725 / 0 / 370	
Goodness-of-fit on F^2	0.965	
Final R indices [$I > 2\sigma(I)$]	$R1 = 0.0588, wR2 = 0.1071$	
R indices (all data)	$R1 = 0.1280, wR2 = 0.1326$	
Largest diff. peak and hole	0.364 and -0.336 e ⁻ Å ⁻³	

REFERENCES

1. D. Brindle, I., Editorial. *Green Chemistry* **1999**, *1* (6), G155-G157.
2. Dadabhoy, A.; Göllitz, P., Sustainability: Chemistry Is Key. *ChemSusChem* **2008**, *1* (1-2), 4-5.
3. Allen, D., Welcome to ACS Sustainable Chemistry & Engineering. *ACS Sustainable Chemistry & Engineering* **2013**, *1* (1), 1-1.
4. Wilke, G.; Bogdanović, B.; Hardt, P.; Heimbach, P.; Keim, W.; Kröner, M.; Oberkirch, W.; Tanaka, K.; Steinrücke, E.; Walter, D.; Zimmermann, H., Allyl-Transition Metal Systems. *Angewandte Chemie International Edition in English* **1966**, *5* (2), 151-164.
5. Quisenberry, K. T.; Smith, J. D.; Voehler, M.; Stec, D. F.; Hanusa, T. P.; Brennessel, W. W., Trimethylsilylated Allyl Complexes of Nickel. The Stabilized Bis(π -allyl)nickel Complex $[\eta^3\text{-}1,3\text{-(SiMe}_3\text{)}_2\text{C}_3\text{H}_3\text{]}_2\text{Ni}$ and Its Mono(π -allyl)NiX (X = Br, I) Derivatives. *Journal of the American Chemical Society* **2005**, *127* (12), 4376-4387.
6. Chmely, S. C.; Carlson, C. N.; Hanusa, T. P.; Rheingold, A. L., Classical versus Bridged Allyl Ligands in Magnesium Complexes: The Role of Solvent. *Journal of the American Chemical Society* **2009**, *131* (18), 6344-6345.
7. Chmely, S. C.; Hanusa, T. P.; Brennessel, W. W., Bis(1,3-trimethylsilylallyl)beryllium. *Angewandte Chemie International Edition* **2010**, *49* (34), 5870-5874.
8. Lichtenberg, C.; Robert, D.; Spaniol, T. P.; Okuda, J., Bis(allyl)aluminum Cation, Tris(allyl)aluminum, and Tetrakis(allyl)aluminate: Synthesis, Characterization, and Reactivity. *Organometallics* **2010**, *29* (21), 5714-5721.
9. Burkey, D. J.; Alexander, E. K.; Hanusa, T. P., Encapsulated Alkaline-Earth Metallocenes. 5. Kinetic Stabilization of Mono[Tetraisopropylcyclopentadienyl]calcium Complexes. *Organometallics* **1994**, *13* (7), 2773-2786.
10. Harvey, Melanie J.; Quisenberry, Keith T.; Hanusa, Timothy P.; Young Jr, Victor G., A Homologous Series of Base-Free Organo(alkaline-earth) Metallocenes: Synthesis and Molecular Structures of $[1,2,4\text{-(SiMe}_3\text{)}_3\text{C}_5\text{H}_2\text{]}_2\text{(Ca, Sr, Ba)}$. *European Journal of Inorganic Chemistry* **2003**, *2003* (18), 3383-3390.
11. Eaborn, C.; Hitchcock, P., The first structurally characterised solvent-free $[\sigma\text{-}C\text{(SiMe}_3\text{)}_3\text{]}_2$ -bonded diorganocalcium, $\text{Ca}[\text{C}(\text{SiMe}_3)_3]_2$. *Chemical Communications* **1997**, (20), 1961-1962.
12. Sartori, A.; El Habra, N.; De Zorzi, C.; Sitran, S.; Casarin, M.; Cavinato, G.; Sada, C.; Gerbasi, R.; Rossetto, G., Zirconocene Alkoxides, Promising Precursors for MOCVD of Zirconium Dioxide Thin Films. *Chemical Vapor Deposition* **2012**, *18* (4-6), 151-158.
13. Johns, A. M.; Chmely, S. C.; Hanusa, T. P., Solution Interaction of Potassium and Calcium Bis(trimethylsilyl)amides; Preparation of $\text{Ca}[\text{N}(\text{SiMe}_3)_2]_2$ from Dibenzylcalcium. *Inorganic Chemistry* **2009**, *48* (4), 1380-1384.
14. Gren, C. K.; Hanusa, T. P.; Rheingold, A. L., Threefold Cation- π Bonding in Trimethylsilylated Allyl Complexes. *Organometallics* **2007**, *26* (7), 1643-1649.
15. Westerhausen, M., Synthesis and spectroscopic properties of bis(trimethylsilyl)amides of the alkaline-earth metals magnesium, calcium, strontium, and barium. *Inorganic Chemistry* **1991**, *30* (1), 96-101.
16. Arduengo, A. J.; Harlow, R. L.; Kline, M., A stable crystalline carbene. *Journal of the American Chemical Society* **1991**, *113* (1), 361-363.

17. Eller, P. G.; Bradley, D. C.; Hursthouse, M. B.; Meek, D. W., Three Coordination in Metal Complexes. *Coordination Chemistry Reviews* **1977**, *24*, 1-95.
18. Anwender, R., Lanthanide amides. *Top. Curr. Chem.* **1996**, *179* (Organolanthoid Chemistry: Synthesis, Structure, Catalysis), 33-112.
19. Cotton, S. A.; Harrowfield, J. M., Lanthanides: Coordination Chemistry. In *Encyclopedia of Inorganic and Bioinorganic Chemistry*, John Wiley & Sons, Ltd: 2011.
20. Rees, W. S., Alkaline Earth Metals: Inorganic Chemistry. In *Encyclopedia of Inorganic and Bioinorganic Chemistry*, John Wiley & Sons, Ltd: 2011.
21. Naglav, D.; Neumann, A.; Blaser, D.; Wolper, C.; Haack, R.; Jansen, G.; Schulz, S., Bonding situation in Be[N(SiMe₃)₂]₂ - an experimental and computational study. *Chemical Communications* **2015**, *51* (18), 3889-3891.
22. Westerhausen, M., Synthesis, properties, and reactivity of alkaline earth metal bis[bis(trialkylsilyl)amides]. *Coordination Chemistry Reviews* **1998**, *176*, 157-210.
23. Faller, J. W.; Anderson, A. S., Organometallic conformational equilibria. XI. cis-trans Isomerism and stereochemical nonrigidity in cyclopentadienylmolybdenum complexes. *Journal of the American Chemical Society* **1970**, *92* (20), 5852-5860.
24. James, S. L.; Adams, C. J.; Bolm, C.; Braga, D.; Collier, P.; Friscic, T.; Grepioni, F.; Harris, K. D. M.; Hyett, G.; Jones, W.; Krebs, A.; Mack, J.; Maini, L.; Orpen, A. G.; Parkin, I. P.; Shearouse, W. C.; Steed, J. W.; Waddell, D. C., Mechanochemistry: opportunities for new and cleaner synthesis. *Chemical Society Reviews* **2012**, *41* (1), 413-447.
25. Rightmire, N. R.; Hanusa, T. P., Advances in organometallic synthesis with mechanochemical methods. *Dalton Transactions* **2016**, *45* (6), 2352-2362.
26. Lappert, M. F.; Protchenko, A.; Power, P. P.; Seeber, A., *Metal Amide Chemistry*. Wiley: Wiltshire, England, 2009.
27. Vehkamäki, M.; Hatanpää, T.; Ritala, M.; Leskelä, M., Bismuth precursors for atomic layer deposition of bismuth-containing oxide films. *J. Mater. Chem.* **2004**, *14* (21), 3191-3197.
28. Evans, W. J.; Rego, D. B.; Ziller, J. W., Synthesis and structure of the cyclic amido bismuth imide, {[Me₃Si]N}Bi[μ-N(SiMe₃)]₂, via loss of SiMe₃ from a [N(SiMe₃)₂]₁-ligand. *Inorg. Chim. Acta* **2007**, *360* (4), 1349-1353.
29. Liu, W.; Chang, A. Y.; Schaller, R. D.; Talapin, D. V., Colloidal InSb Nanocrystals. *J. Am. Chem. Soc.* **2012**, *134* (Copyright (C) 2013 American Chemical Society (ACS). All Rights Reserved.), 20258-20261.
30. Kim, C.-K.; Khang, Y.-H.; Lee, T.-Y. Phase-change random access memory and method of manufacturing the same. US20090050869A1, 2009.
31. Shin, W.-C.; Khang, Y.-H. Method of forming phase change material thin film, and simplified method of manufacturing phase change memory device using the same with improved memory characteristics. EP1806427A2, 2007.
32. Lee, J.-H.; Park, Y.-S.; Park, S.-H. Hexa(trimethylsilyl) antimony triamine precursor for manufacture of Ge₂-Sb₂-Te₅ phase-change films for RAM memory devices. US20060049447A1, 2006.
33. Seo, B.-S.; Lee, J.-H. Ge precursor, Ge-Sb-Te thin layer, phase-change memory device. EP1675194A2, 2006.
34. Bochmann, M.; Song, X.; Hursthouse, M. B.; Karaulov, A., Chalcogenolato complexes of bismuth and antimony. Syntheses, thermolysis reactions, and crystal structure of

Sb(SC₆H₂Pri_{3-2,4,6})₃. *J. Chem. Soc., Dalton Trans.* **1995**, (Copyright (C) 2013 American Chemical Society (ACS). All Rights Reserved.), 1649-52.

35. Olmstead, M. M.; Power, P. P.; Sigel, G. A., Unusual bonding in the secondary aminophosphine [HP{N(SiMe₃)₂}₂]₂: x-ray structures and NMR and IR studies of the main Group V amino compounds HE(NR₂)₂ (E = P, As, R = SiMe₃; E = P, R = Ph). *Inorg. Chem.* **1988**, *27* (12), 2045-2049.

36. Gynane, M. J. S.; Hudson, A.; Lappert, M. F.; Power, P. P.; Goldwhite, H., Bulky alkyls, amides, and aryloxides of main Group 5 elements. Part 1. Persistent phosphinyl and arsinyl radicals [middle dot]MRR[prime or minute] and their chloroprecursors MRR[prime or minute]Cl and related compounds. *J. Chem. Soc., Dalton Trans.* **1980**, *0* (12), 2428-2433.

37. Michalik, D.; Schulz, A.; Villinger, A., Lewis-Acid-Assisted Methyl Exchange Reactions In Silylated Aminodichloroarsanes. *Inorg. Chem.* **2008**, *47* (24), 11798-11806.

38. Flynn, K. M.; Murray, B. D.; Olmstead, M. M.; Power, P. P., Interaction of phosphorous bis(trimethylsilyl)amide dichloride with carbonylmetalate dianions of iron and chromium: syntheses and x-ray crystal structures of new transition metal complexes involving phosphorus and arsenic in multiple bonding. *J. Am. Chem. Soc.* **1983**, *105* (25), 7460-7461.

39. Avtomonov, E. V.; Megges, K.; Li, X.; Lorberth, J.; Wocadlo, S.; Massa, W.; Harms, K.; Churakov, A. V.; Howard, J. A. K., Syntheses and structures of cyclopentadienyl arsenic compounds II. Pentamethyl- and tetraisopropylcyclopentadienyl arsenic amido derivatives. *J. Organomet. Chem.* **1997**, *544* (1), 79-89.

40. Hering, C.; Schulz, A.; Villinger, A., Low-Temperature Isolation of An Azidophosphenium Cation. *Angew. Chem. Int. Ed.* **2012**, *51* (25), 6241-6245.

41. Pohl, S.; Krebs, B., The crystal and molecular structure of [bis(trimethylsilyl)amino]bis(trimethylsilylimino)phosphorane. *Chem. Ber.* **1977**, *110* (Copyright (C) 2013 American Chemical Society (ACS). All Rights Reserved.), 3183-3189.

42. Appel, R.; Gudat, D.; Niecke, E.; Nieger, M.; Porz, C.; Westermann, H., Synthesis and structure of amino-substituted tetraphosphetanes. *Z. Naturforsch., B: Chem. Sci.* **1991**, *46* (Copyright (C) 2013 American Chemical Society (ACS). All Rights Reserved.), 865-83.

43. Perrin, L.; Maron, L.; Eisenstein, O.; Lappert, M. F., [gamma] Agostic C-H or [small beta] agostic Si-C bonds in La{CH(SiMe₃)₂}₃? A DFT study of the role of the ligand. *New J. Chem.* **2003**, *27* (1), 121-127.

44. Brady, E. D.; Clark, D. L.; Gordon, J. C.; Hay, P. J.; Keogh, D. W.; Poli, R.; Scott, B. L.; Watkin, J. G., Tris(bis(trimethylsilyl)amido)samarium: X-ray Structure and DFT Study. *Inorg. Chem.* **2003**, *42* (21), 6682-6690.

45. Brookhart, M.; Green, M. L. H., *J. Organomet. Chem.* **1983**, *250*, 395-408.

46. Comment173, Strict defomotopm of agpstoc. *In much of the literature on the subject, M...Si-C interactions are often termed "agostic"; this term, however, properly and specifically refers only to 3-center-2-electron M...H-C interactions.*¹⁸ We maintain this distinction here. 48.

47. Cooper, A. C.; Clot, E.; Huffman, J. C.; Streib, W. E.; Maseras, F.; Eisenstein, O.; Caulton, K. G., Computational and Experimental Test of Steric Influence on Agostic Interactions: A Homologous Series for Ir(III). *J. Am. Chem. Soc.* **1998**, *121* (1), 97-106.

48. Jaffart, J.; Cole, M. L.; Etienne, M.; Reinhold, M.; McGrady, J. E.; Maseras, F., C-H and C-C agostic interactions in cycloalkyl tris(pyrazolyl)boratoniobium complexes. *Dalton Transactions* **2003**, (21), 4057-4064.

49. Ujaque, G.; Cooper, A. C.; Maseras, F.; Eisenstein, O.; Caulton, K. G., Computational Evidence of the Importance of Substituent Bulk on Agostic Interactions in Ir(H)₂(PtBu₂Ph)₂⁺. *J. Am. Chem. Soc.* **1998**, *120* (2), 361-365.
50. Clot, E.; Eisenstein, O., Agostic Interactions from a Computational Perspective: One Name, Many Interpretations. In *Principles and Applications of Density Functional Theory in Inorganic Chemistry II*, Springer Berlin Heidelberg: 2004; Vol. 113, pp 1-36.
51. Spicer, C. W.; Lovitt, C. F.; Girolami, G. S., Nonagostic M··H-C Interactions. Synthesis, Characterization, and DFT Study of the Titanium Amide Ti₂Cl₆[N(t-Bu)₂]₂. *Organometallics* **2012**, *31* (13), 4894-4903.
52. Niecke, E.; Flick, W.; Pohl, S., A Phosphorus(III) Derivative with Sterically Fixed Bis(trimethylsilyl)amino Groups. *Angew. Chem. Int. Ed. Engl.* **1976**, *15* (5), 309-310.
53. Cordero, B.; Gomez, V.; Platero-Prats, A. E.; Reves, M.; Echeverria, J.; Cremades, E.; Barragan, F.; Alvarez, S., Covalent radii revisited. *Dalton Trans.* **2008**, (21), 2832-2838.
54. Comment166, Relative occupancy of As and As' sites. *The crystallographic results reported here are from a crystal that displayed merohedral twinning in a 60:40 ratio. Twinning need not be constant from crystal to crystal, and in fact is not in this case: examination of a second crystal revealed a twinning ratio of 68:32. Such variability does not affect any of the conclusions.*
55. F. Moser, D.; Schranz, I.; C. Gerrety, M.; Stahl, L.; J. Staples, R., Polycyclic bis(amido)cyclodiphosphazane complexes of antimony(III) and bismuth(III): syntheses, molecular structures and solution behaviour. *J. Chem. Soc., Dalton Trans.* **1999**, 0 (5), 751-758.
56. Diel, B. N.; Huber, T. L.; Ambacher, W. G., Synthesis and characterization of the first examples of 1,3,2-diazastibole and 1,3,2-diazabismole ring compounds. *Heteroatom Chem.* **1999**, *10* (5), 423-429.
57. Burford, N.; Macdonald, C. L. B.; Robertson, K. N.; Cameron, T. S., Synthesis and Structures of Sb[N(H)(C₆H₂tBu₃)]₃ and Bi[N(H)(C₆H₂tBu₃)]₃: Implications for the Steric Limits of Supermesityl Substitution. *Inorg. Chem.* **1996**, *35* (13), 4013-4016.
58. Shutov, P. L.; Karlov, S. S.; Harms, K.; Sundermeyer, J.; Lorberth, J.; Zaitseva, G. S., Intramolecular nucleophilic substitution in C₆F₅ moiety. The fluoride-dialkylamino exchange in decafluorodiphenlamino moiety. *J. Fluor. Chem.* **2009**, *130* (11), 1017-1021.
59. Bartell, L. S.; Hirst, R. C., Electron Diffraction Study of the Structure of Phosphine. *J. Chem. Phys.* **1959**, *31* (2), 449-451.
60. Jerzembeck, W.; Bürger, H.; Constantin, L.; Margulès, L.; Demaison, J.; Breidung, J.; Thiel, W., Bismuthine BiH₃: Fact or Fiction? High-Resolution Infrared, Millimeter-Wave, and Ab Initio Studies. *Angew. Chem. Int. Ed.* **2002**, *41* (14), 2550-2552.
61. Dunne, B. J.; Orpen, A. G., Triphenylphosphine: a redetermination. *Acta Crystallogr. Sect. C* **1991**, *47* (2), 345-347.
62. Hawley, D. M.; Ferguson, G., The stereochemistry of some organic derivatives of Group VB elements. The crystal and molecular structure of triphenylbismuth. *J. Chem. Soc. A* **1968**, 0 (0), 2059-2063.
63. Guzei, I. A.; Wendt, M., An improved method for the computation of ligand steric effects based on solid angles. *Dalton Trans.* **2006**, (33), 3991-3999.
64. Pauling, L., *The Nature of the Chemical Bond*. 3rd. ed.; Cornell University Press: Ithaca, 1960.

65. Westerhausen, M.; Hartmann, M.; Pfitzner, A.; Schwarz, W., Bis(trimethylsilyl)amide und -methanide des Yttriums — Molekülstrukturen von Tris(diethylether-O)lithium-(μ -chloro)-tris[bis(trimethylsilyl) methyl]yttriat, solvensfreiem Yttrium-tris[bis(trimethylsilyl)amid] sowie dem Bis(benzonitril)-Komplex. *Z. Anorg. Allg. Chem.* **1995**, *621* (5), 837-850.
66. Scarel, G.; Wiemer, C.; Fanciulli, M.; Fedushkin, I. L.; Fukin, G. K.; Domrachev, G. A.; Lebedinskii, Y.; Zenkevich, A.; Pavia, G., [(Me₃Si)₂N]₃Lu: Molecular Structure and Use as Lu and Si Source for Atomic Layer Deposition of Lu Silicate Films. *Z. Anorg. Allg. Chem.* **2007**, *633* (11-12), 2097-2103.
67. Rees, J., William S.; Just, O.; Van Derveer, D. S., Molecular design of dopant precursors for atomic layer epitaxy of SrS:Ce. *J. Mater. Chem.* **1999**, *9* (1), 249-252.
68. Andersen, R. A.; Templeton, D. H.; Zalkin, A., Structure of Tris(bis(trimethylsilyl)amido)neodymium(III), Nd[N(Si(CH₃)₃)₂]₃. *Inorg. Chem.* **1978**, *17*, 2317-2319.
69. Sheng, E.-h.; Yang, G.-s.; Dong, B.-p., Synthesis and crystal structure of three coordinate planar neodymium amide [(Me₃Si)₂N]₃Nd. *Anhui Shifan Daxue Xuebao, Ziran Kexueban* **2002**, *25* (Copyright (C) 2013 American Chemical Society (ACS). All Rights Reserved.), 254-256.
70. Sundermeyer, J.; Khvorost, A.; Harms, K., Tris[bis(trimethylsilyl)amido]samarium tetrahydrofuran solvate. *Acta Crystallogr. Sect. E* **2004**, *60* (8), m1117-m1119.
71. Hitchcock, P. B.; Hulkes, A. G.; Lappert, M. F.; Li, Z., Cerium(III) dialkyl dithiocarbamates from [Ce{N(SiMe₃)₂}]₃ and tetraalkylthiuram disulfides, and [Ce(κ -S₂CNET₂)₄] from the Ce(III) precursor; Tb(III) and Nd(III) analogues. *Dalton Trans.* **2004**, (1), 129-136.
72. Herrmann, W. A.; Anwander, R.; Munck, F. C.; Scherer, W.; Dufaud, V.; Huber, N. W.; Artus, G. R. J., Lanthanoid complexes. IX. Reactivity control of lanthanoid amides through ligand effects. Synthesis and structures of sterically congested alkoxy complexes. *Z. Naturforsch., B: Chem. Sci.* **1994**, *49* (Copyright (C) 2013 American Chemical Society (ACS). All Rights Reserved.), 1789-1797.
73. Niemeyer, M., Synthesis and Structural Characterization of Several Ytterbium Bis(trimethylsilyl)amides Including Base-free [Yb{N(SiMe₃)₂}]₂(μ -Cl)₂ — A Coordinatively Unsaturated Complex with Additional Agostic Yb \cdots (H₃C—Si) Interactions. *Z. Anorg. Allg. Chem.* **2002**, *628* (3), 647-657.
74. Stewart, J. L.; Andersen, R. A., Trivalent uranium chemistry: molecular structure of [(Me₃Si)₂N]₃U. *Polyhedron* **1998**, *17* (5-6), 953-958.
75. Gaunt, A. J.; Enriquez, A. E.; Reilly, S. D.; Scott, B. L.; Neu, M. P., Structural Characterization of Pu[N(SiMe₃)₂]₃, a Synthetically Useful Nonaqueous Plutonium(III) Precursor. *Inorg. Chem.* **2007**, *47* (1), 26-28.
76. Ghotra, J. S.; Hursthouse, M. B.; Welch, A. J., Three-coordinate scandium(III) and europium(III). Crystal and molecular structures of their tris(hexamethyldisilylamide) [complexes]. *J. Chem. Soc., Chem. Commun.* **1973**, (18), 669-670.
77. Brookhart, M.; Green, M. L. H.; Parkin, G., Agostic interactions in transition metal compounds. *Proc. Natl. Acad. Sci. U. S. A.* **2007**, *104* (17), 6908-6914.
78. Schaverien, C. J.; van der Heijden, H.; Orpen, A. G., Monocyclopentadienyl lanthanide chemistry: towards the limits of steric unsaturation. *Polyhedron* **1989**, *8* (13-14), 1850-1852.

79. Van der Heijden, H.; Schaverien, C. J.; Orpen, A. G., The first salt- and solvent-free monocyclopentadienyl lanthanide dialkyl complex. X-ray structure determinations of $\text{La}(\eta\text{-}5\text{-C}_5\text{Me}_5)[\text{CH}(\text{SiMe}_3)_2]_2$ and of its tetrahydrofuran adduct: compounds containing agostic silicon-carbon bonds. *Organometallics* **1989**, 8 (1), 255-258.
80. Schaverien, C. J.; Nesbitt, G. J., Multinuclear magnetic resonance investigation of the fluxionality of $\text{CH}(\text{SiMe}_3)_2$ groups in organolanthanide complexes. *J. Chem. Soc., Dalton Trans.* **1992**, 157-167.
81. Klooster, W. T.; Brammer, L.; Schaverien, C. J.; Budzelaar, P. H. M., C-H Bonds Are Not Elongated by Coordination to Lanthanide Metals: Single-Crystal Neutron Diffraction Structures of $(\text{C}_5\text{Me}_5)\text{Y}(\text{OC}_6\text{H}_3\text{tBu}_2)\text{CH}(\text{SiMe}_3)_2$ at 20 K and $(\text{C}_5\text{Me}_5)\text{La}\{\text{CH}(\text{SiMe}_3)_2\}_2$ at 15 K. *J. Am. Chem. Soc.* **1999**, 121, 1381-1382.
82. Comment179, Si-C bond lengthening in "agostic" interactions. *Maseras and Crabtree*{Maseras, 2004 #9044} have argued that to be properly considered an agostic contact, two criteria must be met: (1) there must be an empty orbital that could overlap with the X-Y bond under consideration (generally associated with a distortion in the metal-ligand geometry); and (2), there must be evidence of weakening of the bond. The latter, they propose, is most easily accessible by calculation. This is especially true given the uncertainties in experimentally measured bond lengths, even when hydrogen is not involved. The $\text{M}[\text{N}(\text{SiMe}_3)_2]_3$ and $\text{M}[\text{CH}(\text{SiMe}_3)_2]_3$ complexes used in this study illustrate the difficulty in establishing statistically significant bond lengthening from X-ray crystal structures. The difference between the length of the Si-Me bond that is oriented toward the metal versus the average of the other two on the SiMe_3 group (ΔSiC) should be a positive number if lengthening (and hence weakening) is occurring. For the Group 15 complexes, ΔSiC is, in fact, either statistically indistinguishable from zero (owing to the esd of the Si-C bond lengths) or even slightly negative; i.e., $\Delta\text{SiC} = -0.017$ in the case of 2. Lengthening is usually observed in the f-element $\text{M}[\text{N}(\text{SiMe}_3)_2]_3$ complexes; it is greatest in $\text{Y}[\text{N}(\text{SiMe}_3)_2]_3$ ($\Delta\text{SiC} = +0.028 \text{ \AA}$), for example, and noticeable in $\text{Sm}[\text{N}(\text{SiMe}_3)_2]_3 \cdot \text{hexane}$ ($+0.013 \text{ \AA}$), but less so in $\text{Sm}[\text{N}(\text{SiMe}_3)_2]_3 \cdot \text{THF}$ ($+0.005 \text{ \AA}$, not significantly different from zero), demonstrating the influence of crystal packing effects on the value. Similarly small, insignificantly positive (or negative) values are found in other complexes, such as $\text{U}[\text{N}(\text{SiMe}_3)_2]_3$ ($+0.005 \text{ \AA}$) and $\text{Er}[\text{N}(\text{SiMe}_3)_2]_3$ (-0.006 \AA). Consequently, the associated S-C bond lengths are not listed in Table 1.
83. Maseras, F.; Crabtree, R. H., $[(\text{C}_5\text{H}_4\text{MeEt})\text{Ir}(\text{PPh}_3)_2]^+$: an agostic C-C bond or a close metal-ligand contact? *Inorg. Chim. Acta* **2004**, 357 (1), 345-346.
84. Avent, A. G.; Caro, C. F.; Hitchcock, P. B.; Lappert, M. F.; Li, Z.; Wei, X.-H., Synthetic and structural experiments on yttrium, cerium and magnesium trimethylsilylmethyls and their reaction products with nitriles; with a note on two cerium [small beta]-diketimines. *Dalton Trans.* **2004**, (10), 1567-1577.
85. Westerhausen, M.; Hartmann, M.; Schwarz, W., Syntheses and structure of dimeric yttrium tris[bis(trimethylsilyl)phosphanide]; x-ray structures of $[(\text{thf})\text{LiCl}(\text{thf})_2\text{LiPtBu}_2]_2$ and $\text{Y}[\text{CH}(\text{SiMe}_3)_2]_3$. *Inorg. Chim. Acta* **1998**, 269 (1), 91-100.
86. Hitchcock, P. B.; Lappert, M. F.; Smith, R. G.; Bartlett, R. A.; Power, P. P., Synthesis and structural characterisation of the first neutral homoleptic lanthanide metal(III) alkyls: $[\text{LnR}_3][\text{Ln} = \text{La or Sm}, \text{R} = \text{CH}(\text{SiMe}_3)_2]$. *J. Chem. Soc., Chem. Commun.* **1988**, (15), 1007-1009.

87. Van der Sluys, W. G.; Burns, C. J.; Sattelberger, A. P., First Example of a Neutral Homoleptic Uranium Alkyl. Synthesis, Properties, and Structure of $U[CH(SiMe_3)_2]_3$. *Organometallics* **1989**, *8*, 855-857.
88. Murray, B.; Hvoslef, J.; Hope, H.; Power, P. P., A compound with severely distorted geometry at ligated carbon: synthesis and x-ray crystal structure of $Bi[CH(SiMe_3)_2]_3$, a trialkylbismuth complex with high thermal stability. *Inorg. Chem.* **1983**, *22* (23), 3421-3424.
89. Rappé, A. K.; Casewit, C. J.; Colwell, K. S.; Goddard, W. A., III; Skiff, W. M., UFF, a full periodic table force field for molecular mechanics and molecular dynamics simulations. *J. Am. Chem. Soc.* **1992**, *114* (25), 10024-10035.
90. Rappé, A. K.; Colwell, K. S.; Casewit, C. J., Application of a universal force field to metal complexes. *Inorg. Chem.* **1993**, *32* (16), 3438-50.
91. Pantazis, D. A.; McGrady, J. E.; Maseras, F.; Etienne, M., Critical Role of the Correlation Functional in DFT Descriptions of an Agostic Niobium Complex. *Journal of Chemical Theory and Computation* **2007**, *3* (4), 1329-1336.
92. Comment176, Dispersion interactions in $Lu(Nstar)_3$. *How much distortion can be ascribed to attractive dispersion forces alone is not easily answered. In a small test, we examined $Lu[N(SiMe_3)_2]_3$ with DFT methods, using both a "dispersion-free" functional (APF; Austin, A.; Petersson, G. A.; Frisch, M. J.; Dobek, F. J.; Scalmani, G.; Throssell, K., J. Chem. Theory Comput. 2012, 8, 4989-5007) and its dispersion-corrected counterpart (APF-D). The uncorrected APF functional (with Stuttgart RSC segmented/ECP on Lu, 6-31G(d,p) on the other atoms) actually performs quite well, with deviations in the Lu-N distances and N-Lu-N angles of 0.027 Å and 3.2°, respectively, from the experimental values. Distances to atoms not directly bonded to the metal are only slightly overestimated (e.g., Lu...C(H3) by 0.05 Å). The dispersion correction contracts both bonded and non-bonded distances, so that the Lu-N distance is underestimated by 0.048 Å, and the Lu...C(H3) distance is now 0.03 Å shorter than the crystallographic value. The initial evidence suggests that purely dispersive effects in this molecule are comparatively small, but a survey of many additional compounds would be required to generalize the conclusion.*
93. Check, C. E.; Faust, T. O.; Bailey, J. M.; Wright, B. J.; Gilbert, T. M.; Sunderlin, L. S., Addition of Polarization and Diffuse Functions to the LANL2DZ Basis Set for P-Block Elements. *J. Phys. Chem. A* **2001**, *105* (34), 8111-8116.
94. Comment178, Construction of LANL08(d) Basis set. *By construction, the LANL08(d) basis sets for the Group 15 elements also includes a additional diffuse p function.*
95. Roy, L. E.; Hay, P. J.; Martin, R. L., Revised Basis Sets for the LANL Effective Core Potentials. *Journal of Chemical Theory and Computation* **2008**, *4* (7), 1029-1031.
96. Zhao, Y.; Truhlar, D. G., A new local density functional for main-group thermochemistry, transition metal bonding, thermochemical kinetics, and noncovalent interactions. *The Journal of Chemical Physics* **2006**, *125* (19), 194101-194118.
97. Bader, R. F. W., *Atoms in Molecules: A Quantum Theory*. Oxford University Press: New York, 1994.
98. Tognetti, V.; Joubert, L.; Raucoles, R.; De Bruin, T.; Adamo, C., Characterizing Agosticity Using the Quantum Theory of Atoms in Molecules: Bond Critical Points and Their Local Properties. *J. Phys. Chem. A* **2012**, *116* (22), 5472-5479.
99. Perrin, L.; Maron, L.; Eisenstein, O., Some structural and electronic properties of MX_3 (M = Ln, Sc, Y, Ti⁺, Zr⁺, Hf⁺; X = H, Me, Hal, NH₂) from DFT calculations. *Faraday Discuss.* **2003**, *124* (0), 25-39.

100. Tang, J. A.; Masuda, J. D.; Boyle, T. J.; Schurko, R. W., Ultra-wideline ^{27}Al NMR Investigation of Three- and Five-Coordinate Aluminum Environments. *ChemPhysChem* **2006**, *7* (1), 117-130.
101. Atwood, D. A.; Atwood, V. O.; Cowley, A. H.; Jones, R. A.; Atwood, J. L.; Bott, S. G., synthesis and Structural Characterization of Homoleptic Gallium Amides. *Inorg. Chem.* **1994**, *33* (15), 3251-3254.
102. Petrie, M. A.; Ruhlandt-Senge, K.; Hope, H.; Power, P. P., Structural studies of the monomeric, low coordinate, indium amides $(t\text{-Bu})_2\text{InN}(2,6\text{-i-Pr}_2\text{C}_6\text{H}_3)\text{SiPh}_3$ and $\text{In}\{\text{N}(\text{SiMe}_3)_2\}_3$. *Bull. Soc. Chim. Fr.* **1993**, *130* (Copyright (C) 2013 American Chemical Society (ACS). All Rights Reserved.), 851-5.
103. Allmann, R.; Henke, W.; Krommes, P.; Lorberth, J., Die molekül- und kristallstruktur von thallium-tris(bis(trimethylsilyl)amin), $\text{Tl}[\text{N}(\text{SiMe}_3)_2]_3$. *J. Organomet. Chem.* **1978**, *162* (3), 283-287.
104. Putzer, M. A.; Magull, J.; Goesmann, H.; Neumueller, B.; Dehnicke, K., Syntheses, properties, and crystal structures of the titanium(III) amido complexes $\text{Ti}[\text{N}(\text{SiMe}_3)_2]_3$, $[\text{TiCl}_2\{\text{N}(\text{SiMe}_3)_2\}(\text{THF})_2]$, and $[\text{Na}(12\text{-crown-4})_2][\text{TiCl}_2\{\text{N}(\text{SiMe}_3)_2\}_2]$. *Chem. Ber.* **1996**, *129* (Copyright (C) 2013 American Chemical Society (ACS). All Rights Reserved.), 1401-1405.
105. Ellison, J. J.; Power, P. P.; Shoner, S. C., First examples of three-coordinate manganese(III) and cobalt(III): synthesis and characterization of the complexes $\text{M}[\text{N}(\text{SiMe}_3)_2]_3$ (M = Mn or Co). *J. Am. Chem. Soc.* **1989**, *111* (20), 8044-6.
106. Hursthouse, M. B.; Rodesiler, P. F., Crystal and molecular structure of tris(hexamethyldisilylamido)iron(III). *J. Chem. Soc., Dalton Trans.* **1972**, (19), 2100-2102.
107. Perrin, D. D.; Armarego, W. L. F., *Purification of Laboratory Chemicals*. 3rd ed.; Pergamon: Oxford, 1988.
108. McCormick, M. J.; Sockwell, S. C.; Davies, C. E. H.; Hanusa, T. P.; Huffman, J. C., Synthesis of a Monopentamethylcyclopentadienyl Halide Complex of Calcium; the X-Ray Crystal Structure of $[(\text{Me}_5\text{C}_5)\text{Ca}(\mu\text{-I})(\text{THF})_2]_2$. *Organometallics* **1989**, *8*, 2044-2049.
109. Meredith, M. B.; McMillen, C. H.; Goodman, J. T.; Hanusa, T. P., Ambient temperature imidazolium-based ionic liquids with tetrachloronickelate(II) anions. *Polyhedron* **2009**, *28* (12), 2355-2358.
110. Alyea, E. C.; Bradley, D. C.; Copperthwaite, R. G., Three-co-ordinated transition metal compounds. Part I. The preparation and characterization of tris(bis(trimethylsilyl)amido)-derivatives of scandium, titanium, vanadium, chromium, and iron. *Journal of the Chemical Society, Dalton Transactions* **1972**, (14), 1580-1584.
111. Gaussian, Gaussian 09W ref. **2009**, Gaussian 09, Revision D.01, Frisch, M. J.; Trucks, G. W.; Schlegel, H. B.; Scuseria, G. E.; Robb, M. A.; Cheeseman, J. R.; Scalmani, G.; Barone, V.; Mennucci, B.; Petersson, G. A.; Nakatsuji, H.; Caricato, M.; Li, X.; Hratchian, H. P.; Izmaylov, A. F.; Bloino, J.; Zheng, G.; Sonnenberg, J. L.; Hada, M.; Ehara, M.; Toyota, K.; Fukuda, R.; Hasegawa, J.; Ishida, M.; Nakajima, T.; Honda, Y.; Kitao, O.; Nakai, H.; Vreven, T.; Montgomery, J. A., Jr.; Peralta, J. E.; Ogliaro, F.; Bearpark, M.; Heyd, J. J.; Brothers, E.; Kudin, K. N.; Staroverov, V. N.; Kobayashi, R.; Normand, J.; Raghavachari, K.; Rendell, A.; Burant, J. C.; Iyengar, S. S.; Tomasi, J.; Cossi, M.; Rega, N.; Millam, N. J.; Klene, M.; Knox, J. E.; Cross, J. B.; Bakken, V.; Adamo, C.; Jaramillo, J.; Gomperts, R.; Stratmann, R. E.; Yazyev, O.; Austin, A. J.; Cammi, R.; Pomelli, C.; Ochterski, J. W.; Martin, R. L.; Morokuma, K.; Zakrzewski, V. G.; Voth, G. A.; Salvador, P.; Dannenberg, J. J.;

Dapprich, S.; Daniels, A. D.; Farkas, Ö.; Foresman, J. B.; Ortiz, J. V.; Cioslowski, J.; Fox, D. J. Gaussian, Inc., Wallingford CT, 2009.

112. Rappe, A. K.; Bormann-Rochotte, L. M.; Wiser, D. C.; Hart, J. R.; Pietsch, M. A.; Casewit, C. J.; Skiff, W. M., APT a next generation QM-based reactive force field model. *Mol. Phys.* **2007**, *105* (2-3), 301-324.

113. Rappé, A. K.; Goddard, W. A., Charge equilibration for molecular dynamics simulations. *J. Phys. Chem.* **1991**, *95* (8), 3358-3363.

114. ADF2013.01; SCM; Theoretical Chemistry; Vrije Universiteit; Amsterdam; The Netherlands; (<http://www.scm.com>).

115. Schuchardt, K. L.; Didier, B. T.; Elsethagen, T.; Sun, L.; Gurumoorthi, V.; Chase, J.; Li, J.; Windus, T. L., Basis Set Exchange: A Community Database for Computational Sciences. *Journal of Chemical Information and Modeling* **2007**, *47* (3), 1045-1052.

116. Weigend, F.; Ahlrichs, R., Balanced basis sets of split valence, triple zeta valence and quadruple zeta valence quality for H to Rn: Design and assessment of accuracy. *Phys. Chem. Chem. Phys.* **2005**, *7* (18), 3297-3305.

117. Grimme, S.; Antony, J.; Ehrlich, S.; Krieg, H., A consistent and accurate ab initio parametrization of density functional dispersion correction (DFT-D) for the 94 elements H-Pu. *J. Chem. Phys.* **2010**, *132* (Copyright (C) 2011 American Chemical Society (ACS). All Rights Reserved.), 154104/1-154104/19.

118. Grimme, S.; Ehrlich, S.; Goerigk, L., Effect of the damping function in dispersion corrected density functional theory. *J. Comput. Chem.* **2011**, *32* (7), 1456-1465.

119. Boyde, N. C.; Chmely, S. C.; Hanusa, T. P.; Rheingold, A. L.; Brennessel, W. W., Structural Distortions in M[E(SiMe₃)₂]₃ Complexes (M = Group 15, f-Element; E = N, CH): Is Three a Crowd? *Inorganic Chemistry* **2014**, *53* (18), 9703-9714.

120. Dahl, J. A.; Maddux, B. L. S.; Hutchison, J. E., Toward Greener Nanosynthesis. *Chemical Reviews* **2007**, *107* (6), 2228-2269.

121. Granqvist, C. G.; Buhrman, R. A., Size distributions for supported metal catalysts. *Journal of Catalysis* **1976**, *42* (3), 477-479.

122. Tao, A. R.; Habas, S.; Yang, P., Shape Control of Colloidal Metal Nanocrystals. *Small* **2008**, *4* (3), 310-325.

123. Tsuzuki, T.; McCormick, P., Mechanochemical synthesis of nanoparticles. *Journal of Materials Science* **2004**, *39* (16-17), 5143-5146.

124. Rak, M. J.; Saade, N. K.; Frišćić, T.; Moores, A., Mechanochemical synthesis of ultra-small monodisperse amine-stabilized gold nanoparticles with controllable size. *Green Chemistry* **2014**, *16* (1), 86-89.

125. Talapin, D. V.; Rogach, A. L.; Kornowski, A.; Haase, M.; Weller, H., Highly Luminescent Monodisperse CdSe and CdSe/ZnS Nanocrystals Synthesized in a Hexadecylamine-Trioctylphosphine Oxide-Trioctylphosphine Mixture. *Nano Letters* **2001**, *1* (4), 207-211.

126. Conte, M.; Wilson, K.; Chechik, V., Radical intermediates in chloroform reactions over triphenylphosphine-protected Au nanoparticles. *Organic & Biomolecular Chemistry* **2009**, *7* (7), 1361-1367.

127. Yang, H. T.; Shen, C. M.; Wang, Y. G.; Su, Y. K.; Yang, T. Z.; Gao, H. J., Stable cobalt nanoparticles passivated with oleic acid and triphenylphosphine. *Nanotechnology* **2004**, *15* (1), 70.

128. Diesveld, J. W.; Menger, E. M.; Edzes, H. T.; Veeman, W. S., High-resolution solid-state phosphorus-31 nuclear magnetic resonance of some triphenylphosphine transition-metal complexes. *Journal of the American Chemical Society* **1980**, *102* (27), 7935-7936.
129. Frazer, M. J.; Gerrard, W.; Twaits, R., Triphenylphosphine oxide complexes of non-transition metal halides. *Journal of Inorganic and Nuclear Chemistry* **1963**, *25* (6), 637-640.
130. Elschenbroich, C., *Organometallics*. 3rd, completely rev. and extended ed. / Christoph Elschenbroich

translated by José Oliveira and Christoph Elschenbroich. ed.; Weinheim : Wiley-VCH: Weinheim, 2006.

131. Etter, M. C.; Baures, P. W., Triphenylphosphine oxide as a crystallization aid. *Journal of the American Chemical Society* **1988**, *110* (2), 639-640.
132. Löble, M. W.; Casimiro, M.; Thielemann, D. T.; Oña-Burgos, P.; Fernández, I.; Roesky, P. W.; Breher, F., ¹H,⁸⁹Y HMQC and Further NMR Spectroscopic and X-ray Diffraction Investigations on Yttrium-Containing Complexes Exhibiting Various Nuclearities. *Chemistry – A European Journal* **2012**, *18* (17), 5325-5334.
133. Kühl, O.; Kühl, O., *Phosphorus-31 NMR spectroscopy : a concise introduction for the synthetic organic and organometallic chemist / by Olaf Kühl*. Berlin

London : Springer: Berlin

London, 2008.

134. Elschenbroich, C., *Organometallics*. 3rd. ed.; VCH Publishers: Weinheim, 2006; p 804.
135. Johns, A. M.; Chmely, S. C.; Hanusa, T. P., Solution Interaction of Potassium and Calcium Bis(trimethylsilyl)amides; Preparation of Ca[N(SiMe₃)₂]₂ from Dibenzylcalcium. *Inorg. Chem.* **2009**, *48* (4), 1380-1384.
136. Harder, S.; Ruspic, C., Probing the Salt-Metathesis Route to Bis-(aryl)calcium Compounds: Structure of an Arylcalcate Complex. *European Journal of Inorganic Chemistry* **2015**, *2015* (35), 5743-5750.
137. Rightmire, N. R.; Hanusa, T. P., Advances in Organometallic Synthesis with Mechanochemical Methods. *Dalton Trans.* **2016**, 2352-2362.
138. Rightmire, N. R.; Bruns, D. L.; Hanusa, T. P.; Brennessel, W. W., Mechanochemical Influence on the Stereoselectivity of Halide Metathesis: Synthesis of Group 15 Tris(allyl) Complexes. *Organometallics* **2016**, *35*, 1698–1706.
139. Tsai, J.-C.; Kuo, J. C.; Chen, Y.-C., Novel catalyst compositions for the syndiospecific polymerization of styrene prepared by the combination of cyclopentadienyl complexes of group IIA or group IIIA elements with titanium alkoxides. *J. Polym. Sci. Part A: Polym. Chem.* **2005**, *43* (11), 2304-2315.
140. Hsiao, T.-J.; Tsai, J.-C., Novel monocyclopentadienyl zirconium and hafnium trialkoxide complexes: Syntheses and catalytic properties for olefin polymerization. *J. Appl. Poly. Sci.* **2010**, *116* (4), 2040-2049.
141. Grafov, A. V.; Firme, C. L.; Grafova, I. A.; Benetollo, F.; Dias, M. L.; Abadie, M. J. M., Olefin polymerisation with hafnocenes: A bridged alicyclic alcohol as a ligand and as the hafnocene modifier. *Polymer* **2005**, *46* (23), 9626-9631.

142. Turner, Z. R.; Buffet, J.-C.; O'Hare, D., Chiral Group 4 Cyclopentadienyl Complexes and Their Use in Polymerization of Lactide Monomers. *Organometallics* **2014**, *33* (14), 3891-3903.
143. Buffet, J.-C.; Harris, G. R.; Coward, J. J.; Arnold, T. A. Q.; Turner, Z. R.; O'Hare, D., Zirconocene alkoxides and aryloxides for the polymerization of L- and rac-lactide. *J. Organomet. Chem.* **2016**, *801*, 87-95.
144. Ning, Y.; Zhang, Y.; Rodriguez-Delgado, A.; Chen, E. Y. X., Neutral Metallocene Ester Enolate and Non-Metallocene Alkoxy Complexes of Zirconium for Catalytic Ring-Opening Polymerization of Cyclic Esters. *Organometallics* **2008**, *27* (21), 5632-5640.
145. Niinistö, J.; Putkonen, M.; Niinistö, L.; Song, F.; Williams, P.; Heys, P. N.; Odedra, R., Atomic Layer Deposition of HfO₂ Thin Films Exploiting Novel Cyclopentadienyl Precursors at High Temperatures. *Chem. Mater.* **2007**, *19* (13), 3319-3324.
146. Ott, K. C.; De Boer, E. J. M.; Grubbs, R. H., An investigation of the reaction of bis(cyclopentadienyl)titanium dichlorides with trimethylaluminum. Mechanism of an α -hydrogen abstraction reaction. *Organometallics* **1984**, *3* (2), 223-30.
147. Gell, K. I.; Schwartz, J., Novel phosphorus ylide complexes of zirconium(IV). *Inorganic Chemistry* **1980**, *19* (11), 3207-3211.
148. Wang, Q.; Quyoum, R.; Gillis, D. J.; Tudoret, M.-J.; Jeremic, D.; Hunter, B. K.; Baird, M. C., Ethylene, Styrene, and α -Methylstyrene Polymerization by Mono(pentamethylcyclopentadienyl) (Cp*) Complexes of Titanium, Zirconium, and Hafnium: Roles of Cationic Complexes of the Type [Cp*MR₂]⁺ (R = Alkyl) as both Coordination Polymerization Catalysts and Carbocationic Polymerization Initiators. *Organometallics* **1996**, *15* (2), 693-703.
149. Nesmeyanov, A. N.; Fedin, E. I.; Petrovskii, P. V.; Dubovitskii, V. A.; Nogina, O. V.; Lazareva, N. A., The nature of the bond between Ti and cyclopentadienyl in mono- and dicyclopentadienyl derivatives of Ti, investigated by means of nuclear magnetic resonance. *Dokl. Akad. Nauk SSSR* **1965**, *163* (3), 659-62.
150. Baum, E.; Matern, E.; Pikies, J.; Robaszkiewicz, A., Oxidative Dimerisierung von Phosphanen und Hinweise auf das intermediäre Auftreten des Phosphinophosphinidens tBu₂P—P in Reaktionen von [(η 5-C₅H₅)₂TiCl₂] und [(η 5-C₅H₅)(η 5-C₅Me₅)TiCl₂] mit tBu₂P—P(SiMe₃)Li und tBu₂P—P(Li)—PtBu₂. Bildung von Titan(III)-Fulvalen-Komplexen. *Z. Anorg. Allg. Chem.* **2004**, *630* (7), 1090-1095.
151. Comment201, Reaction of TDC with KOtBu in a ball mill are fast. *A test milling of a 2:1 K[OtBu]:TDC mixture for only 5 min/600 rpm indicated that TDC was already consumed at that point.*
152. Comment12, We are grateful to a reviewer for this suggestion. *We are grateful to a reviewer for this suggestion.*
153. Hansen, L. M.; Marynick, D. S., A molecular orbital study of conformational preferences of the cyclopentadienyl ligand in titanium(IV) and titanium(III) complexes. *Organometallics* **1989**, *8* (9), 2173-2179.
154. Jacobsen, H.; Berke, H.; Brackemeyer, T.; Eisenblätter, T.; Erker, G.; Fröhlich, R.; Meyer, O.; Bergander, K., Comparison of Characteristic Structural Features among the Triade of Tris(cyclopentadienyl)(Group-4 Metal) Complex Cations: a Combined Theoretical and Experimental Study. *Helvetica Chimica Acta* **1998**, *81* (9), 1692-1709.
155. Clearfield, A.; Warner, D. K.; Saldarriaga-Molina, C. H.; Ropal, R.; Bernal, I., Structural Studies of (π -C₅H₅)₂MX₂ Complexes and their Derivatives. The Structure of

- Bis(π -cyclopentadienyl)titanium Dichloride. *Canadian Journal of Chemistry* **1975**, *53* (11), 1622-1629.
156. Guérin, F.; Beddie, C. L.; Stephan, D. W.; Spence, R. E. v. H.; Wurz, R., η 1- and η 5-Indenyl and Cyclopentadienyl Tri-tert-Butylphosphoraneiminatotitanium Complexes. *Organometallics* **2001**, *20* (16), 3466-3471.
157. Song, Z.; Hsieh, Y.-F.; Kanno, K.-i.; Nakajima, K.; Takahashi, T., Coupling Reaction of a Cyclopentadienyl Ligand with a Dienyl or Alkenyl Moiety on Titanocene. *Organometallics* **2011**, *30* (4), 844-851.
158. Russo, M. R.; Kaltsoyannis, N.; Sella, A., Are metal alkoxides linear owing to electrostatic repulsion? *Chem. Commun.* **2002**, *0* (20), 2458-2459.
159. Howard, W. A.; Trnka, T. M.; Parkin, G., Syntheses of the Phenylchalcogenolate Complexes (η 5-C5Me5)2Zr(EPh)2 (E = O, S, Se, Te) and (η 5-C5H5)2Zr(OPh)2: Structural Comparisons within a Series of Complexes Containing Zirconium-Chalcogen Single Bonds. *Inorg. Chem.* **1995**, *34* (Copyright (C) 2013 American Chemical Society (ACS). All Rights Reserved.), 5900-9.
160. Perrotin, P.; El-Zoghbi, I.; Oguadinma, P. O.; Schaper, F., Replacing Chloride by Alkoxide: Cp2Zr(H)OR, Searching for Alternatives to Schwartz's Reagent. *Organometallics* **2009**, *28* (17), 4912-4922.
161. Benetollo, F.; Cavinato, G.; Crosara, L.; Milani, F.; Rossetto, G.; Scelza, C.; Zanella, P., New O- and N-bonded zirconocene complexes and their catalytic properties in ethylene polymerization. X-ray crystal structure of (C5H5)2Zr{2,6-OC6H3(CH3)2}2, (C5H5)2Zr{2,4,6-OC6H2(CH3)3}2 and (C5H5)2Zr(CH3){CH(NC6H5)2}. *J. Organomet. Chem.* **1998**, *555* (2), 177-185.
162. Zhao, Y.; Truhlar, D. G., The M06 suite of density functionals for main group thermochemistry, thermochemical kinetics, noncovalent interactions, excited states, and transition elements: two new functionals and systematic testing of four M06-class functionals and 12 other functionals. *Theoretical Chemistry Accounts* **2008**, *120* (1), 215-241.
163. Tomasi, J.; Mennucci, B.; Cammi, R., Quantum Mechanical Continuum Solvation Models. *Chemical Reviews (Washington, DC, United States)* **2005**, *105* (8), 2999-3094.
164. Skinner, H. A.; Connor, J. A., Metal-ligand bond-energies in organometallic compounds. *Pure Appl. Chem.* **1985**, *57* (1), 79-88.
165. Dolomanov, O. V.; Bourhis, L. J.; Gildea, R. J.; Howard, J. A. K.; Puschmann, H., OLEX2: a complete structure solution, refinement and analysis program. *J. Appl. Cryst.* **2009**, *42* (2), 339-341.
166. Sheldrick, G., SHELXT - Integrated space-group and crystal-structure determination. *Acta Crystallographica Section A* **2015**, *71* (1), 3-8.
167. Sheldrick, G., Crystal structure refinement with SHELXL. *Acta Crystallographica Section C* **2015**, *71* (1), 3-8.
168. Comment194, APEX2 ref. *APEX2, version 2013.10-0; Bruker AXS: Madison, WI, 2013. APEX2 ref.*
169. Altomare, A.; Burla, M. C.; Camalli, M.; Casciarano, G. L.; Giacovazzo, C.; Guagliardi, A.; Moliterni, A. G. G.; Polidori, G.; Spagna, R., SIR97: a new tool for crystal structure determination and refinement. *J. Appl. Cryst.* **1999**, *32* (1), 115-119.
170. Sheldrick, G., A short history of SHELX. *Acta Crystallographica Section A* **2008**, *64* (1), 112-122.

171. Comment210, Sheldrick, G. M. SHELXL-2013/2 University of Göttingen: Göttingen, Germany, 2013. *Sheldrick, G. M. SHELXL-2013/2 University of Göttingen: Göttingen, Germany, 2013.* **2013**.
172. Rabaâ, H.; Saillard, J.-Y.; Hoffmann, R., Hydrogen-hydrogen and carbon-hydrogen activation reactions at d0 metal centers. *J. Am. Chem. Soc.* **1986**, *108* (15), 4327-4333.
173. Kool, L. B.; Rausch, M. D.; Alt, H. G.; Herberhold, M.; Thewalt, U.; Wolf, B., [Cp₂Ti(PMe₃)₂]⁺—A Versatile Source of Titanocene Derivatives. *Angewandte Chemie International Edition in English* **1985**, *24* (5), 394-401.
174. Atwood, J. L.; Stone, K. E.; Alt, H. G.; Hrcncir, D. C.; Rausch, M. D., The crystal structure of dicarbonyldicyclopentadienyltitanium(II), (η⁵-C₅H₅)₂Ti(CO)₂. *Journal of Organometallic Chemistry* **1977**, *132* (3), 367-375.
175. Niehues, M.; Erker, G.; Kehr, G.; Schwab, P.; Fröhlich, R.; Blacque, O.; Berke, H., Synthesis and Structural Features of Arduengo Carbene Complexes of Group 4 Metallocene Cations. *Organometallics* **2002**, *21* (14), 2905-2911.
176. Hlina, J.; Baumgartner, J.; Marschner, C.; Zark, P.; Müller, T., Coordination Chemistry of Disilylated Germylenes with Group 4 Metallocenes. *Organometallics* **2013**, *32* (11), 3300-3308.
177. Arp, H.; Baumgartner, J.; Marschner, C.; Zark, P.; Müller, T., Coordination Chemistry of Cyclic Disilylated Stannylenes and Plumblylenes to Group 4 Metallocenes. *J. Am. Chem. Soc.* **2012**, *134* (26), 10864-10875.
178. Zirngast, M.; Flock, M.; Baumgartner, J.; Marschner, C., Group 4 Metallocene Complexes of Disilenes, Digermenes, and a Silagermene. *J. Am. Chem. Soc.* **2009**, *131* (43), 15952-15962.
179. Boyde, N. C.; Rightmire, N. R.; Bierschenk, E. J.; Steelman, G. W.; Hanusa, T. P.; Brennessel, W. W., Reaction environment and ligand lability in group 4 Cp₂MX₂ (X, Y = Cl, OtBu) complexes. *Dalton Transactions* **2016**, *45* (46), 18635-18642.
180. Takahashi, T., *Metallocenes in Regio- and Stereoselective Synthesis*. Springer-Verlag: Berlin, 2005; Vol. 8.
181. Collins, R. A.; Russell, A. F.; Mountford, P., Group 4 metal complexes for homogeneous olefin polymerisation: a short tutorial review. *Applied Petrochemical Research* **2015**, *5* (3), 153-171.
182. Slifirski, J.; Teyssandier, F., Thermodynamic approach to the OMCVD of titanium carbide from titanocene dichloride. *Chemical Vapor Deposition* **1996**, *2* (6), 247-251.
183. Jobbágy, C.; Tunyogi, T. n.; Pálinkás, G. b.; Deák, A., A Versatile Solvent-Free Mechanochemical Route to the Synthesis of Heterometallic Dicyanoaurate-Based Coordination Polymers. *Inorg. Chem.* **2011**, *50* (15), 7301-7308.
184. Jobbágy, C.; Molnar, M.; Baranyai, P.; Deák, A., Mechanochemical synthesis of crystalline and amorphous digold(i) helicates exhibiting anion- and phase-switchable luminescence properties. *Dalton Transactions* **2014**, *43* (31), 11807-11810.
185. Bowmaker, G. A.; Hanna, J. V.; Hart, R. D.; Healy, P. C.; King, S. P.; Marchetti, F.; Pettinari, C.; Skelton, B. W.; Tabacaru, A.; White, A. H., Mechanochemical and solution synthesis, X-ray structure and IR and ³¹P solid state NMR spectroscopic studies of copper(i) thiocyanate adducts with bulky monodentate tertiary phosphine ligands. *Dalton Trans.* **2012**, *41* (25), 7513-7525.
186. Garay, A. L.; Pichon, A.; James, S. L., Solvent-free synthesis of metal complexes. *Chem. Soc. Rev.* **2007**, *36* (6), 846-855.

187. Rightmire, N. R.; Hanusa, T. P., Advances in Organometallic Synthesis with Mechanochemical Methods. *Dalton Trans.* **2016**, *45*, 2352-2362.
188. Orita, A.; Jiang, L.; Nakano, T.; Ma, N.; Otera, J., Solventless reaction dramatically accelerates supramolecular self-assembly. *Chem. Commun.* **2002**, (13), 1362-1363.
189. Rightmire, N. R.; Hanusa, T. P.; Rheingold, A. L., Mechanochemical Synthesis of [1,3-(SiMe₃)₂C₃H₃]₃(Al,Sc), a Base-Free Tris(allyl)aluminum Complex and Its Scandium Analogue. *Organometallics* **2014**, *33*, 5952–5955.
190. Shi, Y. X.; Xu, K.; Clegg, J. K.; Ganguly, R.; Hirao, H.; Friščić, T.; García, F., The First Synthesis of the Sterically Encumbered Adamantoid Phosphazane P₄(NtBu)₆: Enabled by Mechanochemistry. *Angew. Chem. Int. Ed.* **2016**, *55* (41), 12736-12740.
191. Hernández, J. G.; Macdonald, N. A. J.; Mottillo, C.; Butler, I. S.; Friščić, T., A mechanochemical strategy for oxidative addition: remarkable yields and stereoselectivity in the halogenation of organometallic Re(i) complexes. *Green Chem.* **2014**, *16* (3), 1087-1092.
192. Nesmeyanov, A. N.; Nogina, O. V.; Lazareva, N. A.; Dubovitskii, V. A., Inverse disproportionation reaction and ester interchange of monocyclopentadienyltitaniums. *Izvestiya Akademii Nauk SSSR, Seriya Khimicheskaya* **1967**, (4), 808-14.
193. Gibson, D. H.; Ding, Y.; Mashuta, M. S.; Richardson, J. F., Chlorobis([eta]⁵-cyclopentadienyl)methoxytitanium. *Acta Crystallographica Section C* **1996**, *52* (3), 559-560.
194. Rolsten, R. F.; Sisler, H. H., Molecular Addition Compounds of Titanium Tetrabromide and Titanium Tetraiodide with Several Ethers. *J. Am. Chem. Soc.* **1957**, *79* (5), 1068-1070.
195. Comment212, Properties of TiBr₄(thf)₂. *The adduct TiBr₄(thf)₂ has been used in the preparation of some titanium complexes, but its preparation requires a low-temperature (-78 °C) reaction between TiBr₄ and THF followed by several days of vacuum drying to obtain a solid product. The resulting material is not soluble in THF, CHCl₃, or CCl₄. See. ref. X.*
196. Hernández, J. G.; Friščić, T., Metal-catalyzed organic reactions using mechanochemistry. *Tetrahedron Lett.* **2015**, *56* (29), 4253-4265.
197. Boldyreva, E., Mechanochemistry of inorganic and organic systems: what is similar, what is different? *Chem. Soc. Rev.* **2013**, *42* (18), 7719-7738.
198. Wang, G.-W., Mechanochemical organic synthesis. *Chem. Soc. Rev.* **2013**, *42* (18), 7668-7700.
199. Waddell, D. C.; Thiel, I.; Clark, T. D.; Marcum, S. T.; Mack, J., Making kinetic and thermodynamic enolates via solvent-free high speed ball milling. *Green Chemistry* **2010**, *12* (2), 209-211.
200. Huffman, J. C.; Moloy, K. G.; Marsella, J. A.; Caulton, K. G., Molecular Structure of (h⁵-C₅H₅)₂Ti(OC₂H₅)Cl and [(h⁵-C₅H₅)Cl₂Ti]₂O₂C₂(CH₃)₄. A Structural Basis for Deoxygenation Using Titanium. *J. Am. Chem. Soc.* **1980**, *102*, 3009-3014.
201. Comment211, Bond lengths in Cp₂TiCl(OR) complexes. *The next widest angle is 152.9(5)°, found in the XCV complex. The Ti–O bond length is 1.824(5) Å, shorter than the distance in Cp₂TiCl(OEt), but 0.38 Å longer than the distance in 3. (Carvalho, M. F. N. N.; Galvão, A. M.; Kredatusová, J.; Merna, J.; Pinheiro, P. F.; Margarida Salema, M., Inorg. Chim. Acta* **2012**, *383*, 244-249). *123* (13), 3092-107.
202. Jones, P. G.; Kienitz, C.; Thöne, C., Crystal structure of dibromobis(cyclopentadienyl)titanium(IV), C₁₀H₁₀Br₂Ti. *Zeitschrift für Kristallographie - Crystalline Materials* **1994**, *209* (1), 85.

203. Howard, W. A.; Trnka, T. M.; Parkin, G., Syntheses of the Phenylchalcogenolate Complexes ($\eta^5\text{-C}_5\text{Me}_5$) $2\text{Zr}(\text{EPh})_2$ (E = O, S, Se, Te) and ($\eta^5\text{-C}_5\text{H}_5$) $2\text{Zr}(\text{OPh})_2$: Structural Comparisons within a Series of Complexes Containing Zirconium-Chalcogen Single Bonds. *Inorg. Chem.* **1995**, *34* (Copyright (C) 2013 American Chemical Society (ACS). All Rights Reserved.), 5900-5909.
204. Fazaeli, Y.; Amini, M. M.; Ng, S. W., Bis(isopropoxido-[kappa]O)bis(2-methylquinolin-8-olato-[kappa]2N,O)titanium(IV). *Acta Crystallographica Section E* **2008**, *64* (12), m1509.
205. Austin, A.; Petersson, G. A.; Frisch, M. J.; Dobek, F. J.; Scalmani, G.; Throssell, K., A Density Functional with Spherical Atom Dispersion Terms. *J. Chem. Theory Comp.* **2012**, *8* (12), 4989-5007.
206. Grimme, S., Semiempirical hybrid density functional with perturbative second-order correlation. *The Journal of Chemical Physics* **2006**, *124* (3), 034108.
207. Nugent, W. A.; Mayer, J. M., *Metal-ligand multiple bonds : the chemistry of transition metal complexes containing oxo, nitrido, imido, alkylidene, or alkylidyne ligands*. Wiley: New York, 1988.
208. Manz, T. A.; Fenwick, A. E.; Phomphrai, K.; Rothwell, I. P.; Thomson, K. T., The nature of aryloxy and arylsulfide ligand bonding in dimethyltitanium complexes containing cyclopentadienyl ligation. *Dalton Trans.* **2005**, (4), 668-674.
209. Mingos, D. M. P., A review of complexes of ambivalent and ambiphilic Lewis acid/bases with symmetry signatures and an alternative notation for these non-innocent ligands. *J. Organomet. Chem.* **2014**, *751*, 153-173.
210. Mingos, D. M. P., A theoretical analysis of ambivalent and ambiphilic Lewis acid/bases with symmetry signatures. *Coord. Chem. Rev.* **2015**, *293-294*, 2-18.
211. Arrowsmith, M.; Hill, M. S.; Kociok-Köhn, G., Activation of N-Heterocyclic Carbenes by {BeH₂} and {Be(H)(Me)} Fragments. *Organometallics* **2015**, *34* (3), 653-662.
212. Shannon, R. D., Revised effective ionic radii and systematic studies of interatomic distances in halides and chalcogenides. *Acta Crystallogr., Sect A* **1976**, *32*, 751-767.
213. Westerhausen, M., Synthesis and Spectroscopic Properties of Bis(trimethylsilyl)amides of the Alkaline-earth Metals Magnesium, Calcium, Strontium, and Barium. *Inorg. Chem.* **1991**, *30*, 96-101.
214. Nugent, K. W.; Beattie, J. K.; Hambley, T. W.; Snow, M. R., A precise Low-temperature crystal structure of bis(cyclopentadienyl)beryllium. *Aust. J. Chem.* **1984**, *37*, 1601-1606.
215. Burkey, D. J.; Hanusa, T. P., Structural Lessons from Main-Group Metallocenes. *Comments Inorg. Chem.* **1995**, *17*, 41-77.
216. Civic, T. M., Beryllium Metal Toxicology: A Current Perspective. In *Encyclopedia of Inorganic and Bioinorganic Chemistry*, John Wiley & Sons, Ltd: 2011.
217. Hanusa, T. P.; Bierschenk, E. J.; Engerer, L. K.; Martin, K. A.; Rightmire, N. R., 1.37 - Alkaline Earth Chemistry: Synthesis and Structures. In *Comprehensive Inorganic Chemistry II (Second Edition)*, Reedijk, J.; Poeppelmeier, K., Eds. Elsevier: Amsterdam, 2013; pp 1133-1187.
218. Iversen, K. J.; Couchman, S. A.; Wilson, D. J. D.; Dutton, J. L., Modern organometallic and coordination chemistry of beryllium. *Coord. Chem. Rev.* **2015**, *297-298*, 40-48.

219. Naglav, D.; Buchner, M. R.; Bendt, G.; Kraus, F.; Schulz, S., Off the Beaten Track—A Hitchhiker's Guide to Beryllium Chemistry. *Angew. Chem. Int. Ed.* **2016**, *55* (36), 10562-10576.
220. del Mar Conejo, M.; Fernandez, R.; Gutierrez-Puebla, E.; Monge, A.; Ruiz, C.; Carmona, E., Synthesis and X-ray structures of [Be(C5Me4H)2] and [Be(C5Me5)2]. *Angew. Chem., Int. Ed.* **2000**, *39* (11), 1949-1951.
221. Chmely, S. C.; Hanusa, T. P.; Brennessel, W. W., Bis(1,3-trimethylsilylallyl)beryllium. *Angew. Chem. Int. Ed.* **2010**, *49* (34), 5870–5874.
222. Solomon, S. A.; Muryn, C. A.; Layfield, R. A., s-Block metal complexes of a bulky, donor-functionalized allyl ligand. *Chem. Commun.* **2008**, (27), 3142-3144.
223. Chmely, S. C.; Carlson, C. N.; Hanusa, T. P.; Rheingold, A. L., Classical versus Bridged Allyl Ligands in Magnesium Complexes: The Role of Solvent. *J. Am. Chem. Soc.* **2009**, *131* (18), 6344-6345.
224. Gren, C. K.; Hanusa, T. P.; Rheingold, A. L., Threefold Cation– π Bonding in Trimethylsilylated Allyl Complexes. *Organometallics* **2007**, *26*, 1643–1649.
225. Layfield, R. A.; Garcia, F.; Hannauer, J.; Humphrey, S. M., Ansa-tris(allyl) complexes of alkali metals: Tripodal analogues of cyclopentadienyl and ansa-metallocene ligands. *Chem. Commun.* **2007**, (47), 5081-5083.
226. Neumüller, B.; Weller, F.; Dehnicke, K., Synthese, Schwingungsspektren und Kristallstrukturen der Chloroberyllate (Ph4P)2[BeCl4] und (Ph4P)2[Be2Cl6]. *Zeitschrift fuer Anorganische und Allgemeine Chemie* **2003**, *629* (12-13), 2195-2199.
227. Plieger, P. G.; John, K. D.; Keizer, T. S.; McCleskey, T. M.; Burrell, A. K.; Martin, R. L., Predicting ⁹Be Nuclear Magnetic Resonance Chemical Shielding Tensors Utilizing Density Functional Theory. *J. Am. Chem. Soc.* **2004**, *126* (44), 14651-14658.
228. Comment206, The correlation between ⁹Be chemical shift is not exact, and can be strongly influenced by the electronic properties of the ligands. The 2-coordinate complex beryllium bis(N,N'-bis(2,6-diisopropylphenyl)-1,3,2-diazaborolyl), for example, has an extreme downfield shift of $\delta = 44$ ppm (Arnold, T.; Braunschweig, H.; Ewing, W. C.; Kramer, T.; Mies, J.; Schuster, J. K., *Chem. Commun.* 2015, *51*, 737-740), whereas the 2-coordinate Be(N(SiMe3)2 displays a ⁹Be NMR shift at $\delta = 12.3$ ppm (ref. {Naglav, 2015 #10249}).
Coord number and ⁹Be Chemical shift.
229. Wermer, J. R.; Gaines, D. F.; Harris, H. A., Synthesis and molecular structure of lithium tri-tert-butylberyllate, Li[Be(tert-C4H9)3]. *Organometallics* **1988**, *7* (11), 2421-2422.
230. Gottfriedsen, J.; Blaurock, S., The First Carbene Complex of a Diorganoberyllium: Synthesis and Structural Characterization of Ph2Be(i-Pr-carbene) and Ph2Be(n-Bu2O). *Organometallics* **2006**, *25* (15), 3784-3786.
231. Arrowsmith, M.; Hill, M. S.; Kociok-Köhn, G.; MacDougall, D. J.; Mahon, M. F., Beryllium-Induced C–N Bond Activation and Ring Opening of an N-Heterocyclic Carbene. *Angewandte Chemie International Edition* **2012**, *51* (9), 2098-2100.
232. Weiss, E.; Wolfrum, R., Über metall—alkyl-verbindungen VIII. Die kristallstruktur des lithium-tetramethylberyllats. *Journal of Organometallic Chemistry* **1968**, *12* (2), 257-262.
233. Comment203, Relative stabilities of Beryllate forms. *With a free energy difference of 20.3 kJ mol⁻¹, a straightforward calculation provides an equilibrium constant (K) at 25 °C of 3600:1.*
234. Glock, C.; Görls, H.; Westerhausen, M., N,N,N',N'-Tetramethylethylendiamine adducts of amido calcium bases – Synthesis of monomeric [(tmeda)Ca{N(SiMe3)2}2],

- [(tmeda)Ca{NiPr₂}₂], and dimeric Hauser base-type [(tmeda)Ca(tmp)(μ-I)]₂ (tmp = 2,2,6,6-tetramethylpiperidide). *Inorg. Chim. Acta* **2011**, 374 (1), 429-434.
235. Fitts, L. S.; Bierschenk, E. J.; Hanusa, T. P.; Rheingold, A. L.; Pink, M.; Young, V. G., Selective modification of the metal coordination environment in heavy alkaline-earth iodide complexes. *New J. Chem.* **2016**, 40, 8229 - 8238.
236. Comment209, Reaction of KA' and BeCl₂ in THF. *In a preliminary study, the reaction of K[A'] and BeCl₂ in a 2:1 molar ratio in THF (1 hr) was found not to produce K[BeA'3]. A species with a 9Be NMR shift of δ = 16.6 ppm was present instead, which is tentatively identified as BeA'2(thf). If so, this indicates that THF, like Et₂O, can block the formation of the tris(allyl) anion with Be, although it does not do so for Zn and Sn.*
237. Naglav, D.; Buchner, M. R.; Bendt, G.; Kraus, F.; Schulz, S., Off the Beaten Track—A Hitchhiker's Guide to Beryllium Chemistry. *Angewandte Chemie International Edition* **2016**, 55 (36), 10562-10576.
238. Fraenkel, G.; Chow, A.; Winchester, W. R., Dynamics of solvated lithium(+) within exo,exo-[1,3-bis(trimethylsilyl)allyl]lithium N,N,N',N'-tetramethylethylenediamine complex. *Journal of the American Chemical Society* **1990**, 112 (4), 1382-1386.
239. Harvey, M. J.; Hanusa, T. P.; Young, V. G., Jr., Synthesis and Crystal Structure of a Bis(allyl) Complex of Calcium, [Ca{C₃(SiMe₃)₂H₃}₂·(thf)₂]. *Angew. Chem. Int. Ed.* **1999**, 38, 217-219.
240. Comment193, *Sheldrick, G. M. SADABS, version 2012/1; University of Göttingen: Göttingen, Germany, 2012. SADABS ref.*
241. *SAINTE*, version 8.32B; Bruker AXS: Madison, WI, 2014.
242. Comment192, SIR2011 ref. *Burla, M. C.; Caliandro, R.; Camalli, M.; Carrozzini, B.; Cascarano, G. L.; Giacovazzo, C.; Mallamo, M.; Mazzone, A.; Polidori, G.; Spagna, R. SIR2011: a new package for crystal structure determination and refinement, version 1.0; Istituto di Cristallografia: Bari, Italy, 2012.*